

ABSTRACT

Title of dissertation: **WAVE CHAOTIC EXPERIMENTS
AND MODELS FOR COMPLICATED
WAVE SCATTERING SYSTEMS**

Jen-Hao Yeh, Doctor of Philosophy, 2013

Dissertation directed by: **Professor Steven Anlage
Electrical and Computer Engineering Department**

Wave scattering in a complicated environment is a common challenge in many engineering fields because the complexity makes exact solutions impractical to find, and the sensitivity to detail in the short-wavelength limit makes a numerical solution relevant only to a specific realization. On the other hand, wave chaos offers a statistical approach to understand the properties of complicated wave systems through the use of random matrix theory (RMT). A bridge between the theory and practical applications is the random coupling model (RCM) which connects the universal features predicted by RMT and the specific details of a real wave scattering system. The RCM gives a complete model for many wave properties and is beneficial for many physical and engineering fields that involve complicated wave scattering systems.

One major contribution of this dissertation is that I have utilized three microwave systems to thoroughly test the RCM in complicated wave systems with varied loss, including a cryogenic system with a superconducting microwave cavity

for testing the extremely-low-loss case. I have also experimentally tested an extension of the RCM that includes short-orbit corrections. Another novel result is development of a complete model based on the RCM for the fading phenomenon extensively studied in the wireless communication fields. This fading model encompasses the traditional fading models as its high-loss limit case and further predicts the fading statistics in the low-loss limit. This model provides the first physical explanation for the fitting parameters used in fading models.

I have also applied the RCM to additional experimental wave properties of a complicated wave system, such as the impedance matrix, the scattering matrix, the variance ratio, and the thermopower. These predictions are significant for nuclear scattering, atomic physics, quantum transport in condensed matter systems, electromagnetics, acoustics, geophysics, etc.

WAVE CHAOTIC EXPERIMENTS AND MODELS
FOR COMPLICATED WAVE SCATTERING SYSTEMS

by

Jen-Hao Yeh

Dissertation submitted to the Faculty of the Graduate School of the
University of Maryland, College Park in partial fulfillment
of the requirements for the degree of
Doctor of Philosophy
2013

Advisory Committee:
Professor Steven Anlage, Chair/Advisor
Professor Thomas Antonsen
Professor Christopher Davis
Professor Edward Ott
Professor Romel Gomez

© Copyright by
Jen-Hao Yeh
2013

Dedication

Dedicated to my parents

Yeh, Sung-Chiu

and

Yu, Hsiu-Mei.

Acknowledgments

My Ph.D. study would never have been completed without the help of members in the University of Maryland and researchers in the big science community all over the world. I would like to acknowledge them for their assistance in the theoretical work or the experiments, their comments, feedbacks, and all other support during my Ph.D research.

The most important person in my Ph.D. research is my advisor, Professor Steven Anlage. He provided me all kinds of support in research, including his knowledge of microwave, wave chaos, superconducting, and other physical and engineering fields, the experiment equipment and resources, and his suggestions of the research directions. He is a role model and has shown me how to be a successful faculty member who is excellent and enthusiastic at researching, teaching, and collaborating with all members in the community. I hope one day I will be like him.

I also would like to acknowledge my co-advisors, Professor Thomas Antonsen and Professor Edward Ott. They gave me valuable suggestions and feedbacks regularly in this five years. I admire their incredible intelligence that they could always point out the critical problems in my research and give me useful suggestions to solve them.

In addition to advisors, I would like to acknowledge researchers who have directly worked with me on my research. Thank you, Dr. Biniyam Taddese, Dr. James Hart, Dr. Gabriele Gradoni, Ming-Jer Lee, Michael Johnson, and Bo Xiao in our research group, and Zachary Drikas, Hai Tran, Jesus Gil Gil, and Sun Hong

in Dr. Tim Andreadis' group in Naval Research Laboratory. It is my honor to work with these great researchers. I also would like to acknowledge previous researchers in our group, Dr. Sameer Hemmady, Dr. Xing Zheng, Dr. Florian Schaefer, and Elliott Bradshaw. Their great work gave me tools and bases for my research. My research would also not be possible without the experimental help from Professor H. J. Paik and Dr. M. V. Moody in the University of Maryland, Dr. A. Richter's group in the Technical University of Darmstadt, and L. Ranzani. I also thank the helpful comments from Professor Christopher Davis, who is the committee member of my dissertation and my thesis proposal, Professor Thomas Murphy, Dr. Louis Pecora, and Dr. John Rogers. I would like to thank Professor Romel Gomez for being on my dissertation committee.

I also would like to thank the research companies, Tamin, Mark, Behnood, Matthew, Cihan, Trysten, Harita, Melissa, Daimeng, Enrique, Laura, Nightvid, Henry, Ben, Creeg, and David in our research group, and all of the graduate students in Center for Nanophysics and Advanced Materials. Thank them for their comments and questions in my seminar presentations and their moral support through the years.

Finally, I would like to appreciate my family and friends in Taiwan, and new friends in the US. Without you, I would not be able to start my research career and pursue my scientific dream in Maryland.

Table of Contents

| | |
|--|------|
| List of Figures | viii |
| List of Abbreviations | xiv |
| 1 Introduction | 1 |
| 1.1 Motivation | 1 |
| 1.2 Wave Equations | 3 |
| 1.3 Statistical Approach | 5 |
| 1.4 Wave Chaos | 7 |
| 1.4.1 Classical Chaos and Wave Chaotic Systems | 8 |
| 1.4.2 Microwave Billiard Approach | 12 |
| 1.5 Random Matrix Theory | 13 |
| 1.6 Random Coupling Model | 15 |
| 1.6.1 Random Coupling Model and Poisson Kernel | 16 |
| 1.7 Fading Models | 20 |
| 1.8 Outline of Dissertation | 21 |
| 2 Extended Random Coupling Model | 25 |
| 2.1 Original Random Coupling Model | 25 |
| 2.1.1 Perfectly-Coupled Impedance Matrix | 26 |
| 2.1.2 Radiation Impedance Matrix | 29 |
| 2.2 Short-Orbit Corrections to the Random Coupling Model | 31 |
| 2.2.1 Short Orbits | 32 |
| 2.2.2 Semiclassical Approach to Short-Orbit Terms | 35 |
| 2.3 Chapter Summary | 40 |
| 3 Experimental Systems with a Variety of Loss Values | 42 |
| 3.1 Measurement of Ray-Chaotic Microwave Cavity | 42 |
| 3.1.1 Perturbers and Configuration Ensemble | 46 |
| 3.1.2 Microwave Absorbers and Radiation Impedance | 49 |
| 3.2 Superconducting Cavity and the Cryogenic System | 49 |
| 3.3 Three-Dimensional Cavity | 55 |
| 4 Verification of Short-Orbit Correction | 58 |
| 4.1 Individual Short Orbits | 59 |
| 4.2 Short-Orbit Correction and Frequency Smoothing | 66 |
| 4.3 Short-Orbit Correction and Configuration Ensemble | 72 |
| 4.4 Benefits of the Short-Orbit Correction | 77 |
| 4.4.1 Statistics of the Impedance Matrix | 77 |
| 4.4.2 Statistics of the Scattering Matrix | 81 |
| 4.4.3 Statistics of a Single Realization | 86 |
| 4.5 Chapter Summary | 89 |

| | | |
|---------|---|-----|
| 5 | Application of the Random Coupling Model in Fading | 90 |
| 5.1 | Fading Model based on the Random Coupling Model | 91 |
| 5.2 | Comparison with the Rayleigh Fading Model | 95 |
| 5.3 | Comparison with the Rice Fading Model | 98 |
| 5.4 | Chapter Summary | 101 |
| 6 | Wave Scattering Properties in Varied Loss Systems | 103 |
| 6.1 | Impedance and Scattering Matrices | 104 |
| 6.2 | Variance Ratio | 108 |
| 6.3 | Quantum Dot Properties and the Thermopower | 115 |
| 6.3.1 | Transmittance | 117 |
| 6.3.2 | Thermopower | 118 |
| 7 | Conclusions and Future Work | 124 |
| 7.1 | Conclusions | 124 |
| 7.2 | Future Work | 126 |
| 7.2.1 | Random Coupling Model for Mixed Systems | 126 |
| 7.2.2 | Random Coupling Model for TRIB Systems | 129 |
| 7.2.3 | Random Coupling Model for Nonlinear Systems | 130 |
| 7.2.3.1 | Rouge Waves | 130 |
| 7.2.3.2 | Nonlinear Wave Models | 132 |
| 7.2.3.3 | Proposal of Experimental Systems | 133 |
| 7.2.4 | Source Localization | 134 |
| | Appendices | 139 |
| A | Numerical Algorithms | 139 |
| A.1 | Impedance Matrix Based on Random Matrix Theory | 139 |
| A.1.1 | Frequency Dependence of z_{rmt} | 142 |
| A.1.2 | Gaussian Unitary Ensemble Case | 144 |
| A.2 | Short Orbit Terms | 145 |
| A.2.1 | Short-Orbit-Searching Algorithm | 146 |
| A.2.2 | Computing Parameters | 149 |
| B | Cryogenic Thru-Reflect-Line Calibration | 151 |
| B.1 | Thru-Reflect-Line Calibration | 152 |
| B.2 | <i>In-situ</i> Broadband Cryogenic Calibration System | 156 |
| B.3 | Pseudo-Open Standard | 162 |
| B.4 | Test of RMT Predictions | 171 |
| B.5 | Conclusion | 172 |
| C | Error Analysis of Short-Orbit Correction | 175 |

| | |
|--|-----|
| D Fading Model in the High Loss Regime | 179 |
| D.1 Time-Reversal-Invariant Case | 180 |
| D.2 Time-Reversal-Invariance-Broken Case | 183 |
| D.3 Conclusion | 184 |
| Bibliography | 185 |

List of Figures

| | | |
|-----|---|----|
| 1.1 | Two-dimensional billiards: (a) a rectangular billiard (integrable), (b) a circular billiard (integrable), (c) a bowtie billiard (chaotic) with four inward circular arcs, (d) a cut-circle billiard (chaotic) as a circle with two straight cuts, (e) a mushroom billiard (mixed) as a semicircle with a rectangular stem, and (f) an annular billiard (mixed) as the region between two eccentric circles. | 10 |
| 1.2 | An N -port network system as the model of the N -port wave scattering enclosure. The voltage V_n appears on the n^{th} transmission line of characteristic impedance $Z_{0,nn}$, carrying the current I_n . The incoming (V_n^{in}) and outgoing (V_n^{out}) voltage waves offer a complementary description of the situation at the n^{th} port. | 18 |
| 1.3 | The structure of the chapters in this dissertation. | 22 |
| 2.1 | Illustrations of short orbits in a cut-circle billiard with a circular perturber. The red dots are the ports, black lines are the boundary of the billiard and the perturber, and colored lines are examples of short orbits. Note that the blue lines are direct orbits. The two-bounce orbit (light green) in (a) is blocked in (b) due to the shift of the perturber. | 33 |
| 3.1 | (a) The 1/4-bowtie cavity connected through two transmission lines to a network analyzer. (b) The side view of a port antenna and the cavity. (c) The top view of the 1/4-bowtie cavity with the two ports as red dots and the two metallic perturbers as blue circles. | 43 |
| 3.2 | The two pairs of perturbers. | 47 |
| 3.3 | The two cylindrical perturbers in the 1/4-bowtie cavity without the lid. | 47 |
| 3.4 | The arrangement of microwave absorbers for the measurement of the radiation impedance. The upper plot is the side view, and the lower plot is the top view. Microwave absorbers are represented as the gray material along the walls. The red dots represent the ports of the cavity. | 48 |
| 3.5 | (a) The quasi-two-dimensional symmetry-reduced cut-circle microwave cavity in a three-dimensional perspective, showing the cavity dimensions, ports, and the perturber. (b) Projected two-dimensional view of the cut-circle billiard. | 51 |
| 3.6 | Illustration of the <i>in-situ</i> broadband cryogenic calibration system with the cut-circle cavity. Note that the phase-matched coaxial cables are not shown to scale. | 53 |
| 3.7 | The upper picture shows the cut-circle cavity hanging in the cryostat. The thermal straps are connected to the 4K stage of the refrigerator on the top and to the cavity on the bottom. The lower picture shows the measurement system with the cryorefrigerator, the network analyzer, the voltage controller, and the cryostat labeled. | 54 |

| | | |
|-----|---|----|
| 3.8 | The experimental setup of measurement of the GigaBox as measured by the Naval Research Laboratory group. | 56 |
| 4.1 | Four examples of the comparison between the $z_{cor,n,m}$ elements (Data) and the $\zeta_{n,m}^{(LM)}$ elements (Theory). The insets are the corresponding geometry of the exposed walls. The thick black lines denote microwave absorber material covering the walls. | 62 |
| 4.2 | The loss parameter α and the attenuation parameter κ versus frequency of the empty 1/4-bowtie cavity. The loss parameter is determined by the best-fit of the statistics of the measured impedance data and the RMT prediction, and the attenuation parameter is calculated from the loss parameter. | 65 |
| 4.3 | The impedance of the empty 1/4-bowtie cavity with two ports. Shown are (a) the real part of Z_{11} , (b) the imaginary part of Z_{11} , (c) the real part of Z_{12} , and (d) the imaginary part of Z_{12} with the measured impedance $Z_{n,m}$ (red thinner), the short-orbit-corrected radiation impedance $Z_{soc,n,m}^{(LM)}$ (blue dashed), as well as the radiation impedance $Z_{rad,n,m}$ (black). | 69 |
| 4.4 | The smoothed impedance of the 1/4-bowtie cavity versus frequency of (a) Z_{11} in the one-port experiment, (b) Z_{11} in the two-port experiment, and (c) Z_{12} in the two-port experiment. Shown are the real (three upper curves) and the imaginary parts (three lower curves) of the smoothed impedance for the theory $Z_{soc,n,m}^{(LM)}$ (blue dashed curves) and the experiment $Z_{n,m}$ (red solid curves), as well as the measured (un-smoothed) radiation impedance of the port ($Z_{rad,n,m}$, black thick). | 71 |
| 4.5 | Left: the one-port experiment system with two irregular-shaped perturbors. Right: the two-port experiment system with two cylindrical perturbors. | 73 |
| 4.6 | The averaged impedance versus frequency of (a) Z_{11} in the one-port experiment, (b) Z_{11} in the two-port experiment, and (c) Z_{12} in the two-port experiment. Shown are the real (three upper curves) and the imaginary parts (three lower curves) of the ensemble-averaged impedance $Z_{avg,n,m}$ (red solid curves), comparing with the theory $Z_{soc,n,m}^{(LM)}$ (blue dashed curves) and the radiation impedance of the port ($Z_{rad,n,m}$, black thick). | 75 |
| 4.7 | The probability distributions of (a) the real part and (b) the imaginary part of the normalized impedance eigenvalues in the frequency range 6.8 – 7.0 GHz, and (c) the real part and (d) the imaginary part of the normalized impedance in the frequency range 11.0 – 11.2 GHz. | 79 |
| 4.8 | An example of the probability distributions $P(\varphi_s)$ of the phase φ_s of eigenvalues of the normalized scattering matrices, taken over from the 11.0 – 11.5 GHz frequency window. | 82 |

| | | |
|------|---|-----|
| 4.9 | The average RMS error of the phase distributions $P(\varphi_s)$ of the eigenvalues of the normalized scattering matrices from different normalization methods and varied frequency window sizes. Shown are (a) the one-port case and (b) the two-port case. | 85 |
| 4.10 | The errors for (a) the one-port experiment and (b) the two-port experiment. Shown are δ_μ for the errors in the mean (blue circles) of the normalized impedance eigenvalues and δ_σ for the errors in the standard deviations (green squares). | 88 |
| 5.1 | The probability density functions of the fading amplitude (a) $ s_{rmt,21} $ for the TRI case and (b) $ \tilde{s}_{rmt,21} $ for the TRIB case. Solid curves show the numerical results from the RMT approach with different loss parameters. For the higher loss cases ($\alpha = 1$ and $\alpha = 10$), the corresponding Rayleigh distributions are shown as dashed curves. | 92 |
| 5.2 | Probability density functions from the experimental data [$P(s_{n,21})$, the red curves with circles] in (a) the 1/4-bowtie cavity and in (b) the cut-circle cavity, comparing with the RMT model [$P(s_{rmt,21})$, the black solid curves] and the best-matched Rayleigh distribution (the blue dashed curves). | 97 |
| 5.3 | Magnitude $ s_{\zeta,21}^{(LM)} $ averaged over a 2-GHz frequency band versus the central frequency of the frequency band of the experimental result (red), and the ν parameter of the best-matched Rice distribution (blue square). | 100 |
| 6.1 | Probability density functions of (a) the real part and (b) the imaginary part of the normalized impedance component $z_{n,11}$ from four sets of experimental data. The thicker solid curves represent measured results from the cut-circle cavity at 6.6 K (gray), the cut-circle cavity at 270 K (pink), the 1/4-bowtie cavity (light green), and the GigaBox (light blue). The dashed curves are the best-fit numerical results (from fits to $P(s_{n,21})$) to the four experimental results with the loss parameters shown respectively. | 106 |
| 6.2 | Probability density functions of the magnitude of the normalized scattering matrix components (a) $ s_{n,11} $ and (b) $ s_{n,21} $ from four sets of experimental data. The thicker solid curves represent measured results from the cut-circle cavity at 6.6 K (gray), the cut-circle cavity at 270 K (pink), the 1/4-bowtie cavity (light green), and the GigaBox (light blue). The dashed curves are the best-fit numerical results (from fits to $P(s_{n,21})$) to the four experimental results with the loss parameters shown respectively. | 107 |

| | | |
|-----|---|-----|
| 6.3 | Probability density functions of the phase of the normalized scattering matrix component $s_{n,21}$ from four sets of experimental data. The thicker solid curves represent measured results from the cut-circle cavity at 6.6 K (gray), the cut-circle cavity at 270 K (pink), the 1/4-bowtie cavity (light green), and the GigaBox (light blue). The dashed black curve is the uniform distribution. | 109 |
| 6.4 | The ensemble-averaged resistances $R_{avg,11}$ (blue), $R_{avg,22}$ (green), and $ R_{avg,12} $ (red) versus frequency in (a) the cut-circle cavity at 6.6 K over 72 realizations, (b) the cut-circle cavity at 270 K over 72 realizations, (c) the 1/4-bowtie cavity over 100 realizations, and (d) the GigaBox over 199 realizations. In all of these cases the condition $R_{avg,11}, R_{avg,22} \gg R_{avg,12} , R_{avg,21} $ is well satisfied for these data sets. | 112 |
| 6.5 | The averaged variance ratios of the impedance matrix before the RCM normalization (Ξ_Z , red circles) and after the RCM normalization (Ξ_{z_n} , green squares) from the four sets of experimental data. The blue curve is the theoretical prediction for Ξ_{z_n} versus the loss parameter α [55]. The light blue stars with error bars are the numerical data with the same ensemble sizes as the measured data. The black diamond with an error bar is the numerical result with many more samples (40001 realizations). The horizontal axis is on a logarithmic scale. | 113 |
| 6.6 | The averaged variance ratios of the scattering matrix before the RCM normalization (Ξ_S , red circles) and after the RCM normalization (Ξ_{s_n} , green squares) from the four sets of experimental data. The horizontal axis is the loss parameter α on a logarithmic scale. The blue dashed line is the theoretical prediction of Ξ_S for $\alpha \gg 1$ | 116 |
| 6.7 | The PDFs of the transmittance τ in (a) the cut-circle cavity at 6.6 K and (b) the 1/4-bowtie cavity. Shown are the experimental data (solid red) and the numerical data (dashed blue). The thin green curve in (a) is the RMT prediction for the lossless case. | 119 |
| 6.8 | The PDFs of the normalized thermopower \tilde{P}_{th} in (a) the cut-circle cavity at 6.6 K and (b) the 1/4-bowtie cavity. Shown are the experimental data (solid red), the RMT numerical data (dashed blue), and the best-fit Gaussian distributions (dashed green) to the experimental data. | 121 |
| 6.9 | The PDFs of the normalized thermopower \tilde{P}_{th} in the cut-circle cavity at 6.6 K. Shown are the experimental data (solid red) and the RMT numerical data with additional noise in $s_{rmt,21}$ (dashed blue). Compare to Fig. 6.8(a). | 123 |
| 7.1 | Mixed two-dimensional billiards: (a) a cut-circle with a circular insert, (b) an annular billiard, (c) a 1/2-mushroom billiard, and (d) a 1/2-mushroom billiard with a triangular stem. | 127 |
| 7.2 | The short orbit amplitude versus the orbit length in one realization of the two-port 1/4-bowtie cavity with two perturbers. | 135 |

| | | |
|-----|---|-----|
| 7.3 | (a) The 1/4-bowtie cavity, the two ports (red dots), and the two perturbers (blue circles). The wave source probability distributions are shown as (b) with the information of one short orbit, (c) with the information of two short orbits, and (d) with the information of four short orbits. In each case, the longest orbit length is shown, and the white star indicates the correct position of the wave source. | 137 |
| A.1 | Shown are examples (blue circles) of (a) $z_{rmt,11}$ with $\alpha = 0.1$, (b) $z_{rmt,12}$ with $\alpha = 0.1$, (c) $z_{rmt,11}$ with $\alpha = 1.0$, and (d) $z_{rmt,12}$ with $\alpha = 1.0$ in the complex plane. Each plot has 10000 samples from Eq. A.1, and $M = 10^6$ | 141 |
| A.2 | Shown are (a) frequency-dependent $z_{rmt,11}$ (light blue) and $z_{rmt,22}$ (red) and (b) $z_{rmt,12}$ (blue) in the complex plane. The numerical results are generated as a single realization of the frequency window 9 – 11 GHz with the loss parameter $\alpha = 0.8$ and the two-dimensional cavity area $A = 0.112 \text{ m}^2$ using Eq. A.2. | 143 |
| A.3 | A short orbit with two bounces. The red dots are the source port and the target port. The billiard walls (gray) are only shown near the bounces for illustration, and they can be straight segments or circular arcs. | 147 |
| A.4 | An example of the port-crossing detection. The two solid lines are trajectories launching at angle $\theta_{so,1}$ and angle $\theta_{so,2}$, and the dashed line represent the true orbit between them. | 148 |
| B.1 | Illustrations of the Thru, Reflect, and Line standards. The left transmission lines are terminated with a male connector, and the right transmission lines are terminated with a female connector. The Reflect standard consists of one male reflector and one female reflector. The Line standard is a transmission line with a male connector and a female connector in its two ends. | 153 |
| B.2 | Schematic experimental setup of the <i>in-situ</i> broadband cryogenic calibration system. The five pairs of phase-matched coaxial cables have nearly identical length and are not shown to scale. For the phase-matched coaxial cables and TRL standards, the male (or female) connectors are illustrated. The microwave cavity has a female connector and a male connector for its two ports, respectively. | 157 |
| B.3 | Left: The Radiall cryogenic switches R591722605. Right: The copper clamp to mount the cryogenic switches on the cold plate. The pink arrow points the position for tightening the clamp by a screw. | 159 |
| B.4 | Left: The front of the cryogenic switch in the copper clamp. The coaxial cable in the center is connected to the network analyzer. The other coaxial cables around the center one are connected to the microwave cavity and TRL standards. Right: The back of the cryogenic switch in the copper clamp. The black and red wires are connected to the voltage controller to control the state of the switch. | 160 |

| | | |
|------|---|-----|
| B.5 | The magnitude of (a) $ S_{11} $ and (b) $ S_{21} $ with high-quality-factor resonances from 3 to 18 GHz of a single realization of the superconducting cut-circle cavity in the <i>in-situ</i> cryogenic calibration system. The data have been calibrated with the TRL calibration and corrected by the pseudo-Open method. | 163 |
| B.6 | The magnitude of raw measured scattering matrix element $S_{raw,11}$ (black solid curves) and $S_{raw,21}$ (red dash curves) versus frequency. (a) An example with the frequency band from 14.0 to 14.5 GHz plotted in linear scale; (b) another example with the frequency band from 15.5 to 16.0 GHz plotted in semi-logarithmic scale. | 165 |
| B.7 | The magnitude of TRL-calibrated $S_{TRL,11}$ (the black curve) and the pseudo-Open standard (the thicker light-blue curve) versus frequency. | 166 |
| B.8 | (a) The quasi-two-dimensional cut-circle microwave cavity in a three-dimensional perspective, showing the cavity dimensions, ports, and the perturber. (b) Projected two-dimensional view of the cut-circle billiard. | 167 |
| B.9 | Shown are 12 examples of different realizations of $\Sigma_1 = (S_{TRL,11} ^2 + S_{TRL,21} ^2)^{1/2}$ versus frequency in varied colors. | 168 |
| B.10 | The magnitude of TRL-calibrated and pseudo-Open-corrected $S_{PO,11}$ (the black solid curve) and $S_{PO,21}$ (the red dash curve) versus frequency. The horizontal blue line shows $ S = 1$ | 170 |
| B.11 | The probability density of (a) $ S_{11} $ and (b) $ S_{21} $ of the RMT predictions (thicker light-blue curves), the experimental data from the superconducting cut-circle cavity at 6.6 K with TRL-calibration (red dash curves), and the data with TRL-calibration and pseudo-Open correction (black curves). | 173 |
| C.1 | Four examples of the magnitudes of the impedance correction in the length domain $\varepsilon(l)$. The insets are the corresponding geometry of the labeled orbits and the corresponding error sources. The thick black lines correspond to walls coated with microwave absorber. | 177 |

List of Abbreviations

| | |
|---------------------------------------|---|
| $\underline{\underline{\mathbf{1}}}$ | identity matrix |
| α | loss parameter |
| $\beta_{b(n,m)}$ | number of bounces of the trajectory $b(n, m)$ |
| γ | dephasing rate of a quantum dot |
| $\tilde{\Delta}$ | normalized eigen-energy spacing |
| δ_μ | error in the mean of the normalized impedance eigenvalues |
| δ_σ | error in the standard deviation of the normalized impedance eigenvalues |
| $\varepsilon(l)$ | magnitude of the impedance correction in the length domain |
| ζ | short-orbit correction matrix |
| $\underline{\underline{\theta}}_{so}$ | launch angle of an orbit |
| κ | effective attenuation parameter |
| $\underline{\underline{\lambda}}$ | eigenvalue matrix of the eigenmode of a wave system |
| λ | wavelength |
| $\lambda^{(rmt)}$ | eigenvalues of a wave system |
| Ξ_S | variance ratio of the scattering matrix |
| Ξ_Z | variance ratio of the impedance matrix |
| τ | transmittance |
| φ_s | phase of the eigenvalue of the scattering matrix |
| Ψ | wave function of a quantum system |
| $\psi(\vec{r})$ | wave field as a function of position \vec{r} |
| A | area |
| $\underline{\underline{A}}_C$ | matrix of the weight coefficients of the chaotic portion |
| $\underline{\underline{A}}_I$ | matrix of the weight coefficients of the integrable portion |
| \vec{a} | vector of the incoming power waves |
| \vec{B} | magnetic field |
| \vec{b} | vector of the incoming power waves |
| $b(n, m)$ | index of trajectories which leave the n^{th} port and return to the m^{th} port |
| c | speed of light |
| $D_{b(n,m)}$ | geometrical factor of the trajectory $b(n, m)$ |
| d_{so} | threshold distance for determining short orbits |
| \vec{E} | electric field |
| E | energy |
| f | frequency |
| f_{bw} | frequency bandwidth |
| Δf | average spacing between resonant frequencies |
| \widehat{H} | Hamiltonian operator |
| $\underline{\underline{H}}$ | Hamiltonian matrix |
| h | crest height of waves |
| \hbar | reduced Planck constant |
| \hat{I} | vector of the port currents |
| i | $\sqrt{-1}$ |

| | |
|-----------------------------------|--|
| $\underline{\underline{K}}$ | reaction matrix |
| k | wave number |
| k_m^2 | m^{th} eigen-energies |
| Δk | mean spacing of the wave numbers |
| Δk_m^2 | mean spacing of the eigen-energies |
| $L_{b(n,m)}$ | length of the trajectory $b(n, m)$ |
| L_M | maximum of the length of short orbits |
| L_o | orbit length |
| $L_{port(n,m)}$ | port-dependent constant length between the n th port and the m th port |
| L_t | typical length scale |
| l | length |
| M | dimension of a random matrix |
| m | mass |
| N | number of the ports of a wave system |
| N_{so} | number of short orbits |
| $\underline{\underline{O_p}}$ | pseudo-Open standard |
| P_{th} | thermopower |
| \tilde{P}_{th} | normalized thermopower |
| \vec{p} | momentum |
| $p_{b(n,m)}$ | survival probability of the trajectory $b(n, m)$ |
| Q | quality factor |
| R | radius |
| $\underline{\underline{R_{avg}}}$ | real part of the ensemble-averaged impedance matrix $\underline{\underline{Z_{avg}}}$ |
| $\underline{\underline{R_{rad}}}$ | real part of the radiation impedance matrix $\underline{\underline{Z_{rad}}}$ |
| \vec{r} | position vector |
| $\underline{\underline{S}}$ | scattering matrix |
| $\underline{\underline{s_n}}$ | normalized scattering matrix |
| $\underline{\underline{S_{PO}}}$ | TRL-calibrated and pseudo-Open-corrected scattering matrix |
| $\underline{\underline{s_{rmt}}}$ | scattering matrix based on random matrix theory |
| $\underline{\underline{S_{TRL}}}$ | TRL-calibrated scattering matrix |
| T | absorption probability |
| t | time |
| $\underline{\underline{U}}$ | random unitary matrix |
| V | volume |
| \hat{V} | vector of the port voltages |
| \hat{V}^{in} | vector of the incoming voltage waves |
| \hat{V}^{out} | vector of the outgoing voltage waves |
| $V(\vec{r})$ | potential energy |
| $\underline{\underline{W}}$ | coupling matrix |
| $\underline{\underline{X_{avg}}}$ | imaginary part of the ensemble-averaged impedance matrix $\underline{\underline{Z_{avg}}}$ |
| $\underline{\underline{X_{rad}}}$ | imaginary part of the radiation impedance matrix $\underline{\underline{Z_{rad}}}$ |

| | |
|--------------------------------------|--|
| $\underline{\underline{Z}}$ | impedance matrix |
| $\underline{\underline{Z^{(0)}}}$ | impedance matrix of the original random coupling model |
| $\underline{\underline{Z^{(1)}}}$ | impedance matrix of the extended random coupling model |
| $\underline{\underline{Z_0}}$ | characteristic impedance matrix of the ports |
| $\underline{\underline{Z_{avg}}}$ | ensemble-averaged impedance matrix |
| $\underline{\underline{Z_{int}}}$ | impedance matrix of orbits of the ports in the integrable regions |
| $\underline{\underline{Z_{rad}}}$ | radiation impedance matrix |
| $\underline{\underline{Z_{soc}}}$ | short-orbit-corrected radiation impedance matrix |
| $\underline{\underline{Z_{wall}}}$ | measured impedance from the microwave cavity with specific walls exposed |
| $\underline{\underline{z_{cor}}}$ | impedance correction matrix |
| $\underline{\underline{z_n}}$ | normalized impedance matrix |
| $\underline{\underline{z_n^{(0)}}}$ | normalized impedance matrix of the original RCM |
| $\underline{\underline{z_n^{(1)}}}$ | normalized impedance matrix of the extended RCM |
| $\underline{\underline{z_n^{(LM)}}}$ | normalized impedance matrix of the RCM with the short-orbit correction |
| $\underline{\underline{z_{rmt}}}$ | perfectly-coupled impedance matrix or impedance matrix based on random matrix theory |
| CPW | coplanar waveguide |
| DUT | device under test |
| GOE | Gaussian orthogonal ensemble |
| GUE | Gaussian unitary ensemble |
| i.i.d. | independent and identically distributed |
| LOS | line-of-sight |
| LRM | Line-Reflect-Match |
| NLS | nonlinear Schrödinger equation |
| PDF | probability density function |
| RCM | random coupling model |
| RMS | root-mean-square |
| RMT | random matrix theory |
| SMA | subminiature version A microwave connector |
| SQUID | superconducting quantum interference device |
| TRI | time-reversal-invariant |
| TRIB | time-reversal-invariance-broken |
| TRL | Thru-Reflect-Line |
| VNA | vector network analyzer |

Chapter 1

Introduction

1.1 Motivation

Waves are a ubiquitous phenomenon in diverse branches of physics and engineering, including examples such as quantum waves, electromagnetic waves, and acoustic waves. Many practical applications related to wave phenomena confront a common challenge of wave propagation in a complicated environment. For example, wireless devices communicating with each other in a house or office space involves electromagnetic waves propagating in a complicated environment with scattering created by floors, walls, and furniture. Radio signals and cell phone signals propagating in a metropolis also confront complicated reflections and diffraction on buildings and trees. Quantum waves in an irregularly-shaped quantum dot or acoustic waves in a complex medium or enclosure are other instances of complicated wave systems.

For all applications, one first tries to find the exact solution of the wave propagation. However, the complexity makes the exact solution impractical to find, or once found, the solution is of little utility if small details in the scattering environment are changed. Therefore, it is often more practical to pursue a statistical approach. Random matrix theory has been utilized to successfully develop a statistical approach to wave properties of complex systems [1], which is initially applied

in nuclear physics and then broadly utilized in other wave systems.

Random matrix theory can describe the statistics of a wave property based on the universal physical symmetries of the wave system. For practical applications, one needs to combine predictions of random matrix theory with system-specific (nonuniversal) features of the wave system. In this dissertation, I focus on a statistical model, the random coupling model, originally developed in our group [2, 3]. The extended version of the random coupling model [4] connects the statistical predictions of random matrix theory to practical wave systems by taking account of the system-specific features, such as the radiation impedance and the short orbits. The random coupling model is valuable for many applications related to complicated wave systems, including wireless communications with electromagnetic waves, quantum dots with quantum waves, high power microwaves, energy focusing with microwaves or acoustic waves.

Our goal is to establish statistical predictions for different wave properties in complicated wave systems based on the extended random coupling model. In this dissertation, my contributions are firstly verifying the extended version of the random coupling model and secondly indicating practical applications of the extended random coupling model.

In the rest of this chapter, I first introduce the general wave equations in Sec. 1.2. Based on these wave equations, I explain the difficulties of solving them in a complicated environment, and then I introduce a popular solution, the statistical approach, in Sec. 1.3. In Sec. 1.4 I introduce the field of wave chaos in which researchers use random matrix theory and the features of chaotic dynamics to predict

the statistical properties of the wave scattering system in wave chaotic systems in the short-wavelength limit. I review random matrix theory (RMT) in Sec. 1.5. However, RMT is not enough to make predictions for a practical system unless one combines RMT with the system-specific features of the wave scattering system. The random coupling model (RCM) introduced in Sec. 1.6 is the approach I utilize to connect RMT to my experimental results in this dissertation. The experiments verify that the RCM is a complete model for many wave properties in a complicated wave scattering system. One example of the utility of the RCM is its application to the fading phenomenon in the wireless communication field. I introduce fading and its traditional statistical models in Sec. 1.7. Finally, in Sec. 1.8, I give an outline for the dissertation.

1.2 Wave Equations

In general one can describe waves by their wave propagation equations. For example, the Schrödinger equation

$$i\hbar \frac{\partial}{\partial t} \Psi = \widehat{H} \Psi \quad (1.1)$$

describes a quantum system, where Ψ is the wave function of the system, $i = \sqrt{-1}$ is the imaginary unit, \hbar is the reduced Planck constant, and \widehat{H} is the Hamiltonian operator. Another example is the electromagnetic wave equations

$$\frac{1}{c^2} \frac{\partial^2}{\partial t^2} \vec{E} = \nabla^2 \vec{E} \quad (1.2)$$

and

$$\frac{1}{c^2} \frac{\partial^2}{\partial t^2} \vec{B} = \nabla^2 \vec{B} \quad (1.3)$$

which describe the propagation of electromagnetic waves through a medium, where \vec{E} is the electric field, \vec{B} is the magnetic field, c is the speed of light in the medium, and ∇^2 is the Laplace operator.

In a large subset of wave-related problems where applying the technique of separation of variables of space and time is valid, one can describe the wave phenomenon by a variant of the linear, scalar wave equation (also known as the Helmholtz equation)

$$(\nabla^2 + k^2)\psi(\vec{r}) = 0, \quad (1.4)$$

where $\psi(\vec{r})$ is the wave field as a function of position \vec{r} ; k is the wave number $k = 2\pi/\lambda$, where λ is the wavelength. For instance, considering the non-relativistic Schrödinger equation for a single particle moving in an infinite potential well with the Hamiltonian

$$\widehat{H} = \frac{-\hbar^2}{2m}\nabla^2 + V(\vec{r}), \quad (1.5)$$

where m is the mass of the particle, and the potential $V(\vec{r})$ is constant V_0 in the potential well and $V(\vec{r}) \rightarrow \infty$ outside, the wave equation can be rewritten in the form of the Helmholtz equation via the ansatz

$$\Psi(\vec{r}, t) = \psi(\vec{r})e^{-iEt/\hbar}, \quad (1.6)$$

with

$$k^2 = \frac{2m}{\hbar^2}(E - V_0), \quad (1.7)$$

where E is the energy of the quantum state $\Psi(\vec{r}, t)$.

For the case of the electromagnetic wave, if the electric field can be written as

$$\vec{E}(\vec{r}, t) = \vec{E}(\vec{r})e^{i2\pi ft}, \quad (1.8)$$

where f is the frequency, then Eq. (1.2) can be rewritten in the Helmholtz form with $k = 2\pi f/c$. Therefore, solving the Helmholtz equation [Eq. (1.4)] is common in many physical and engineering applications related to waves.

To solve the Helmholtz equation [Eq. (1.4)] in a practical wave scattering system, which is an enclosure where the wave propagates, one needs to specify the boundary condition of the system. However, solving this equation can be difficult, particularly in the short-wavelength limit [5], where the solutions to the wave equation are very sensitive to the boundary conditions. The major motivation of this dissertation is to study this common but challenging condition, a complicated wave scattering system.

1.3 Statistical Approach

To solve the Helmholtz equation [Eq. (1.4)] with a specific boundary condition, it is difficult to find the exact analytic solutions unless the boundary condition has special geometric symmetry. For most practical problems, one usually uses numerical methods to obtain the approximate solution with errors below a specified limit [6]. For example, many researchers and engineers use the high frequency structure simulator (HFSS), a commercial program which uses the finite element method to solve electromagnetic structures, for antenna design, complex radiofrequency (RF) electronic elements design, or electromagnetic property simulation.

The computational complexity for an accurate solution to Eq. (1.4) strongly depends on the wavelength of the applied waves compared with the characteristic

length scale of the wave scattering system. When the applied wavelength is much smaller than the characteristic scale of the wave enclosure (the short-wavelength limit, known as the “semiclassical limit” in wave chaos), the computational complexity enormously increases because more details of the system become influential to the solution, so the computation could be infeasible. Even if the solution was feasible with the computation power of modern computers, there may be uncertainties in the locations of boundaries or in parameters specifying the system. The exact solution of the wave equation, or the desired wave quantities, will be extremely sensitive to changes of the details of boundary conditions and the uncertainties. Therefore, the solution for a special realization (including the geometrical configuration and the applied wavelength) of a system may not be useful in predicting that of another similar system.

Instead of seeking the exact solution of a complicated wave system in the short-wavelength limit by a numerical approach, which only represents the solution for a specific realization, researchers turned to statistical approaches. The predictions of a statistical approach are the statistical distributions of the desired wave quantities, and the results can represent the outcome of measuring an ensemble of realizations [7]. For example, in applications to the wireless communication field, boundary conditions are complicated due to the structure of buildings and time varying due to the motion of objects in the wave-propagation environment [8]. Therefore, researchers created empirical statistical models for the fading phenomenon of communication signals. For another example, RF coupling to a targeted sensitive electronic device within a large enclosure can be considered as a wave scattering problem in

the short-wavelength limit. In this limit, distributions of the electromagnetic field, or the induced voltage on the target, can vary dramatically even with a small rearrangement of the internal objects, a small change in the enclosure boundaries, or a change in frequency of the excitation [9]. Thus, rather than seeking solutions for specific systems, it is often convenient to create statistical models which reproduce generic properties of the system [10] that can predict the statistical properties of an ensemble of similar systems.

1.4 Wave Chaos

The statistical models we use in this dissertation are based on the theory in the wave chaos field, which was initiated in nuclear physics and quantum wave systems [10, 11]. The development of the wave chaos field can be traced back to Wigner's work in the 1950s [12, 13, 14, 15], concerning the statistics of the energy levels of large nuclei. Large nuclei are examples of complicated systems with extreme sensitivity to small changes, and therefore the exact solution is either inaccessible or may not be useful for predicting the properties of another similar system. To address this problem, Wigner replaced the complicated Hamiltonian matrix \underline{H} of the system with a random matrix from a suitable ensemble. He found that the statistical properties of the eigenvalues and eigenfunctions of these random matrices agree with those of real nuclei.

Wigner's approach later became the well-known "random matrix theory" in the nuclear reaction field [16]. In 1962 Dyson introduced new kinds of statistical

ensembles for the energy levels of complex systems [17]. Other researchers have extended the random matrix approach to other complicated systems in different fields, such as wave scattering [18], quantum systems [10, 11], acoustic waves [19, 20], quantum dots and mesoscopic systems [21, 22, 23], and microwave cavities [3, 11, 24]. The fundamental conjecture of random matrix theory is: useful statistics can be obtained by replacing the exact Hamiltonian or scattering matrices by random matrices drawn from an appropriate ensemble [1, 25]. Further details of random matrix theory (RMT) will be discussed in Sec. 1.5.

Since Wigner’s work, applying statistical approaches to quantum wave equations has become a very active area in theoretical physics, where the field has been called “quantum chaos” [10, 11]. The quantum aspect can actually be generalized to all kinds of waves, hence a better terminology, emphasizing the generality of the issues addressed, might be “wave chaos” [26, 27, 28]. In general this field utilizes a statistical approach to understanding the wave properties of complicated systems. In addition to solving wave systems with the RMT approach, quantum chaos studies how to include classical chaotic dynamics in the quantum theory description in the semiclassical limit [10, 11].

1.4.1 Classical Chaos and Wave Chaotic Systems

Combining the ideas of chaos and waves is not straightforward. Classical chaos is characterized by the fact that small differences in the initial conditions of a dynamical system grow exponentially in time [5, 27]. For example, considering

a vacuum-filled uniform two-dimensional cavity, classical particles move in straight lines in the cavity and bounce specularly on the boundary. Such dynamical systems are called “billiards” and have been studied as a paradigm of particle motion in Hamiltonian mechanics [29]. The equations of motion of a particle in a billiard can be written as

$$H = \frac{\vec{p} \cdot \vec{p}}{2m} + V(\vec{r}), \quad (1.9)$$

where H is the Hamiltonian of the particle, \vec{p} is the particle momentum, m is the particle mass, and $V(\vec{r})$ is the potential. The potential $V(\vec{r}) = 0$ for the position \vec{r} in the billiard, and $V(\vec{r}) \rightarrow \infty$ elsewhere. Note that Eq. 1.5 is a quantum mechanical version of this equation.

The motion of particles in a billiard can be separated into three categories: (i) integrable, (ii) chaotic, and (iii) mixed, depending on the shape of the billiard [29]. Figure 1.1 illustrates several examples of these three types of billiards. Considering the trajectory of the particle motion, if one randomly choose two particles with slightly different positions (\vec{r}) or momentums (\vec{p}) as their initial conditions, with probability one, the difference (on average) grows linearly with time in an integrable billiard. However, with probability one, the difference of the randomly chosen particles (on average) grows exponentially with time in a chaotic billiard. For a mixed billiard, there is a finite amount of probability that the difference grows as the integrable case, and also a finite amount of probability that the difference grows as the chaotic case.

On the other hand, for wave scattering systems, the linear wave equations do

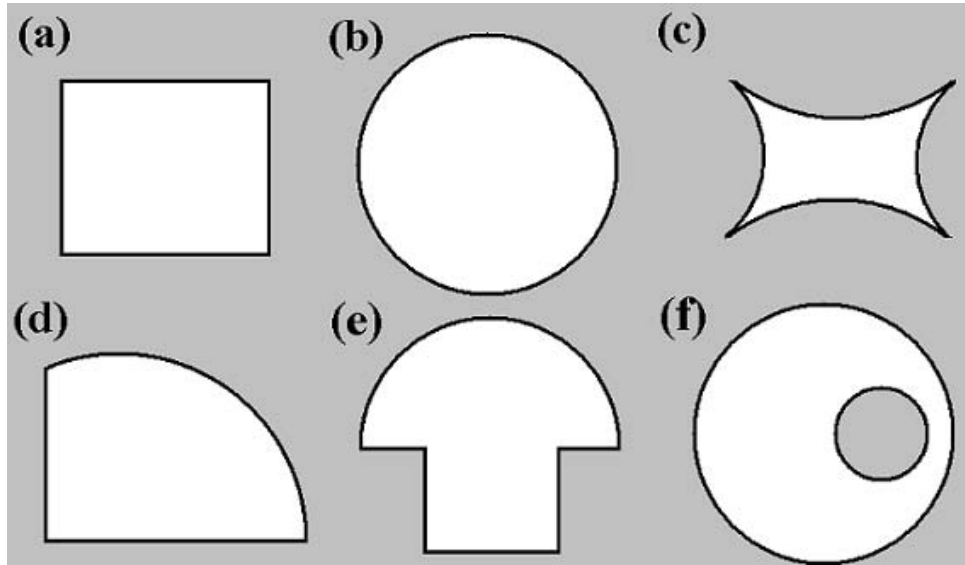


Figure 1.1: Two-dimensional billiards: (a) a rectangular billiard (integrable), (b) a circular billiard (integrable), (c) a bowtie billiard (chaotic) with four inward circular arcs, (d) a cut-circle billiard (chaotic) as a circle with two straight cuts, (e) a mushroom billiard (mixed) as a semicircle with a rectangular stem, and (f) an annular billiard (mixed) as the region between two eccentric circles.

not demonstrate an exponential sensitivity to initial conditions. One may ask how a wave system described by linear wave equations becomes chaotic. The answer is: a wave chaotic system is a wave scattering system with a chaotic-shaped boundary, for example, the billiards in Fig. 1.1(c) and (d). Although the wave equation is not chaotic, if the wavelength is very short compared to the typical length scale of the wave scattering system, the so-called “semiclassical limit”, the wave behavior can be well approximated by ray equations [11, 30]. Then the ray equations will be the same as the equations of motion of classical particles in a chaotic billiard. Since the ray equations are a nonlinear Hamiltonian system, ray trajectories can be chaotic [26, 31].

Wigner’s original setting (the energy levels of large nuclei) was a complicated wave system, and the complexity invoked the statistical hypothesis. Subsequently it was proposed that a wave chaotic system (even though the boundary shape is apparently simple) might satisfy the Wigner hypothesis [25, 28, 32, 33]. The proposal had been tested numerically [25, 28, 32] and later experimentally in electromagnetic cavities [26, 31, 34] and found to be valid. Therefore, we also use wave chaotic systems to test random matrix theory and the random coupling model in this dissertation, and we presume the results in wave chaotic systems can be further applied in practical complicated wave systems, without proving that the boundary of the system is ray-chaotic.

1.4.2 Microwave Billiard Approach

As the examples in the beginning of this chapter demonstrate, the Helmholtz equation [Eq. (1.4)] is a general equation which may describe a quantum wave system or an electromagnetic wave system. Due to the equality of the mathematical expressions, many researchers use chaotic microwave billiards to represent quantum systems of potential wells or quantum dots with a chaotic shape [24, 35, 36]. These wave chaotic systems are microwave cavities, and the behavior of the wave system in the short-wavelength limit is described by chaotic ray trajectories [36]. In this dissertation I introduce three microwave cavities as our experimental wave chaotic systems. Two of them are quasi-two-dimensional, and that means the scale of the cavity in the \hat{z} direction is smaller than the applied wavelength. Therefore, one can only consider the wave fields as $\psi(x, y)$, and a quasi-two-dimensional cavity can be a good analog of the two-dimensional quantum potential well.

Note that the wave chaos can be extended to three-dimensional systems, and we also do experiments in a three-dimensional microwave cavity. More details of the microwave cavities will be introduced in Chapter 3. Note that here we consider wave systems with uniform potential inside and specular reflections on the boundary (billiards). Although our explicit considerations in this dissertation are for billiard systems (i.e., scattering regions that are homogeneous with perfectly reflecting walls), presumably these effects may also be present with continuous potentials (i.e. soft walls [37]) and are not limited to billiards. In practical systems, there might be diffraction and ray-splitting in the wave enclosure, as well as dif-

fuse reflections on the boundary. We presume these situations would increase the complexity and make the statistical approach more valid.

In this dissertation, we use microwave experiments in wave chaos systems to test universal statistical properties predicted by the wave chaotic theory, namely random matrix theory. The study of random matrix theory (RMT) is a highly developed field, and applications of RMT have been found in many different scientific and engineering disciplines [1, 38]. Researchers have applied RMT as a statistical approach to model the scattering behavior of an ensemble of wave chaotic systems coupled to the outside world through scattering channels [39, 40, 41]. More introduction of RMT is given in the next section.

1.5 Random Matrix Theory

Random matrix theory (RMT) applied to wave systems is based on the assumption that many statistical properties of a sufficiently complex wave system are generic. It means that these properties do not depend on the details of a system, but rather depend only on underlying physical symmetries. This assumption has been tested in many different fields, and RMT has successfully been applied in many applications [5], such as chaotic quantum systems [42], quantum networks [43, 44, 45], or wireless communications in a complicated scattering environment [40, 46].

For a wave system with unknown or complex dynamics, RMT is invoked by treating the pertinent operator (typically the Hamiltonian, a scattering matrix, or an impedance matrix) of the system as an element of an ensemble of random matrices

[4]. The constraints on these random matrix ensembles only depend on the known physical symmetries of the system, and otherwise the ensembles are assumed to be completely random [47]. Here we introduce Wigner's random matrix ensembles for the Hamiltonian operator. In Chapter 2 we will discuss how to use RMT to generate random impedance matrices of wave scattering systems.

There are several constraints on the random matrices [4], for example, the geometric symmetries of the system, the time-reversal symmetry, and the group of symmetries related to half-integer spin [17]. Wigner introduced three types of wave chaotic systems with three different ensembles of random matrices respectively, the Gaussian orthogonal ensemble, the Gaussian unitary ensemble, and the Gaussian symplectic ensemble [13, 17]. For the microwave systems in this dissertation, I will focus on the first two systems with the presence or absence of time-reversal invariance. For systems with time-reversal invariance (TRI), the category is the Gaussian orthogonal ensemble (GOE). On the other hand, the category for systems with time-reversal invariance broken (TRIB) is the Gaussian unitary ensemble (GUE). The random matrices of these two ensembles have different statistics, so the desired wave quantities will have different statistical distributions. For example, Wigner had considered the $M \times M$ random Hamiltonian matrices $\underline{\underline{H}}$ and computed the eigenvalues k^2 of $\underline{\underline{H}}$. Wigner ordered them as $k_1^2 \leq k_2^2 \leq k_3^2 \leq \dots \leq k_M^2$, where k_m^2 is the m^{th} eigen-energy. Δk_m^2 is the mean spacing of the eigen-energy. For large M with $k_M^2 \gg \Delta k_m^2$, Wigner had found the distributions of the normalized eigen-energy

spacing

$$\tilde{\Delta}_m \equiv \frac{k_{m+1}^2 - k_m^2}{\Delta k_m^2} \quad (1.10)$$

are

$$P_{GOE}(\tilde{\Delta}) \simeq \frac{\pi}{2} \tilde{\Delta} e^{-\frac{\pi}{4} \tilde{\Delta}^2} \quad (1.11)$$

for the GOE case and

$$P_{GUE}(\tilde{\Delta}) \simeq \frac{32}{\pi^2} \tilde{\Delta}^2 e^{-\frac{4}{\pi} \tilde{\Delta}^2} \quad (1.12)$$

for the GUE case [2, 12, 13, 14, 15, 27]. Researchers have also found there are intermediate states where time-reversal invariance is partly broken between these two limits [10, 48, 49, 50, 51, 52, 53].

1.6 Random Coupling Model

In addition to eigen-energy spacing of large nuclei, random matrix theory [1] has achieved substantial success at predicting the universal statistics of many wave properties, including spectra, eigenfunctions [54], scattering matrices [55], impedance matrices, and conductances [56] of wave chaotic systems in the semiclassical limit [11]. However, the experimental applicability of RMT requires consideration of nonuniversal effects in practical situations. For example, in the particular case of scattering, the scattering system may have N ports, which are the scattering channels where the waves access this open wave scattering system. The scattering properties of an open system depend on the coupling between the field within the scattering region and the asymptotic incoming and outgoing waves connecting the exterior to the scatterer at the ports. The random coupling model (RCM) introduced

by Zheng, Antonsen, and Ott [57, 58, 59] is a stochastic model that incorporates nonuniversal coupling and port-specific effects into the analysis of short-wavelength scattering data for wave chaotic systems [36, 60].

Our group has extended the RCM by considering the short-orbit correction [39, 40, 41] which better describes practical systems. Further details of the short-orbit correction and the extended RCM will be introduced in Chapter 2, and the extended RCM is the main theoretical model of this dissertation. We have also introduced new applications of the RCM in the field of wireless communications, such as predictions of the statistics of the fading amplitude [61, 62]. The RCM model for fading can explain the statistics of the fading phenomenon more completely in different loss environments and also offers physical understanding for traditional empirical models of fading commonly used in wireless communications [8].

1.6.1 Random Coupling Model and Poisson Kernel

The random coupling model combines the universal predictions of RMT and the nonuniversal parts of the practical system in the impedance matrix $\underline{\underline{Z}}$ domain. The concept is similar to the Poisson kernel which combines the universal parts and the nonuniversal features in the scattering matrix $\underline{\underline{S}}$ domain [23, 24]. The advantage of the random coupling model is that nonuniversal contributions manifest themselves in $\underline{\underline{Z}}$ as simple additive corrections [39, 57, 58], and the expression is simpler than the expression for $\underline{\underline{S}}$ in the Poisson kernel [4, 63]. In addition, one can directly calculate the nonuniversal features of a system in the impedance description, rather

than relying on the more empirical Poisson kernel approach.

Impedance is a meaningful concept in electromagnetism, and it can be extended to all wave scattering systems. In a linear electromagnetic wave system with N ports, the $N \times N$ impedance matrix is the linear relationship of the vector \hat{V} of the port voltages and the vector \hat{I} of the port currents, via the phasor generalization of Ohm's law as [64]

$$\hat{V} = \underline{\underline{Z}} \hat{I}. \quad (1.13)$$

A cartoon of the linear wave system is shown in Fig. 1.2. The port voltages \hat{V} is a vector with elements V_1, V_2, \dots, V_N , and the port currents \hat{I} is a vector with elements I_1, I_2, \dots, I_N . A quantum-mechanical quantity corresponding to the impedance is the reaction matrix $\underline{\underline{K}}$, which is often denoted in the literature as $\underline{\underline{K}} = -i\underline{\underline{Z}}$ [2, 22, 54, 56, 65, 66]. The impedance matrix can also be related to the scattering matrix via the relationship [57, 58]

$$\underline{\underline{Z}} = \underline{\underline{Z}}_0^{1/2} (\underline{\underline{1}} + \underline{\underline{S}}) (\underline{\underline{1}} - \underline{\underline{S}})^{-1} \underline{\underline{Z}}_0^{1/2}, \quad (1.14)$$

where $\underline{\underline{Z}}_0$ is a $N \times N$ diagonal matrix which gives the characteristic impedance of the scattering ports, and $\underline{\underline{1}}$ is the identity matrix. The diagonal element $Z_{0,nn}$ is the characteristic impedance of the n^{th} port. In this dissertation we assume that lossless transmission lines attached to the ports, and $Z_{0,nn}$ are real for all ports. In our experiment, $Z_{0,nn} = 50 \Omega$. The scattering matrix $\underline{\underline{S}}$ specifies the linear relationship between the incoming power waves \hat{a} (a vector with elements a_1, a_2, \dots, a_N) and the outgoing power waves \hat{b} (a vector with elements b_1, b_2, \dots, b_N), as [64]

$$\hat{b} = \underline{\underline{S}} \hat{a}. \quad (1.15)$$

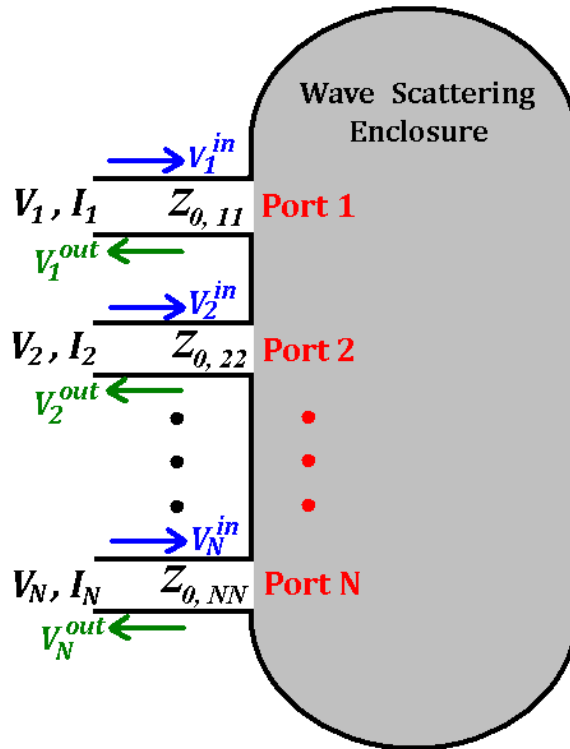


Figure 1.2: An N -port network system as the model of the N -port wave scattering enclosure. The voltage V_n appears on the n^{th} transmission line of characteristic impedance $Z_{0,nn}$, carrying the current I_n . The incoming (V_n^{in}) and outgoing (V_n^{out}) voltage waves offer a complementary description of the situation at the n^{th} port.

The n^{th} elements of incoming and outgoing power waves are

$$a_n = \frac{V_n^{\text{in}}}{\sqrt{Z_{0,nn}}} \quad (1.16)$$

and

$$b_n = \frac{V_n^{\text{out}}}{\sqrt{Z_{0,nn}}}, \quad (1.17)$$

where V_n^{in} and V_n^{out} are the incoming and outgoing voltage waves at the n^{th} port, respectively [64].

The Poisson kernel characterizes the probability density for observing a particular scattering parameter S in terms of the average scattering parameter $\langle S \rangle$ [24]. $\langle S \rangle$ represents contributions to the scattering behavior from elements of the system which are not random, such as the prompt reflection from the interface between the scattering channel and the chaotic system. The scattering parameter can be generalized to a matrix for multiple-channel systems [67, 68, 69, 70, 71, 72, 73, 74, 75].

On the other hand, the random coupling model characterizes the nonuniversal features as the ensemble-averaged impedance matrix $\underline{\underline{Z_{avg}}}$. $\underline{\underline{Z_{avg}}}$ includes (i) the system-specific features of the ports, which we denote as the radiation impedance matrix, and (ii) the geometry of the wave scattering enclosure (including the positions of the ports and the shape of the boundary) which we encompass in the short-orbit effect. The details of these quantities will be introduced in Chapter 2. By combining all these features, the random coupling model becomes a complete statistical model for complicated wave scattering systems in the semiclassical limit.

1.7 Fading Models

Our group also studied applications of the RCM to fading statistics [61]. Considering wave propagation between a source and a receiver through a complex scattering environment, fading is the time-dependent variation in the received signal amplitude as the scattering environment changes and evolves with time [8]. Fading occurs because waves propagating via multiple paths or around obstacles interfere when they arrive at a receiver. A common example is the nighttime variation of AM radio signal reception in the presence of ray bounce(s) off a time varying ionosphere. Another common observation of fading is experienced by radio listeners in automobiles moving among vehicles and buildings in an urban environment. Although fading exists in closed or open scattering systems and in all types of wave propagation, such as electromagnetic waves, acoustic waves, and quantum waves, it has been most extensively studied in the wireless communication field [76, 77, 78, 79].

Because of the complexity of wireless communication environments, a precise mathematical description of the fading phenomenon is either unknown or too complex for tractable analysis [8]. Researchers have empirically designed statistical models for fading channels in particular scattering environments and frequency bands, and different (apparently unrelated) fitting parameters are introduced in different models. For example, the Rayleigh fading model applies a one-parameter Rayleigh distribution to model the fading amplitude in an environment where there is no line-of-sight (LOS) path between the transmitter and the receiver, such as mobile wireless systems in a metropolitan area [8, 76, 77, 78]. The Rice fading model,

on the other hand, applies a two-parameter distribution to model situations with a strong LOS path [8, 79, 80]. The detailed physical origins of these models, and their parameters, are not clear.

The complexity of the wave propagation environment is advantageous from the perspective of wave chaos theory because it means that wave propagation is very sensitive to details, and a statistical description is most appropriate. For applying wave chaos approaches, the system should be in the semiclassical limit where the wavelength is much shorter than the typical size of the scattering system [11]. Researchers have applied RMT in wireless communications [46] and in analyzing the information capacity of fading channels [81, 82, 83, 84], or directly to the fading phenomenon itself [61]. In this dissertation I will demonstrate that the RMT fading model is more complete than the Rayleigh and Rice fading models, which are recovered by the RMT model in the high-loss limit [61] in Chapter 5. I also present a thorough derivation of the RMT fading model in Appendix D.

1.8 Outline of Dissertation

In this chapter I have introduced the big picture of wave chaos research related to this dissertation. In the following chapters, I will go through the details of the theory, the experiments, and the novel contributions of this work. The structure of the following chapters is illustrated in Fig. 1.3. It can be separated into two groups. Chapters 2, 3, and 4, and Appendix A, B and C are the theoretical derivations, experimental systems, and the experimental verifications of the extended random

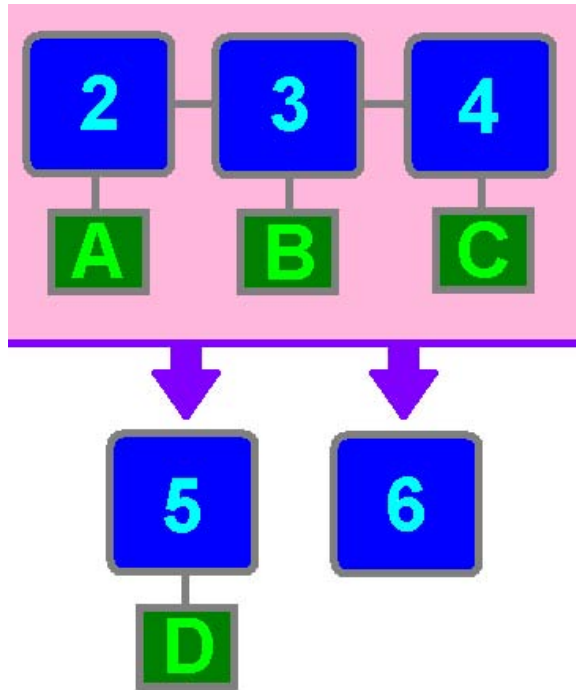


Figure 1.3: The structure of the chapters in this dissertation.

coupling model. Chapter 5, Chapter 6, and Appendix D are applications of the extended random coupling model.

Chapter 2 introduces the extended random coupling model, and it is the main theory we used in all of the experiments in this dissertation. I first introduce the original random coupling model which is developed by previous members of our group. Then I introduce the short-orbit correction which takes an additional system-specific feature, the short-orbit effect of wave scattering systems, into account and greatly expands the utility of the random coupling model. Numerical algorithms of how to generate random matrices and how to compute short-orbit contributions in

impedance are introduced in Appendix A.

Chapter 3 introduces all of the experimental systems we used for verifying the extended random coupling model and testing its applications. Three systems are introduced respectively. The first system is a quasi-two-dimensional microwave cavity with a 1/4-bowtie shape. The experiment is operated at room temperature, and the system shows moderate loss. The second system aims to achieve a much lower loss environment, so we use a quasi-two-dimensional superconducting microwave cavity, and the measurement is done in a cryogenic system. Details of the cryogenic system are separately addressed in Appendix B. For the third system, the major difference is that the cavity is three-dimensional, and it can be used to test the random coupling model and its applications in the more practical three-dimensional case.

In Chapter 4, we verify the short-orbit correction and compare the extended RCM with the original RCM in varied aspects. We first verify the short-orbit correction by the effect of individual short orbits in the first experimental system. A more detailed discussion of the error sources of this experiment is given in Appendix C. Then we compare the short-orbit correction with two other approaches to depict the system-specific features of a wave scattering system, which are the frequency smoothing and the configuration ensemble. In the end of Chapter 4, we show the benefits of applying the short-orbit correction by comparing the normalized results of the extended RCM and the original RCM.

After we verified the extended RCM, it is important to demonstrate its applications. In Chapter 5, I introduce the application of the extended RCM in the statistical model of fading. I first demonstrate how to build a fading model based on

the extended RCM. I also compare this model with the traditional fading models, such as the Rayleigh fading and the Rice fading. The results show that the fading model based on the RCM can explain the physical meaning of the parameters of the Rayleigh fading model and the Rice fading model. It also better describes the statistics of the wave scattering system in the low loss regime. In the high loss regime, I can show the RCM model goes over to the Rayleigh model and the Rice model, and the derivation is shown in Appendix D.

In Chapter 6, I further test the applications of the extended RCM. The extended RCM is a complete statistical approach that can predict the statistics of different properties of a wave scattering system with varied loss. These properties include the elements of the impedance matrix and the scattering matrix, the variance ratios of these quantities, and the transmittance. Furthermore, the statistics of the first-order energy derivatives of the scattering matrix and the impedance matrix are also well predicted. The first-order energy derivatives are related to the thermopower of a quantum dot.

In the end, Chapter 7 gives the conclusion of this dissertation and suggestions for future work. I also summarize the extended RCM and its applications. The future work section includes the interesting but incomplete projects related to our wave chaos research.

Chapter 2

Extended Random Coupling Model

The random coupling model (RCM) is a statistical model of impedance matrices of a complicated wave scattering system. It connects wave chaos theory to the measurement results of a practical system. The model combines the universal properties of the predictions of random matrix theory and the system-specific features of real-life wave scattering systems. In Sec. 2.1, I review the original random coupling model introduced by Zheng *et al.* [57, 58] which described one system-specific feature, namely the radiation impedance of the ports of the system. Hart *et al.* [4, 39] extended the random coupling model by replacing the radiation impedance with the ensemble-averaged impedance which includes additional short-orbit information of the wave system. This short-orbit correction will be reviewed in Sec. 2.2. The short-orbit information incorporates more fluctuating details in the frequency domain than the original radiation impedance, so the extended RCM can better predict the statistics of the practical measurement results than the original RCM in a narrower frequency band.

2.1 Original Random Coupling Model

The original random coupling model was introduced by Zheng *et al.* [57, 58]. They use the random plane wave hypothesis and random matrix theory (RMT)

to describe the statistical properties of the impedance matrix $\underline{\underline{Z}}$ of a complicated wave scattering system, and the system-specific features are incorporated through the radiation impedance matrix. On the other hand, the Poisson kernel combines the universal properties and the system-specific features in terms of the scattering matrix $\underline{\underline{S}}$ [24, 85]. The advantage of the random coupling model is that system-specific (nonuniversal) contributions manifest themselves in $\underline{\underline{Z}}$ as simple additive corrections [39, 57, 58], as compared to the Poisson kernel where the nonuniversal features are both in the numerator and the denominator of a fraction expression [4, 63].

We assume that the wave system is linear in all of our studies. Therefore, wave scattering in an enclosure can be modeled as a linear network system with N ports which act as the access channels of the waves. For an N -port system, the original random coupling model [57, 58] expresses the $N \times N$ impedance matrix as

$$\underline{\underline{Z}}^{(0)} = i\underline{\underline{X}}_{rad} + \underline{\underline{R}}_{rad}^{1/2} \left(\underline{\underline{z}}_{rmt} \right) \underline{\underline{R}}_{rad}^{1/2}. \quad (2.1)$$

This equation combines the universal fluctuating property predicted by RMT ($\underline{\underline{z}}_{rmt}$) and the system-specific features ($\underline{\underline{R}}_{rad}$ and $\underline{\underline{X}}_{rad}$). The superscript $(^{(0)})$ stands for the original version of the RCM. In the next two sections we discuss $\underline{\underline{z}}_{rmt}$, $\underline{\underline{R}}_{rad}$, and $\underline{\underline{X}}_{rad}$ in detail.

2.1.1 Perfectly-Coupled Impedance Matrix

The RMT part of the random coupling model can be expressed as

$$\underline{\underline{z}}_{rmt} = \frac{-i}{\pi} \underline{\underline{W}} \left(\underline{\underline{\lambda}} - i\alpha \underline{\underline{1}} \right)^{-1} \underline{\underline{W}}^T, \quad (2.2)$$

and we call it the perfectly-coupled impedance matrix. This form combines (i) the randomness of the eigenmodes in the wave enclosure ($\underline{\lambda}$, based on random matrix theory), (ii) the randomness of the coupling between the ports and the eigenmodes (\underline{W} , based on the random plane wave hypothesis), and (iii) the system-dependent feature, namely the loss parameter α . The coupling matrix \underline{W} is an $N \times M$ matrix where its element W_{nm} represents the coupling between the n^{th} driving port ($1 \leq n \leq N$) and the m^{th} eigenmode of the wave scattering enclosure ($1 \leq m \leq M$). \underline{W}^T is the transpose matrix of \underline{W} . Each W_{nm} is an independent Gaussian random variable of zero mean and unit variance. The statistics of W_{nm} is based on the random plane wave hypothesis [57], in which the wave scattering is assumed as a superposition of random plane waves, and it is justified by the complexity of the enclosure and the smallness of the wavelength compared to the enclosure size. The random plane wave hypothesis has also been used for waves in plasmas [86] and within the context of quantum mechanics of classically chaotic systems [87].

In Eq. (2.2), $\underline{\lambda}$ is an $M \times M$ diagonal matrix where its diagonal elements are the eigenvalues of the wave scattering enclosure. The statistics of these eigenvalues are based on RMT [1, 57]. α is the loss parameter of the wave system, and it will be further introduced in the following paragraphs. $\underline{1}$ is an identity matrix. Previous work focused on the statistics of the scattering matrix (\underline{s}_{rmt}) described by random matrix theory [21, 63]. With

$$\underline{z}_{rmt} = \left(\underline{1} + \underline{s}_{rmt} \right) \left(\underline{1} - \underline{s}_{rmt} \right)^{-1}, \quad (2.3)$$

Hemmady *et al.* have experimentally examined the statistics of \underline{z}_{rmt} and \underline{s}_{rmt} as a

function of the loss parameter and found excellent agreement with RMT [36, 60, 88, 89, 90]. In Appendix A.1, I introduce our numerical algorithm to generate random impedance matrices \underline{z}_{rmt} , and some examples of the elements of 2×2 \underline{z}_{rmt} matrices are shown. In Appendix D, Brouwer and Beenakker's method [21] of generating \underline{s}_{rmt} will be discussed in more detail.

The statistics of \underline{z}_{rmt} is a universal property that is independent of the system-specific features of a wave system. A single parameter governs the statistics of \underline{z}_{rmt} : the loss parameter α , which represent the (assumed uniform) distributed losses of wave scattering in the wave enclosure [57, 88]. The distributed losses mean losses that affect all modes in a frequency band almost equally, for example, wall losses and losses from a lossy dielectric that fills the wave system are considered distributed [2]. Moreover, Hemmady's semiclassical experiments in a microwave cavity showed that the loss of localized microwave absorbers can also be well described by the loss parameter [60]. The loss parameter is defined as

$$\alpha \equiv \frac{k^2}{\Delta k_m^2 Q}, \quad (2.4)$$

where k is the wave number of the operated wave. The wave number $k = 2\pi f/c$, where f is the frequency of the wave, and c is the speed of light. Δk_m^2 is the mean spacing of the eigen-energies (k_m^2), and it can be approximated by Weyl's formula in the limit of small wavelength compared to the system size. Weyl's formula is

$$\Delta k_m^2 \simeq \frac{4\pi}{A} \quad (2.5)$$

for two-dimensional systems, where A is the area of the enclosure, and

$$\Delta k_m^2 \simeq \frac{2\pi^2}{kV} \quad (2.6)$$

for three-dimensional systems, where V is the volume of the enclosure [91]. The quantity Q represents the quality factor of the wave system, and accounts for the losses within the enclosure (dielectric losses, ohmic losses, etc.) and the dissipation through the port [88]. The loss parameter can also be written as $\alpha = f/(2Q\Delta f)$, and it represents the ratio of the half width of the frequency resonances due to distributed losses in the enclosure ($f/2Q$) to the average spacing between resonant frequencies (Δf).

Other researchers also use similar parameters for representing the loss of the wave system. For example, Brouwer and Beenakker have derived the statistics of the scattering matrix \underline{s}_{rmt} based on RMT for a chaotic quantum dot [21]. They use a parameter γ , which represents the dephasing rate of a quantum dot. Hemmady *et al.* have shown the statistics of \underline{s}_{rmt} with the parameter γ are equivalent with the statistics of z_{rmt} in the random coupling model with $\underline{z}_{rmt} = (\underline{1} + \underline{s}_{rmt})(\underline{1} - \underline{s}_{rmt})^{-1}$ and $\gamma = 4\pi\alpha$.

2.1.2 Radiation Impedance Matrix

When applying wave chaos theory to practical systems, one needs to take account of the system-specific (nonuniversal) features of the wave system. One of the major contributions of the random coupling model is to combine the universal fluctuating feature (\underline{z}_{rmt}) with the system-specific features (\underline{R}_{rad} and \underline{X}_{rad}) in Eq. (2.1). In the original random coupling model, the system-specific features are embodied in the radiation impedance matrix \underline{Z}_{rad} [57, 58]. \underline{R}_{rad} and \underline{X}_{rad} are the real and the

imaginary parts of \underline{Z}_{rad} respectively, $\underline{Z}_{rad} = \underline{R}_{rad} + i\underline{X}_{rad}$.

The radiation impedance matrix captures the system-specific features of the ports of the wave scattering system. For the waves entering the enclosure at the ports, there are prompt reflections in general. If waves impinging at the ports are fully transmitted to the wave enclosure with no prompt reflections, the wave enclosure is said to be perfectly coupled to the outside environment through the ports. In practical wave systems, the coupling is a frequency-dependent feature due to the geometry of the ports, and thus it is difficult to directly compare the measured impedance matrix with the perfectly-coupled impedance matrix (\underline{z}_{rmt}) [3]. The original random coupling model encompasses the effect of prompt reflections in the frequency-dependent radiation impedance matrix $\underline{Z}_{rad}(f)$, which is the impedance measured at the ports when the boundaries of the enclosure are removed, so that the waves launched at a port propagate in the enclosure and never return to the port. Therefore, the radiation impedance matrix \underline{Z}_{rad} represents the radiation features of the ports. The real part \underline{R}_{rad} (radiation resistance) describes the radiation of power from the ports, and the imaginary part \underline{X}_{rad} (radiation reactance) describes the difference between the amounts of electric and magnetic energy stored in nonradiating fields near the ports [2]. Note that for the perfectly-coupling situation, $\underline{R}_{rad} = \underline{Z}_0$ and $\underline{X}_{rad} = 0$.

Hemmady *et al.* [36, 60] employed the original random coupling model to identify these nonuniversal features. In the semiclassical limit, their results [3] verify that the random coupling model (RCM) can represent wave systems composed of a wave scattering enclosure and probing ports coupling the outside world and the

scattering system. Note that, for a multiple-port system, Hemmady *et al.* considered the direct orbits between a pair of ports (see Fig. 2.1) as a part of the radiation impedance matrix, and this effect was represented in the off-diagonal terms of $\underline{\underline{Z_{rad}}}$ [88]. However, in this dissertation I treat the effect of the direct orbits in the short-orbit correction, which will be introduced in the next section, and therefore the radiation impedance matrix $\underline{\underline{Z_{rad}}}$ is diagonal, and each diagonal component represents the radiation of an isolated port. Another method to deal with the coupling between the scattering ports and the wave system is the Poisson kernel, which represents the nonuniversal features as an average $\langle \underline{\underline{S}} \rangle$ in the scattering matrix description [24, 85].

2.2 Short-Orbit Corrections to the Random Coupling Model

After the research of the original random coupling model, Hart *et al.* [39, 40, 41] introduced another system-specific feature, the short-orbit effect, and extended the random coupling model as

$$\underline{\underline{Z}}^{(1)} = i\underline{\underline{X_{avg}}} + \underline{\underline{R_{avg}}}^{1/2} \left(\underline{\underline{z_{rmt}}} \right) \underline{\underline{R_{avg}}}^{1/2}, \quad (2.7)$$

where the superscript $(^{(1)})$ stands for the extended version of the RCM. The difference is that the radiation impedance matrix $\underline{\underline{Z_{rad}}} = \underline{\underline{R_{rad}}} + i\underline{\underline{X_{rad}}}$ has been replaced by the ensemble-averaged impedance matrix $\underline{\underline{Z_{avg}}} = \underline{\underline{R_{avg}}} + i\underline{\underline{X_{avg}}}$. This new matrix quantity includes the radiation impedance and the short-orbit effect, and we will discuss the details in the following sections. The extended RCM can better describe the statistics of complicated wave systems than the original RCM. The experimental

verification will be shown in Chapter 4.

2.2.1 Short Orbits

A “short orbit” (or a “short ray trajectory”) means one ray trajectory whose length is not much longer than several times the characteristic size of the scattering enclosure, and the trajectory enters the scattering enclosure from a port, bounces (perhaps several times) within the scattering region, and then returns to a port. A “port” is the region in which there is a connection from the scatterer to the outside world. Note that the short orbits are different from periodic orbits [68, 92, 93], which are closed classical trajectories bouncing in a closed system. Short orbits, as defined here, are only relevant to open systems.

Figure 2.1 illustrates short orbits in a two-dimensional cut-circle billiard. In Fig. 2.1, the red dots represent the ports where the waves enter the billiard from outside. The circular perturber is a movable object for creating different boundary realizations. Colored lines are examples of short orbits. Note that the blue lines are direct orbits between the two ports. Dark green lines are one-bounce orbits, and light green lines are two-bounce orbits. Short orbits can also leave and return to the same port, such as the one-bounce orbit in purple. In these two realizations, the light green orbit in (a) is blocked in (b) due to the shift of the perturber. In general, the longer orbits have higher probability to be blocked by moving perturbers.

In practical experiments for measuring the statistics of wave scattering properties, one needs an ensemble measurement of many different realizations. Researchers

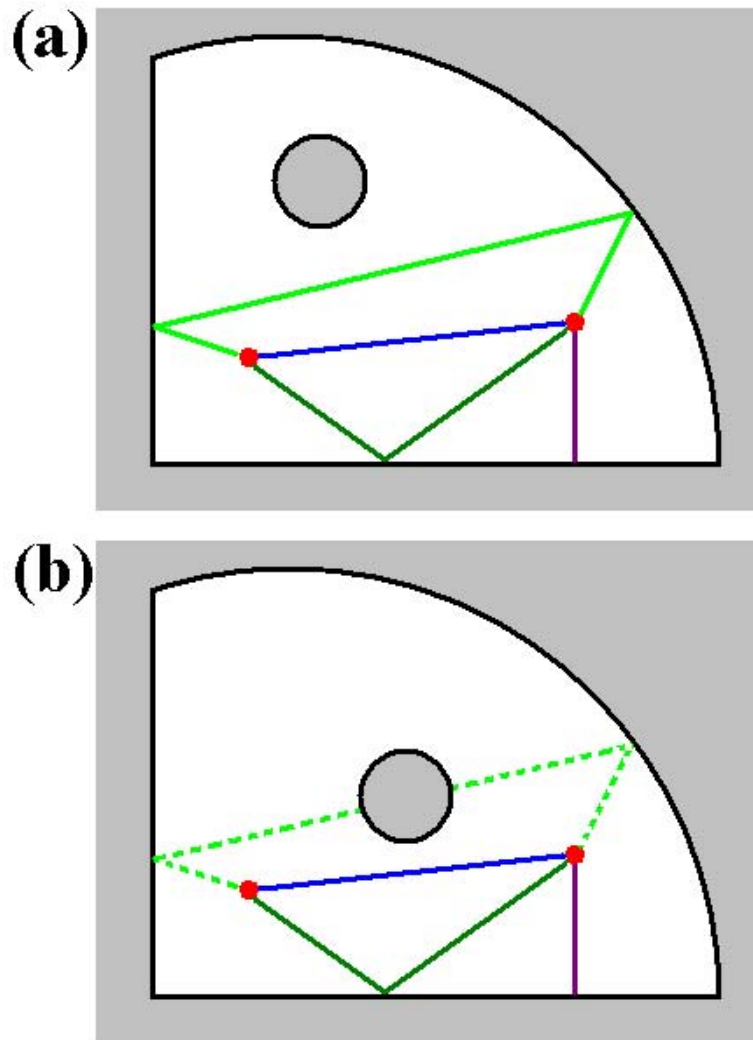


Figure 2.1: Illustrations of short orbits in a cut-circle billiard with a circular perturber. The red dots are the ports, black lines are the boundary of the billiard and the perturber, and colored lines are examples of short orbits. Note that the blue lines are direct orbits. The two-bounce orbit (light green) in (a) is blocked in (b) due to the shift of the perturber.

have typically (i) varied the geometrical configurations of the scattering enclosure (as the example in Fig. 2.1) and/or (ii) taken measurements at different frequencies [36, 51, 57, 58, 94]. These variations aim to create a set of systems in which none of the nonuniversal system details are reproduced from one realization to another, except for the effects of the port details. Thus, by suitably accounting for the port details (as the radiation impedance matrix in the RCM), it was hoped that only universal RMT properties remained in the ensemble data.

However, there can be problems in practice. For example, in the case of (i) geometrical configuration variation, researchers typically move perturbing objects inside a ray-chaotic enclosure with fixed shape and size [36, 57], or move one wall of that enclosure [51, 94], to create an ensemble of systems with varying details. The problem is that certain walls or other scattering objects of the enclosure remain fixed throughout the ensemble. Therefore, there may exist relevant ray trajectories that remain unchanged in many or all realizations of the ensemble. We term such ray trajectories, which leave a port and soon return to it (or another port) before ergodically sampling the enclosure, as “short orbits” or “short ray trajectories.” The influence of short orbits is also a problem for ensemble realizations with (ii) frequency variation. A orbit with short length (L_o) shows long-range oscillation in the frequency domain. Within a limited frequency range (f_{bw}), the variation of the phase accumulated by a wave following that short orbit may not be large enough to be considered random. In such a case ($f_{bw} < c/L_o$) the effect of specific (hence, nonuniversal) short orbits will survive the ensemble averaging processes.

The influence of short orbits makes systematic, nonuniversal contributions to

the ensemble data, and thus consideration of short orbits arises naturally in the semiclassical approach to quantum scattering theory [5, 11, 30, 95, 96, 97]. Previous work has examined short orbits in cases where the system and the ports can be treated in the semiclassical approximation [70, 74, 98] or considered the effect on eigenfunction correlations due to short orbits associated with nearby walls [73, 99]. Such short-orbit effects have been noted in microwave billiards [57, 58, 59] or for quantum transport in chaotic cavities [30, 100] and have either constrained or frustrated previous tests of RMT predictions. Microwave billiard experimental work has extracted a measure of the microwave power that is emitted at a certain point in the billiard and returns to the same point after following all possible classical trajectories of a given length [68]. The short-orbit effect on wave scattering properties of chaotic systems has been explicitly calculated in the case of quantum graphs [43] and for two-dimensional billiards [39]. Moreover, the Poisson Kernel approach can also be generalized to include short orbits [75] through measurement of a (statistical) optical \underline{S} matrix. Later, a general first-principles deterministic approach to experimentally analyzing the short-orbit effect is developed and verified by microwave billiard experiments [40, 41], which I will introduce in Chapter 4.

2.2.2 Semiclassical Approach to Short-Orbit Terms

Hart *et al.* [39, 41] extended the RCM by considered a port and its nearby walls as a generalized port. This method takes the information of the geometry of the system to compute the short-orbit contribution to the radiation impedance.

More specifically, the generalized system-specific impedance matrix (the short-orbit-corrected radiation impedance matrix) is written as

$$\underline{\underline{Z}}_{soc} = \underline{\underline{Z}}_{rad} + \underline{\underline{R}}_{rad}^{1/2} \underline{\underline{\zeta}} \underline{\underline{R}}_{rad}^{1/2}, \quad (2.8)$$

where $\underline{\underline{Z}}_{rad}$ is the diagonal radiation impedance matrix representing the features of the ports, $\underline{\underline{R}}_{rad}$ is the real part of $\underline{\underline{Z}}_{rad}$, and

$$\underline{\underline{\zeta}} \equiv \underline{\underline{\rho}} + i\underline{\underline{\chi}} \quad (2.9)$$

is the short-orbit correction matrix.

For the system with N ports, the (n, m) element of the $N \times N$ matrix $\underline{\underline{\zeta}}$ is [39, 41]

$$\zeta_{n,m} = \sum_{b(n,m)} \left\{ -p_{b(n,m)} \sqrt{D_{b(n,m)}} \exp[-(ik + \kappa)L_{b(n,m)} - ikL_{port(n,m)} - i\beta_{b(n,m)}\pi] \right\}, \quad (2.10)$$

where $b(n, m)$ is an index over all classical trajectories which leave the n^{th} port, bounce $\beta_{b(n,m)}$ times, and return to the m^{th} port. Note that for the off-diagonal term ($n \neq m$), $\zeta_{n,m}$ includes the direct orbit from the n^{th} port to the m^{th} port without bouncing on the walls ($\beta = 0$). In Appendix A.2, I introduce our numerical algorithm which can find short orbits in the billiard and compute the parameters $p_{b(n,m)}$, $D_{b(n,m)}$, $L_{b(n,m)}$, and $\beta_{b(n,m)}$ for each short orbit term.

In Eq. 2.10, $L_{b(n,m)}$ is the length of the trajectory $b(n, m)$. The effective attenuation parameter, $\kappa = k/(2Q) = \alpha\Delta k$, takes account of loss, where Q is the quality factor, α is the loss parameter, k denotes the wave number of a plane wave, and Δk is the average spacing between resonant wave numbers. $L_{port(n,m)}$ is the

port-dependent constant length between the n^{th} port and the m^{th} port, and it is a correction term for the orbit length required to explain the experimental results. In our experimental results, we constantly observe a frequency-dependent phase shift corresponding to a short-length transmission line in each port, so we add the correction term $L_{port(n,m)}$ in Eq. 2.10. More details of $L_{port(n,m)}$ will be introduced in Sec. 4.1.

The amplitude of each term in the sum [Eq. (2.10)] is determined by two quantities, where the orbit stability factor $D_{b(n,m)}$ is a geometrical factor of the trajectory, and it measures how the energy spreads out along the orbit path. This geometrical factor is a function of the length of each segment of the trajectory, the angle of incidence of each bounce, and the radius of curvature of each wall encountered in that trajectory. More details of computing $D_{b(n,m)}$ are introduced in Appendix A.2.2. In arriving at Eq. (2.10), it has been assumed that the port radiates isotropically from a location (several wavelengths) far from the boundaries of the wave enclosure, and the walls of the wave enclosure present perfect-metal boundary conditions with π phase shift on each bounce. These assumptions are well satisfied for the cavities used in our experiments.

The other quantity $p_{b(n,m)}$ is the survival probability of the trajectory due to the positions of the perturbing objects in the ensemble. For example, the light green orbit in Fig. 2.1(b) is blocked by the perturbing object. One can determine if an orbit is blocked by knowing the positions and the shapes of the perturbing objects. In Sec. 4.3, I introduce how we utilize perturbing objects in our experiment and how we determine $p_{b(n,m)}$.

With $\rho_{n,m} + i\chi_{n,m} \equiv \zeta_{n,m}$, the analytic continuations of $\rho_{n,m}$ and $\chi_{n,m}$ are

$$\rho_{n,m} = \sum_{b(n,m)} \left\{ -p_{b(n,m)} \sqrt{D_{b(n,m)}} \cos[-(k - i\kappa)L_{b(n,m)} - kL_{port(n,m)} - \beta_{b(n,m)}\pi] \right\}, \quad (2.11)$$

$$\chi_{n,m} = \sum_{b(n,m)} \left\{ -p_{b(n,m)} \sqrt{D_{b(n,m)}} \sin[-(k - i\kappa)L_{b(n,m)} - kL_{port(n,m)} - \beta_{b(n,m)}\pi] \right\}. \quad (2.12)$$

The short-orbit-corrected radiation impedance matrix is $\underline{\underline{Z}}_{soc} \equiv \underline{\underline{R}}_{soc} + i\underline{\underline{X}}_{soc}$, where

$$\underline{\underline{R}}_{soc} = \underline{\underline{R}}_{rad} + \underline{\underline{R}}_{rad}^{1/2} \underline{\underline{\rho}} \underline{\underline{R}}_{rad}^{1/2}, \quad (2.13)$$

$$\underline{\underline{X}}_{soc} = \underline{\underline{X}}_{rad} + \underline{\underline{R}}_{rad}^{1/2} \underline{\underline{\chi}} \underline{\underline{R}}_{rad}^{1/2}. \quad (2.14)$$

In the lossless case ($\kappa = 0$) $\underline{\underline{\rho}}$ and $\underline{\underline{\chi}}$ are the real and imaginary parts of $\underline{\underline{\zeta}}$; $\underline{\underline{R}}_{soc}$ and $\underline{\underline{X}}_{soc}$ are the real and imaginary parts of $\underline{\underline{Z}}_{soc}$. However, with uniform loss (e.g., due to an imaginary part of a homogeneous dielectric constant in a microwave cavity), $\underline{\underline{R}}_{soc}$ and $\underline{\underline{X}}_{soc}$ are the analytic continuations of the real and imaginary parts of the lossless $\underline{\underline{Z}}_{soc}$ as $k \rightarrow k + i\kappa$. These analytic continuations are no longer purely real (i.e., $\underline{\underline{\rho}}$, $\underline{\underline{\chi}}$, $\underline{\underline{R}}_{soc}$, and $\underline{\underline{X}}_{soc}$ become complex).

For the summation of orbit terms ($\underline{\underline{\zeta}}$, $\underline{\underline{\rho}}$, and $\underline{\underline{\chi}}$), the issue of convergence is worthy of discussion. Note that the sums in Eqs. (2.11) and (2.12) involve terms of the form sine and cosine of $[(k - i\kappa)L_{b(n,m)} + \dots]$ which for large $L_{b(n,m)}$ increase exponentially like $\exp(\kappa L_{b(n,m)})$. Although in the numerical tests of a bowtie billiard [39], we have observed that the parameters $p_{b(n,m)}$ and $D_{b(n,m)}$ decrease exponentially when $L_{b(n,m)}$ increases, the sums do not necessarily converge if the loss is too high. Accordingly, we will use a finite cutoff of the sum and regard the cutoff result as being asymptotic. In contrast, the sum involved in the calculation of

$\underline{\underline{\zeta}}$ [Eq. (2.10)] is now over terms that *decrease* exponentially with increasing path length as $\exp(-\kappa L_{b(n,m)})$. This sum is much more likely to converge than the sums in Eqs. (2.11) and (2.12).

The contribution of orbits decreases exponentially with the orbit length [39, 40, 41], so one can only take account of a finite number (N_{so}) of short (major) orbits by setting a threshold of the maximum length L_M . In practice, when considering either of the sums in $\underline{\underline{\zeta}}$, $\underline{\underline{\rho}}$, and $\underline{\underline{\chi}}$, we employ a cutoff by replacing the sums by $\sum_{b(n,m)}^{N_{so}}$ which signifies that the sum is now over all trajectories $b(n, m)$ with lengths up to the maximum length L_M , $L_{b(n,m)} \leq L_M$, and this is the reason of the name “short-orbit correction.” We use $\underline{\underline{\rho}}^{(L_M)}$, $\underline{\underline{\chi}}^{(L_M)}$, $\underline{\underline{\zeta}}^{(L_M)}$, $\underline{\underline{Z}}_{soc}^{(L_M)}$, $\underline{\underline{R}}_{soc}^{(L_M)}$, and $\underline{\underline{X}}_{soc}^{(L_M)}$ to indicate the finite length versions of those quantities. Combined with the measured radiation impedance ($\underline{\underline{R}}_{rad}$ and $\underline{\underline{X}}_{rad}$), these corrections ($\underline{\underline{R}}_{soc}^{(L_M)}$ and $\underline{\underline{X}}_{soc}^{(L_M)}$) can be analytically determined by using the ray-optics of short orbits between the ports and the fixed walls of the cavity.

Another way to estimate the nonuniversal features of a scattering system is by computing the averaged impedance matrix $\underline{\underline{Z}}_{avg} = \langle \underline{\underline{Z}} \rangle$ over all realizations of varied geometrical configurations. The universal fluctuations in $\underline{\underline{Z}}$ would cancel each other in the averaging, and only the nonuniversal parts remain. The ensemble-average impedance matrix $\underline{\underline{Z}}_{avg}$ is a frequency-dependent quantity just like $\underline{\underline{Z}}_{soc}$. In a lossy system $\underline{\underline{Z}}_{soc}^{(L_M)} \rightarrow \underline{\underline{Z}}_{avg}$ as L_M increases [39, 40, 41], and only a limited number of short orbits are required to represent system-specific nonuniversal features that survive the ensemble average. The experimental comparison of $\underline{\underline{Z}}_{soc}^{(L_M)}$ and $\underline{\underline{Z}}_{avg}$ will be shown in Chapter 4.

2.3 Chapter Summary

The extended RCM can represent the statistics of the impedance matrix $\underline{\underline{Z}}^{(1)}$ [Eq. (2.7)] by combining the universal fluctuating feature (\underline{z}_{rmt}) and nonuniversal features (\underline{Z}_{avg}). The perfectly-coupled impedance matrix \underline{z}_{rmt} can be generated by the Monte Carlo method according to RMT, and the statistics depend on only one parameter, the loss parameter α . The loss parameter can be determined by the experimental results [3]. The ensemble-averaged impedance matrix $\underline{\underline{Z}}_{avg}$ can be computed by averaging measured $\underline{\underline{Z}}$ matrices in varied geometrical configurations, or it can be approximated by $\underline{\underline{Z}}_{soc}^{(L_M)}$. The short-orbit-corrected radiation impedance $\underline{\underline{Z}}_{soc}^{(L_M)}$ includes the nonuniversal features of the radiation impedance, which can be measured, and the short orbits ($L_{b(n,m)} \leq L_M$), which can be analytically calculated with knowledge of the ports and enclosure geometry.

On the other hand, the extended RCM can be used as a normalization method for removing the system-specific features in the measured impedance matrix $\underline{\underline{Z}}$ as

$$\underline{z}_n = \underline{\underline{R}}_{avg}^{-1/2} \left(\underline{\underline{Z}} - i \underline{\underline{X}}_{avg} \right) \underline{\underline{R}}_{avg}^{-1/2}. \quad (2.15)$$

We use \underline{z}_n to denote the normalized impedance matrix, and correspondingly $\underline{s}_n = (\underline{z}_n - \underline{\underline{1}})(\underline{z}_n + \underline{\underline{1}})^{-1}$ is the normalized scattering matrix. The normalized impedance \underline{z}_n contains the remaining features of longer trajectories and the deviations between a single realization and the ensemble average. A longer length threshold (L_M) makes sure that more short-orbit effects are removed from the measured impedance, and the statistical distributions of normalized impedance are closer to the predictions of RMT (\underline{z}_{rmt}) [40, 41]. In Chapter 4, I also show the comparison of the statistics of

z_n and z_{rmt} .

In many of the wave related applications, one can treat the transmitters and the receivers of the system as ports and the wave propagating environment as the scattering enclosure. Therefore, with the extended random coupling model and $N \times N$ impedance matrices (or scattering matrices), one is able to model many statistical properties of a complicated wave scattering system, such as the reflection coefficient, transmission coefficient, conductances, impedances, scattering parameters, and fading amplitude.

Chapter 3

Experimental Systems with a Variety of Loss Values

The predictions of wave chaos can be applied in different types of waves, such as electromagnetic waves, acoustic waves, and quantum waves. Here we choose microwaves as an accessible wave source, and the wave scattering enclosures are simply metal cavities with movable perturbing objects inside. For the semiclassical limit, the typical length scales of the cavities are several times larger than the applied wavelengths. Sec. 3.1 shows the measurement of a quasi-two-dimensional microwave cavity made of copper by a network analyzer. It can be used to test the statistics of different wave scattering properties and the extended random coupling model (RCM) in the loss range from $\alpha = 0.3$ to $\alpha = 1.9$. In order to test the interesting features of the statistics of wave chaos in the low loss regime, we use a quasi-two-dimensional superconducting cavity and a cryogenic system which can reach the extremely low loss from $\alpha = 0.02$ to $\alpha = 0.2$. This system is introduced in Sec. 3.2. In Sec. 3.3, we further test the extended RCM in a three-dimensional cavity, and the loss range of this cavity is from $\alpha = 1$ to $\alpha = 10$.

3.1 Measurement of Ray-Chaotic Microwave Cavity

We use an Agilent PNA E8364C network analyzer to measure the frequency dependence of the complex 2×2 scattering matrix \underline{S} , and then we compute the

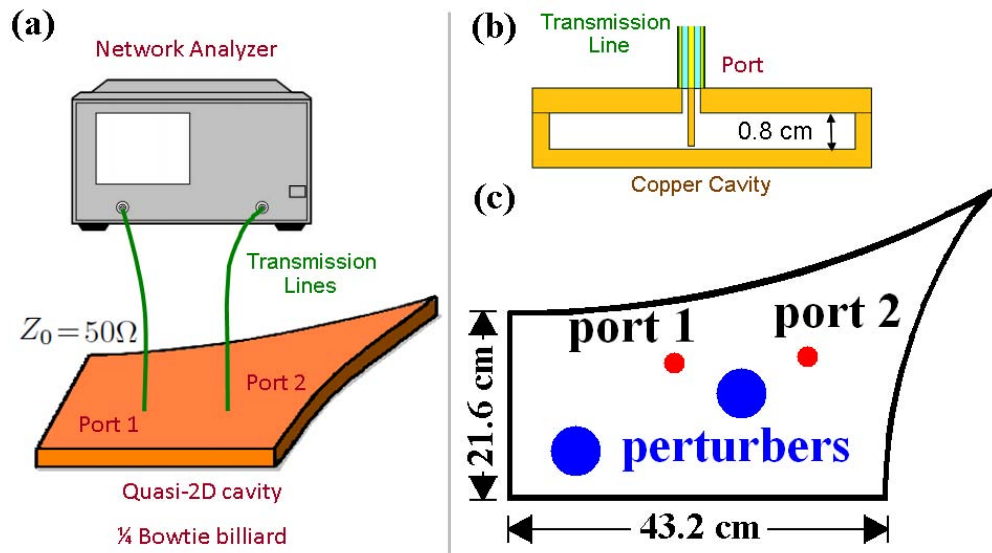


Figure 3.1: (a) The 1/4-bowtie cavity connected through two transmission lines to a network analyzer. (b) The side view of a port antenna and the cavity. (c) The top view of the 1/4-bowtie cavity with the two ports as red dots and the two metallic perturbers as blue circles.

corresponding impedance $\underline{Z} = \underline{Z}_0^{1/2}(\underline{1} + \underline{S})(\underline{1} - \underline{S})^{-1}\underline{Z}_0^{1/2}$. The measured results are frequency spectra of complex elements S_{11} , S_{12} , S_{21} , and S_{22} . We can change the sampling resolution in frequency and the incident wave power in the network analyzer. I will specify them in each experimental system. The network analyzer also has an averaging function to reduce the noise, and we set the averaging factor to 10.

The first experimental system is for measuring complex 2×2 scattering matrices \underline{S} in a quasi-two-dimensional ray-chaotic microwave cavity illustrated in Fig. 3.1. The cavity has two coupling ports [as the red dots in Fig. 3.1(c)], which can be treated as a transmitter and a receiver in the fading system. Microwaves are injected through each port antenna attached to a coaxial transmission line of characteristic impedance $Z_{0,11} = Z_{0,22} = 50\Omega$ [as the green lines in Fig. 3.1(a)], and each antenna is inserted into the cavity through a small hole (diameter about 0.1 cm) in the lid [shown in Fig. 3.1(b)], similar to previous setups [41, 88, 89, 90, 101, 102]. The effect of the transmission lines is calibrated by the Agilent N4691 electronic calibration module. The waves introduced are quasi-two-dimensional for frequencies (from 6 to 18 GHz, 48000 sample points) below the cutoff frequency for higher order modes (~ 19 GHz) due to the thin height of the cavities [0.8 cm in the vertical (\hat{z}) direction in Fig. 3.1(b)]. The wave power is 0 dBm. The 1/4-bowtie cavity is made of copper, and measurements of the transmission spectrum at room temperature suggest the loss parameter goes from $\alpha = 0.3$ to $\alpha = 1.0$, varying with the frequency range [40].

The shape of the cavity walls is chosen to create classical ray chaos. In Sec. 1.4 I have introduced ray-chaotic billiards [for example, Fig. 1.1(c) and (d)],

and these ray-chaotic systems have been used to test the application of RMT [25, 26, 28, 31, 32, 33, 34]. In this dissertation, we use wave chaotic systems to test RMT and the RCM. We perform the experiments in ideal ray-chaotic billiards, as opposed to real-life complicated wave systems, so that clear and definitive tests of RMT and the RCM can be accomplished. We presume that the results can be applied to practical complicated wave systems. The cavity is a symmetry-reduced “bowtie billiard” made up of two straight walls and two circular dispersing walls as in Fig. 3.1(c) [103]. The bowtie billiard has been previously used to examine eigenvalue [26] and eigenfunction [49] statistics of the closed system in the crossover from Gaussian orthogonal ensemble (GOE) to Gaussian unitary ensemble (GUE) statistics as time-reversal invariance is broken. In addition, this cavity has also been used to study scattering (\underline{S}), [41, 60, 88] impedance (\underline{Z}) [36, 41] and conductance (\underline{G}) [90] statistics. The length scales of the billiard (shown in Fig. 3.1) compared to the wavelengths of the microwave signals (1.7 – 5.0 cm) put these systems into the semiclassical limit (short-wavelength limit). The total area of the billiard is $A = 0.115 \text{ m}^2$, so the measured frequency range (6 – 18 GHz) includes about 1100 eigenmodes of the corresponding closed cavity. The quasi-two-dimensional eigenmodes of the closed system are described by the Helmholtz equation for the single nonzero component of electric field (E_z), and these solutions can be mapped onto solutions of the Schrödinger equation for an infinite square well potential of the same shape [11, 103].

3.1.1 Perturbers and Configuration Ensemble

To create an ensemble for statistical analysis, we add two metal perturbers to the interior of the 1/4-bowtie cavity and randomly move the perturbers to create 100 different realizations. Note that although we move the perturbers randomly, we keep the perturbers away (> 3 cm) from the ports to avoid affecting the radiation impedance of the ports. In each realization, we measure the scattering matrix over the frequency window (6–18 GHz). The average frequency shift of the resonances in different realizations is on the scale of the average frequency spacing. The perturbers are short prisms with about the same height of the cavity (0.7 cm). The purpose of these perturbers is to create different geometry configurations for a configuration ensemble, but the volume of enclosure remains the same as they move about. The perturbers can be considered scattering objects in the propagation medium, so changing the positions creates the equivalent of time-dependent scattering variations that give rise to fading. The walls are fixed relative to the ports in all realizations.

We made two pairs of perturbers for the experiments in the 1/4-bowtie cavity. They are shown in Fig. 3.2. The two irregular-shaped perturbers are made of iron and coated with aluminum foil with the maximum diameters 7.9 and 9.5 cm. The two circular cylindrical perturbers are made of aluminum with diameter 5.1 cm and an iron core in the center. Therefore, we can use a magnet held outside the closed cavity to translate and rotate the perturbers *in-situ*. The irregular-shaped perturbers was designed to further randomize the wave scattering within the cavity by preventing the formation of standing waves between the straight wall segments of



Figure 3.2: The two pairs of perturbers.

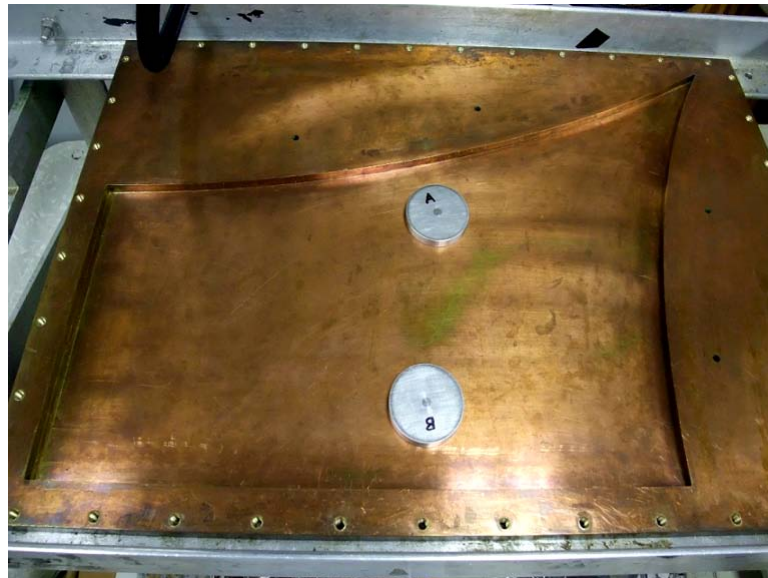


Figure 3.3: The two cylindrical perturbers in the 1/4-bowtie cavity without the lid.

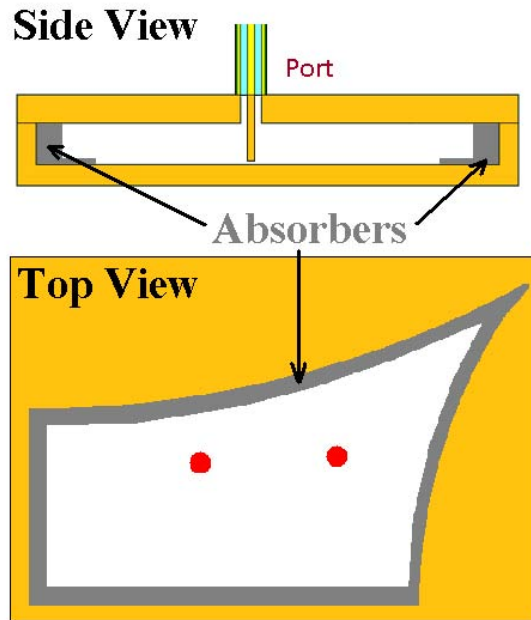


Figure 3.4: The arrangement of microwave absorbers for the measurement of the radiation impedance. The upper plot is the side view, and the lower plot is the top view. Microwave absorbers are represented as the gray material along the walls. The red dots represent the ports of the cavity.

the cavity and the perturbors [90]. Experimental results show no notable difference in the impedance statistics between using the irregular-shaped perturbors or the cylindrical perturbors [41].

3.1.2 Microwave Absorbers and Radiation Impedance

The radiation impedance \underline{Z}_{rad} can be experimentally determined by removing the perturbers, placing microwave absorbers along all the side walls of the cavity, and measuring the resulting impedance matrix. We use the DD-10017 microwave absorber made by ARC Technologies. The absorbers largely eliminate reflections from the walls (by > 10 dB for the frequency range 6 – 18 GHz), so this method removes the effect of ray trajectories bounced back from the walls, leaving only the effects of the port details.

Figure 3.4 illustrates the 1/4-bowtie cavity with microwave absorbers and without metal perturbers. The gray material along the side walls are microwave absorbers. In our measurement, we also add microwave absorbers on the floor near the side walls [see the side view in Fig. 3.4], and the purpose is to further reduce the reflected waves. Note that this measurement of the radiation impedance will also include the effect of the direct orbits between each pair of the ports. The experimental result is shown in Chapter 4.

3.2 Superconducting Cavity and the Cryogenic System

Many important wave chaos predictions for complicated wave scattering systems are in the low loss regime, such as the variance ratio of the scattering matrix and impedance matrix [90] and the statistics of the fading amplitude [61]. Further discussion of the theoretical predictions of fading is given in Chapter 5, and the variance ratio is discussed in Chapter 6. Here I focus on the experimental setup of

the extremely-low-loss system. This wave scattering system can reach the loss range from $\alpha = 0.02$ to $\alpha = 0.2$.

We have carried out experiments by measuring the complex 2×2 scattering matrix $\underline{\underline{S}}$ of a quasi-two-dimensional microwave cavity, illustrated in Fig. 3.5. There are two coupling ports (the red cylinders and dots in Fig. 3.5) where microwaves are injected through an antenna attached to a single-mode coaxial transmission line of characteristic impedance $Z_{0,11} = Z_{0,22} = 50\Omega$. Each antenna is inserted into the cavity through a small hole in the lid, similar to the setup of the 1/4-bowtie cavity. The waves introduced have frequencies from 3 to 18 GHz, and they are quasi-two-dimensional due to the thin height of the cavity (0.8 cm in the \hat{z} direction). For the low loss system, the frequency resonances are much sharper than the 1/4-bowtie cavity case, so we increase the frequency sampling resolution to 150000 points over the 15 GHz frequency band. We have applied wave powers of -10 dBm, 0 dBm, and 3 dBm to observe the effect of the wave power on superconductivity. The antennas are terminated with SMA microwave connectors, one male and the other female, on the surface of the cavity. The shape of the cavity is a symmetry-reduced “cut-circle” and is a billiard potential that shows classical chaos [61, 101, 102, 104].

The superconducting cavity is made of copper with Pb-plated walls and cooled to a temperature (6.6 K) below the transition temperature of Pb [101, 102, 105]. Measurements of the transmission spectrum suggest that the quality factor of the resonances is on the order of $Q \approx 10^5$. A Teflon wedge (the blue wedge in Fig. 3.5) can be rotated as a ray-splitting perturber inside the cavity, and we rotate the wedge by 5° each time to create an ensemble of 72 different realizations. The ray-

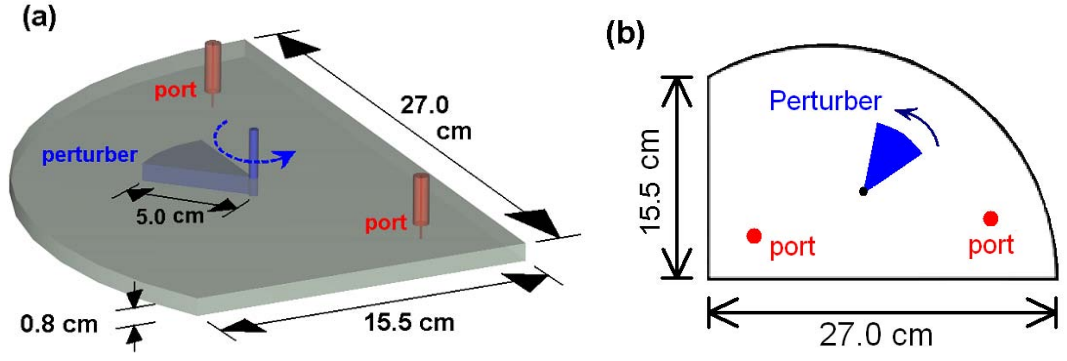


Figure 3.5: (a) The quasi-two-dimensional symmetry-reduced cut-circle microwave cavity in a three-dimensional perspective, showing the cavity dimensions, ports, and the perturber. (b) Projected two-dimensional view of the cut-circle billiard.

splitting and refraction due to the dielectric material can make the wave system more complicated. The rotation axis of the perturber is connected with a MDC vacuum rotary feedthrough (BRM-133) at room temperature, so we can control the angular position from outside the cryostat.

The measurements of the scattering matrix of the superconducting cavity are calibrated by an *in-situ* broadband cryogenic calibration system illustrated in Fig. 3.6. One major challenge of the cryogenic experiment is the calibration of the two transmission lines between the network analyzer and the superconducting cavity. Due to the limited space and the cold temperature, the convenient electronic calibration module, which we use in the room temperature measurement, cannot be applied here. Therefore, we use the Thru-Reflect-Line (TRL) calibration

method which is a manual calibration method by using three calibration standards [106, 107, 108]. In Fig. 3.6, the voltage controller, cryogenic switches, and the four additional electrical paths are all for the TRL calibration. More discussion of the cryogenic TRL calibration is given in Appendix B.

The cryostat includes two cylindrical vacuum chambers (aluminum) with one cylindrical thermal shield (copper) in between them. The switches, calibration standards, and the superconducting cavity are all contained in the inner vacuum chamber (designed temperature 4 K, radius 16.5 cm, and height 30.2 cm). We use an Alcatel Drytel 31 Dry Vacuum Pump System to evacuate the inner and outer chambers to a pressure lower than 1×10^{-6} atm and a Cryomech PT405 Pulse Tube Cryorefrigerator (with a water-cooled compressor) to cool down the cavity to the base temperature of 6.6 K. The cavity is hung on the cold plate of the cryorefrigerator, and we also use copper thermal straps to connect the cold plate and the cavity (Fig. 3.7). The thermometer is attached in the lower part of the outside surface of the cavity. We also designed two copper clamps to mount and thermally anchor the cryogenic switches on the cold plate. More details of the cryogenic switches are given in Appendix B. The second layer of the cryostat is the cylindrical copper shield (designed temperature 40 K, radius 17.8 cm, and height 43.8 cm). The third layer is the outer vacuum chamber (designed temperature 300 K, radius 20.3 cm, and height 55.9 cm). For a thermal cycle, it takes about one day to pump the system to vacuum and cool down the cavity to thermal equilibrium at the base temperature, while warming-up takes about two days. The dwell time of the system at the base temperature can be longer than one week.

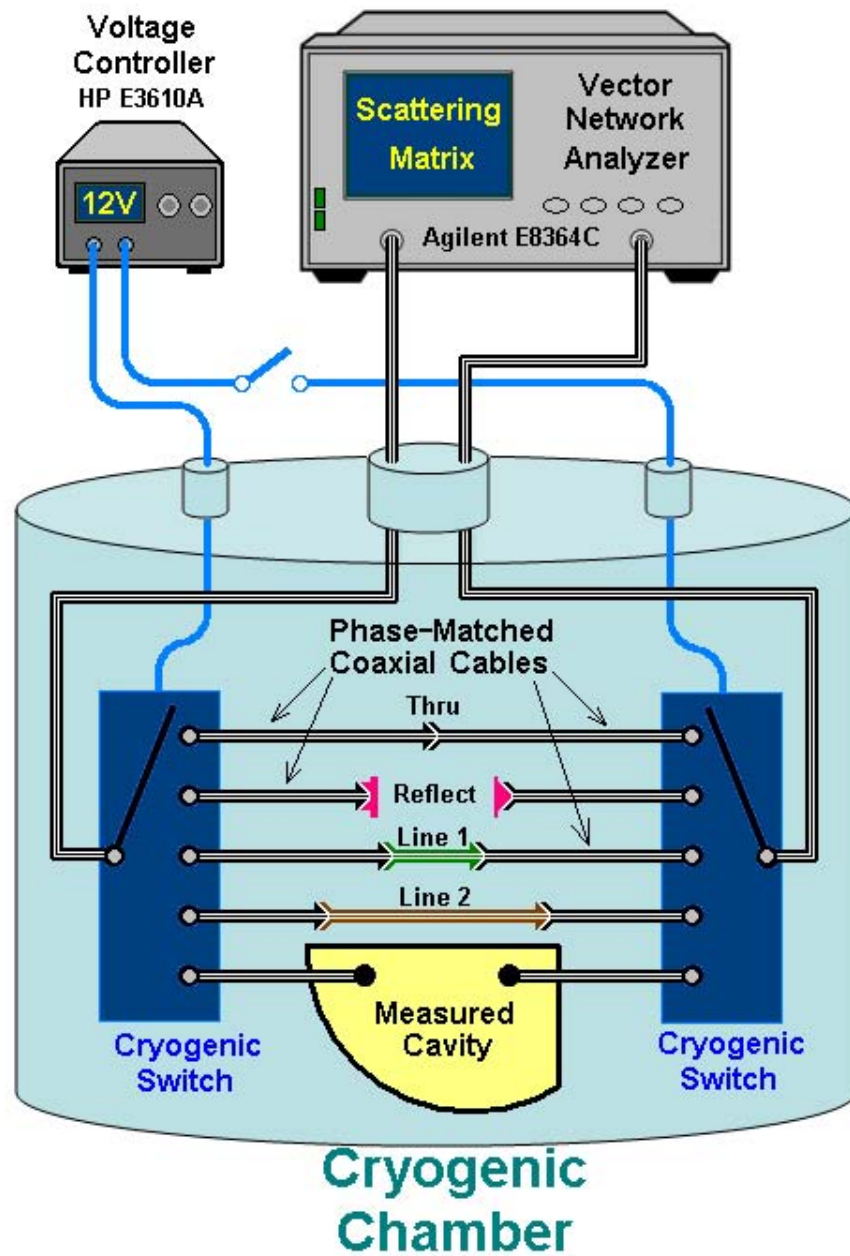


Figure 3.6: Illustration of the *in-situ* broadband cryogenic calibration system with the cut-circle cavity. Note that the phase-matched coaxial cables are not shown to scale.

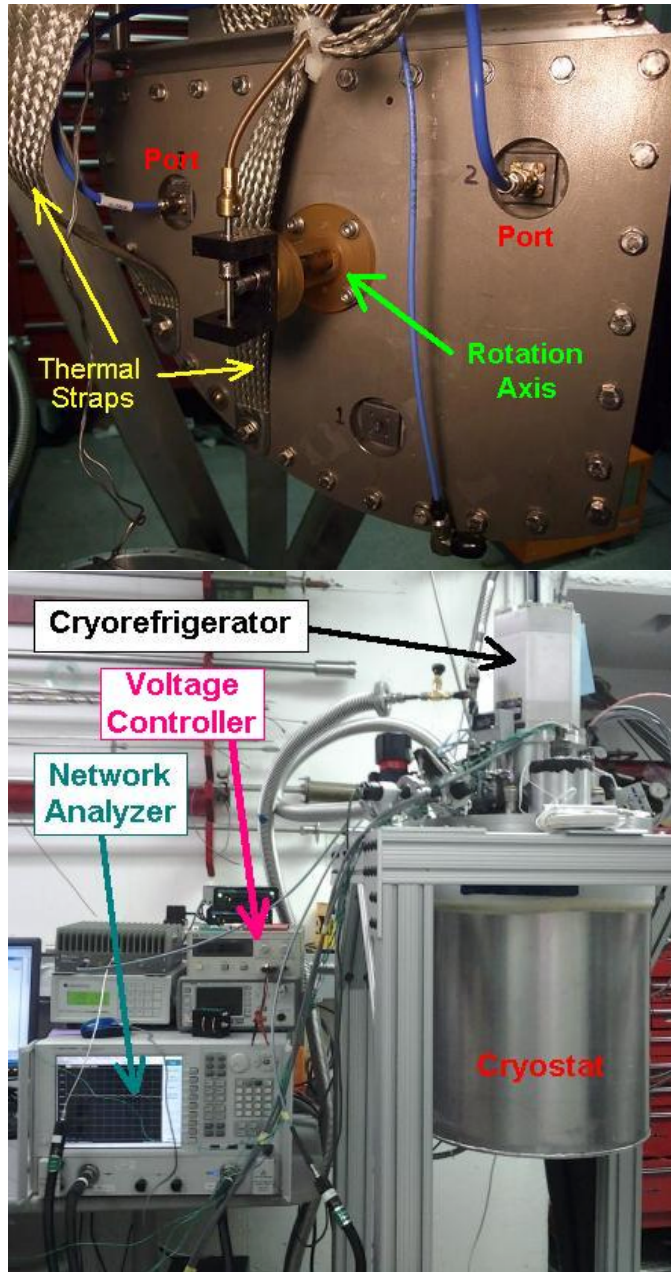


Figure 3.7: The upper picture shows the cut-circle cavity hanging in the cryostat. The thermal straps are connected to the 4K stage of the refrigerator on the top and to the cavity on the bottom. The lower picture shows the measurement system with the cryorefrigerator, the network analyzer, the voltage controller, and the cryostat labeled.

With this cryogenic system, we can measure and calibrate the 2×2 scattering matrices at different cavity temperatures and different powers of the incident microwave signals, and thus different loss parameter values. The equilibrium temperature of the cavity and the standards can be changed by tuning the applied DC current to heating resistors installed in the cryostat; the applied microwave power can be controlled by the network analyzer.

3.3 Three-Dimensional Cavity

The previous two wave systems are both quasi-two-dimensional cavities. In order to demonstrate that the random coupling model and wave chaos can be extended to three-dimensional cavities, we also do microwave experiments in a three-dimensional metal cavity. Biniyam Taddese and Matthew Frazier in our group have used the original version of this three-dimensional cavity to study the linear and nonlinear time-reversal mirror [109, 110]. We have cooperated with the Andreadis group at the U.S. Naval Research Laboratory, and they have built another cavity which is a nearly exact copy of our original version. Zachary Drikas *et al.* in the Andreadis group performed measurements in the new three-dimensional metal cavity, and I analyzed the data. The experimental results and the analysis will be shown in Chapter 6.

The experimental system is shown in Fig. 3.8. The complicated wave scattering enclosure is called the “GigaBox”. The GigaBox is approximately a rectangular microwave resonator with dimensions of length 1.27 m, width 1.22 m, and height

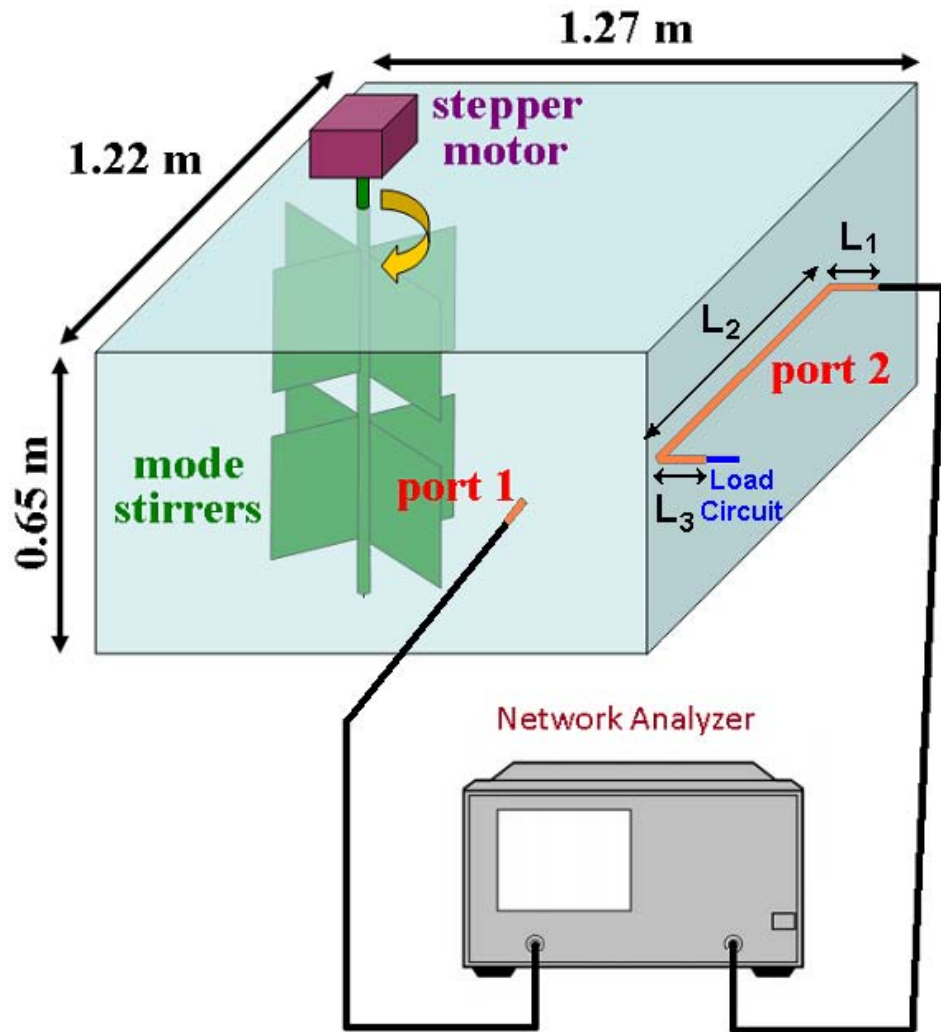


Figure 3.8: The experimental setup of measurement of the GigaBox as measured by the Naval Research Laboratory group.

0.65 m. The cavity is made of aluminum and has mode stirrers (perturbers made of aluminum) inside it. Even though the shape of this cavity is not ray-chaotic, the mode stirrers and the irregularities on the surface facilitate the creation of a complicated wave scattering system. A stepper motor is used to rotate the mode stirrers to create an ensemble of 199 different realizations. A network analyzer is connected to the two ports of the GigaBox and measures the scattering matrix in the frequency range 3 – 10 GHz, which is in the semiclassical limit.

Port 1 is a monopole antenna with a length 13 mm, mounted on the front wall of the GigaBox. Port 2 is an electronically-long U-shaped conductor with one end connected to the transmission line on the side wall of the GigaBox, and the other end terminated with a 50Ω load circuit. The U-shaped conductor is a copper tube of 6 mm diameter and total length 1156 mm, and the lengths of the three segments of the U shape are $L_1 = 127$ mm, $L_2 = 902$ mm, and $L_3 = 127$ mm (see Fig. 3.8).

In the three-dimensional case, the loss parameter $\alpha = k^3 V / (2\pi^2 Q)$. Due to the large volume ($V = 1.01 \text{ m}^3$), the GigaBox system has a high mode density and a high loss parameter. In addition, due to the k^3 term in α , this system has a wide loss parameter range ($\alpha = 1 - 10$) when the frequency varies from 3 to 10 GHz. Due to the high mode density, we use 16000 frequency points in a 100 MHz window. This experimental result will also be shown in Chapter 6.

Chapter 4

Verification of Short-Orbit Correction

Predicting the statistics of realistic wave-chaotic scattering systems requires, in addition to random matrix theory (RMT), introduction of system-specific information. The original random coupling model (RCM) combines the radiation impedance (\underline{Z}_{rad}) and the normalized impedance predicted by RMT (\underline{z}_{rmt}). The extended RCM further introduces the short-orbit correction on top of the original RCM to take account of these system-specific features.

In this chapter, we investigate experimentally the short orbits in a wave chaotic system, the 1/4-bowtie cavity open to outside scattering channels. In particular, we consider ray trajectories (orbits) of limited length that enter a scattering region through a channel (port) and subsequently exit through a channel (port). We examine the results in a one-port experiment and a two-port experiment. In the one-port experiment, we measure the 1×1 scattering matrix, or the scattering parameter; in the two-port experiment, we measure the 2×2 scattering matrix by a network analyzer. The frequency range is from 6 to 18 GHz, and therefore the ratio of the wavelength (λ) to the typical length scale (L_t) of the cavity is $\lambda/L_t \simeq 10$. This makes the wave system in the semiclassical limit.

We show that a suitably averaged value of the impedance can be computed from the short-orbit correction, and this can improve the ability to describe the

statistical properties of a scattering system. The compensation for the effects of short orbits improves the agreement between RMT-based predictions and measured statistical properties of the data from an ensemble of realizations or even a single realization. In Section 4.1 we consider the modification of the free-space radiation impedance arising in configurations when there are only a few possible short orbits, and this situation applies directly to many cases where, although reflecting objects are present, there is also substantial coupling to the outside. In Section 4.2 and 4.3, we test the short-orbit correction and compare it with the frequency smoothing approach and the configuration ensemble approach which are both used to represent the system-specific features in a complicated wave system [24, 41, 111]. After verifying the effects of short orbits, in Section 4.4 we compare the original RCM and the extended RCM to demonstrate the benefits of introducing the short-orbit correction for the goal of uncovering RMT statistics.

4.1 Individual Short Orbits

The first experiment tests whether the analytical form of short-orbit correction [$\underline{\zeta}$, Eq. (2.10)] can correctly predict the effect of individual ray trajectories, as well as the aggregate effect of a small number of ray trajectories, on the impedance. We have discussed the short orbit terms in Sec. 2.2.2, and here we test the term

$$\zeta_{n,m} = \sum_{b(n,m)} \left\{ -\sqrt{D_{b(n,m)}} \exp[-(ik + \kappa)L_{b(n,m)} - ikL_{port(n,m)} - i\beta_{b(n,m)}\pi] \right\}, \quad (4.1)$$

where the amplitude is determined by the geometrical factor $D_{b(n,m)}$ of the trajectory $b(n, m)$, and the phase is determined by the wave number k , the effective attenuation

parameter κ , the length of the trajectory $L_{b(n,m)}$, the port-dependent constant length $L_{port(n,m)}$, and the number of bounces of the trajectory $\beta_{b(n,m)}$. In this experiment, the perturbers are removed from the cavity, and thus the survival probability of the trajectory $p_{b(n,m)}$ in Eq. (2.10) is always $p_{b(n,m)} = 1$.

In order to isolate individual trajectories, I employ microwave absorbers to cover some of the cavity walls, and the experiment systematically includes short orbits involving bounces from exposed walls of the 1/4-bowtie cavity (see insets of Fig. 4.1 for examples, where the thick black lines denote the walls covered by the microwave absorbers). In some combinations of exposed walls, there are an infinite number of trajectories existing in the cavity. Therefore, I employ a cutoff of the sum in Eq. (4.1) by setting a threshold of the maximum length L_M of the computed orbits, and the term is now denoted as $\zeta_{n,m}^{(L_M)}$. By knowing the geometry of the exposed walls and the port locations, the quantities $D_{b(n,m)}$, $L_{b(n,m)}$, and $\beta_{b(n,m)}$ in $\zeta_{n,m}^{(L_M)}$ can be analytically computed. The numerical algorithm for computing these parameters of the short orbit terms is introduced in Appendix A.2. The effective attenuation parameter κ is related to the loss parameter α and will be discussed in the last paragraph of this section.

In Eq. (4.1), $-ikL_{port(n,m)}$ is a modification of the phase of the short-orbit correction term. In all of the experimental results, we observed phase shifts between the measured data and the numerical results. These shifts are consistently observed in all orbit terms, and the quantity is equivalent to the effect of adding an additional offset length. The offset length for Port 1 is 1.86 cm, and the offset length for Port 2 is 1.97 cm. We think that these lengths are from the deviation between the calibrated

reference plane at the end of the transmission lines and the practical reference plane at the port antennas. Therefore, in Eq. (4.1) we introduce this port-dependent correction term $L_{port(n,m)}$ for orbits from the n^{th} port to the m^{th} port.

For the experimental results, in order to compare with the theoretical expression $\zeta_{n,m}^{(LM)}$, I use the random coupling model to remove the effect of the port mismatch (in other words, the radiation impedance matrix $\underline{\underline{Z_{rad}}}$) from the measured impedance. Following from Eq. (2.8), we define the impedance correction matrix $\underline{\underline{z_{cor}}}$ as

$$\underline{\underline{z_{cor}}} \equiv \underline{\underline{R_{rad}}}^{-1/2} (\underline{\underline{Z_{wall}}} - \underline{\underline{Z_{rad}}}) \underline{\underline{R_{rad}}}^{-1/2}. \quad (4.2)$$

$\underline{\underline{Z_{wall}}}$ is the measured impedance of the microwave cavity with specific walls exposed, where the subscript $wall = B, CD, \text{ or } BC$ stands for one or more of the walls (A, B, C, and D, shown in the insets of Fig. 4.1) exposed. The radiation impedance matrix $\underline{\underline{Z_{rad}}}$ is determined by a separate measurement in which all four side walls are covered by the microwave absorbers [36]. In Eq. 4.2, we remove the radiation impedance $\underline{\underline{Z_{rad}}}$ from the measured impedance $\underline{\underline{Z_{wall}}}$. Note that, for the two-port case, the measured result is a 2×2 matrix with non-zero off-diagonal elements which represent the coupling between the two ports (the direct orbit). However, here we want to examine the effect of this direct orbit in $\underline{\underline{z_{cor}}}$ in the two-port case. Therefore, we only take the diagonal elements of the measured radiation impedance matrix for $\underline{\underline{Z_{rad}}}$ and $\underline{\underline{R_{rad}}}$. After this normalization method, the direct orbit and other bounced orbits of the measured impedance $\underline{\underline{Z_{wall}}}$ remain in the impedance correction matrix $\underline{\underline{z_{cor}}}$.

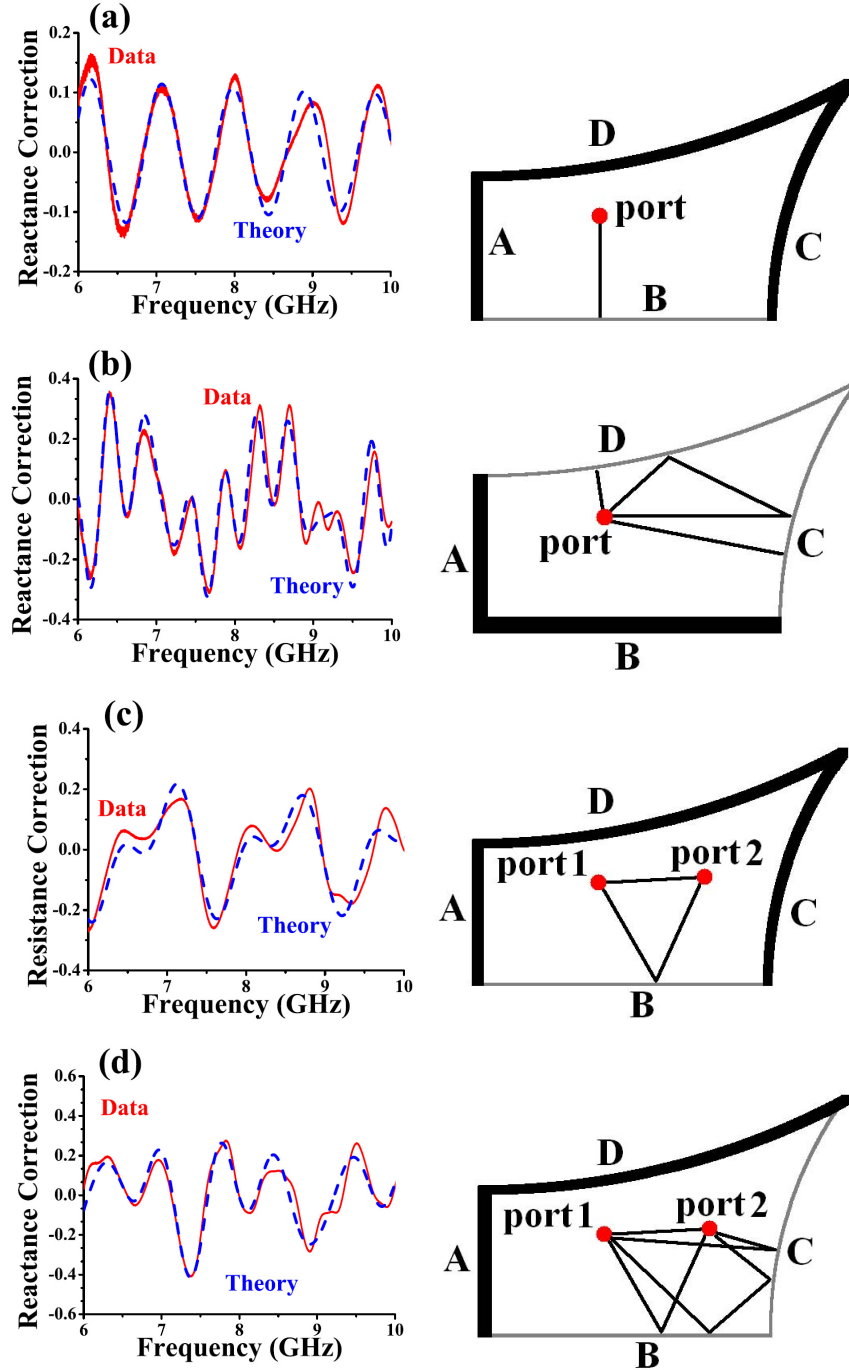


Figure 4.1: Four examples of the comparison between the $z_{cor,n,m}$ elements (Data) and the $\zeta_{n,m}^{(LM)}$ elements (Theory). The insets are the corresponding geometry of the exposed walls. The thick black lines denote microwave absorber material covering the walls.

Figure 4.1 shows four examples of the comparison in frequency domain (6 – 10 GHz) between the impedance correction $z_{cor,n,m}$ from the measured impedance (\underline{Z}_{wall}) and the short-orbit correction term $\zeta_{n,m}^{(L_M)}$ according to Eq. (4.1) with the maximum length L_M . The measured results (Data) are represented by red and solid curves, and the theoretical results are represented by blue and dashed curves. The resistance correction is the real part of the impedance correction ($\text{Re}[z_{cor,n,m}]$ or $\text{Re}[\zeta_{n,m}^{(L_M)}]$); the reactance correction is the imaginary part of the impedance correction ($\text{Im}[z_{cor,n,m}]$ or $\text{Im}[\zeta_{n,m}^{(L_M)}]$). We have examined other combinations of exposed walls and choose some representative cases to show here. Figures 4.1(a) and 4.1(b) are for the cases of one-port experiments with (a) one wall exposed (wall B) and (b) two walls exposed (walls C and D), and Figures 4.1(c) and 4.1(d) are for cases of two-port experiments with (c) one wall exposed (wall B) and (d) two walls exposed (walls B and C). The geometry is illustrated in the insets, where the red dots are positions of the ports, and the thicker black walls represent the walls covered by the microwave absorbers. I also illustrate some short orbits as black lines in the insets.

The measured data generally follow the theoretical predictions quite well, thus the comparison verifies that the short-orbit correction offers a quantitative prediction of short-orbit features of the impedance \underline{Z}_{wall} . In Fig. 4.1(a), we examine the resistance correction for the waves entering and returning from the cavity through the single port (the $z_{cor,11}$ element), and the short-orbit correction includes only one orbit from the exposed wall B. This explains the simple oscillation in the frequency domain. In Fig. 4.1(b), still a one-port case, we examine the reactance correction for Z_{11} due to orbits from the exposed walls C and D. There are an infinite number

of orbits in this case, but for $\zeta_{11}^{(L_M)}$ we only include eight of them with orbit lengths shorter than $L_M = 80$ cm. The good agreement shows longer orbits are less important. In Figs. 4.1(c) and 4.1(d), the two-port cases, we examine the resistance correction and the reactance correction between the two ports (the $z_{cor,12}$ element). For the case in Fig. 4.1(c), there are only two orbits including the direct orbits and a one-bounce orbit. For the case in Fig. 4.1(d), there are only four orbits. The small deviations between the theoretical results and the measured results can be further analyzed if we plot the results in the length domain. The major error source is the imperfections of the microwave absorbers. The details of this length-domain analysis are given in Appendix C.

In the end of this section, I go back to discuss how to measure the effective attenuation parameter κ used in Eq. (4.1). κ represents the the propagation attenuation of orbits and is a frequency-dependent attenuation parameter $\kappa(f)$. We compute κ by utilizing the previously measured frequency-dependent loss parameter α of the 1/4-bowtie cavity [3]. Here α is the loss parameter introduced in Chapter 2.1.1 as the ratio of the 3-dB bandwidth of the closed-cavity resonance modes to the mean spacing between cavity modes, $\alpha \equiv k^2/(\Delta k_m^2 Q) \simeq k^2 A/(4\pi Q)$, where A is the area of the cavity ($A = 0.115 \text{ m}^2$), k is the wave number, and Q is the quality factor of the cavity. The mean spacing between modes varies from 21 MHz at 6 GHz to 6.9 MHz at 18 GHz.

Figure 4.2 shows the loss parameter α and the effective attenuation parameter κ versus frequency of an empty 1/4-bowtie cavity. We obtain the loss parameter α from the measured impedance data in an empty 1/4-bowtie cavity according to

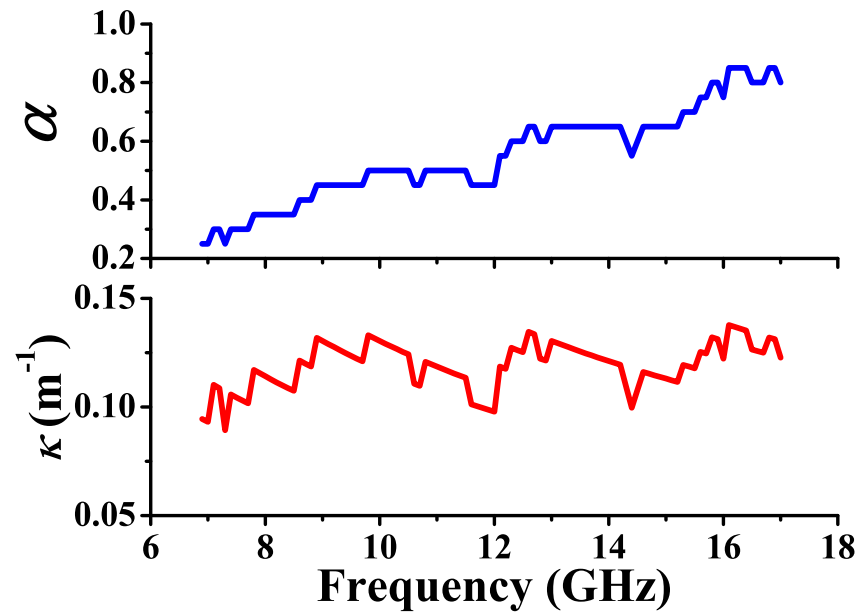


Figure 4.2: The loss parameter α and the attenuation parameter κ versus frequency of the empty 1/4-bowtie cavity. The loss parameter is determined by the best-fit of the statistics of the measured impedance data and the RMT prediction, and the attenuation parameter is calculated from the loss parameter.

the procedures presented in previous work [36, 60]. In this procedure the frequency-dependent loss parameter $\alpha(f)$ is determined by the best-fit of the statistics of the measured data and the RMT prediction. More particularly, we use RMT to generate a series of numerical data of the perfectly-coupled impedance matrix [\underline{z}_{rmt} , Eq. (2.2)] with varied loss parameters in a step of 0.05. For the experimental data, we select a proper frequency range (e.g., 1.8 GHz) and compute the probability density function (PDF) of the “perfectly-coupled” normalized impedance \underline{z}_n [Eq. (2.15)] in the range. Then we compare the PDF of the experimental data to different PDFs of numerical data generated according to RMT, using α as a fitting parameter. We choose the α value of the best-fit PDF of the numerical data as the loss parameter at the center frequency f of the frequency range. Once $\alpha(f)$ is known, the frequency-dependent attenuation parameter $\kappa(f)$ can be calculated because the dominant attenuation comes from losses in the top and bottom plates of the 1/4-bowtie cavity, and it is well modeled by assuming that the waves suffer a spatially uniform propagation loss $\kappa = k/(2Q) = 2\pi\alpha/(kA)$.

4.2 Short-Orbit Correction and Frequency Smoothing

Considering the short-orbit correction, Eq. (4.1), each orbit term creates a periodic oscillation in the frequency domain, and the period is related to the orbit length $L_{b(n,m)}$. When we set a maximum length L_M to cut off the sum in Eq. (4.1), it is equivalent to applying a low-pass filter or a smoothing method on the frequency dependent quantity $Z(f)$. In this section, we first demonstrate the

measured results of the impedance of a empty 1/4-bowtie cavity, where all orbits present. Then we introduce a smoothing method for the frequency-domain data. Finally the comparison will shows that the short-orbit-corrected impedance agrees with the frequency-smoothed impedance (the frequency ensemble).

Firstly, we measure the impedance matrix of an empty 1/4-bowtie cavity without microwave absorbers or perturbers. Therefore, all possible orbits between ports are present in this single realization. Figure 4.3 shows (a) the real and (b) the imaginary parts of the first diagonal element of the impedance in a two-port cavity, corresponding to $\text{Re}[Z_{11}]$ and $\text{Im}[Z_{11}]$. Figures 4.3(c) and 4.3(d) are for the off-diagonal element of the impedance, $\text{Re}[Z_{12}]$ and $\text{Im}[Z_{12}]$. The measured data are shown in red curves. The radiation impedance data are shown in black curves in the cases of the diagonal elements. The radiation impedance \underline{Z}_{rad} is measured with all side walls covered by the microwave absorbers, and it traces through the center of the fluctuating impedance data of the empty cavity and represents the nonuniversal aspects of the coupling antennas [36, 57, 58]. Note that I treat \underline{Z}_{rad} as a diagonal matrix, so the off-diagonal term is zero and not shown in Figs. 4.3(c) and 4.3(d). The blue curves represent the short-orbit-corrected radiation impedance matrix \underline{Z}_{soc} [Eq. (2.8)], which combines the radiation impedance and the short-orbit correction up to $L_M = 200$ cm.

$$\underline{Z}_{soc}^{(L_M)} = \underline{Z}_{rad} + \underline{R}_{rad}^{1/2} \left(\underline{\zeta}^{(L_M)} \right) \underline{R}_{rad}^{1/2}. \quad (4.3)$$

This gives a total of 584 orbit terms for $Z_{soc,11}^{(L_M)}$ and 1088 orbit terms for $Z_{soc,12}^{(L_M)}$.

The theoretical impedance $\underline{Z}_{soc}^{(L_M)}$ tracks the main features of the single-realization

measured impedance although there are many sharp deviations between the two sets of curves. These fluctuations are expected because of the infinite number of trajectories ($L_{b(n,m)} > 200$ cm) not included in the short-orbit correction.

When computing the sum of short-orbit correction terms in a low loss system like the empty metal cavity, a problem associated with the finite number of terms ($L_{b(n,m)} \leq L_M$) occurs in the sum. In the theory, to perfectly reproduce the measured data in the empty cavity requires an infinite number of orbit terms. Therefore, in some frequency regions where the experimental impedance changes rapidly, the finite sum for the theoretical resistance $\text{Re}[\underline{Z}_{soc}^{(L_M)}]$ will show values less than zero, which are not physical for a passive system. For example, see the blue dashed curve in Fig. 4.3(a) between 6.3 and 6.4 GHz. This problem is similar to the Gibbs phenomenon in which the sum of a finite number of terms of the Fourier series has large overshoots near a jump discontinuity.

In Fig. 4.3 we claim that the theoretical impedance $\underline{Z}_{soc}^{(L_M)}$ tracks the main features of the single-realization measured impedance \underline{Z} . To further verify this, we introduce a frequency-smoothing method and apply it to both $\underline{Z}_{soc}^{(L_M)}$ and \underline{Z} . In particular, if $Z(f)$ denotes a frequency dependent quantity, then we take its frequency smoothed counterpart to be the convolution of $Z(f)$ with a Gaussian function,

$$\overline{Z(f)} = \int Z(f')g(f - f')df', \quad (4.4)$$

where the Gaussian function

$$g(f) = \frac{1}{\sqrt{2\pi}\sigma_f} \exp\left(\frac{-f^2}{2\sigma_f^2}\right), \quad (4.5)$$

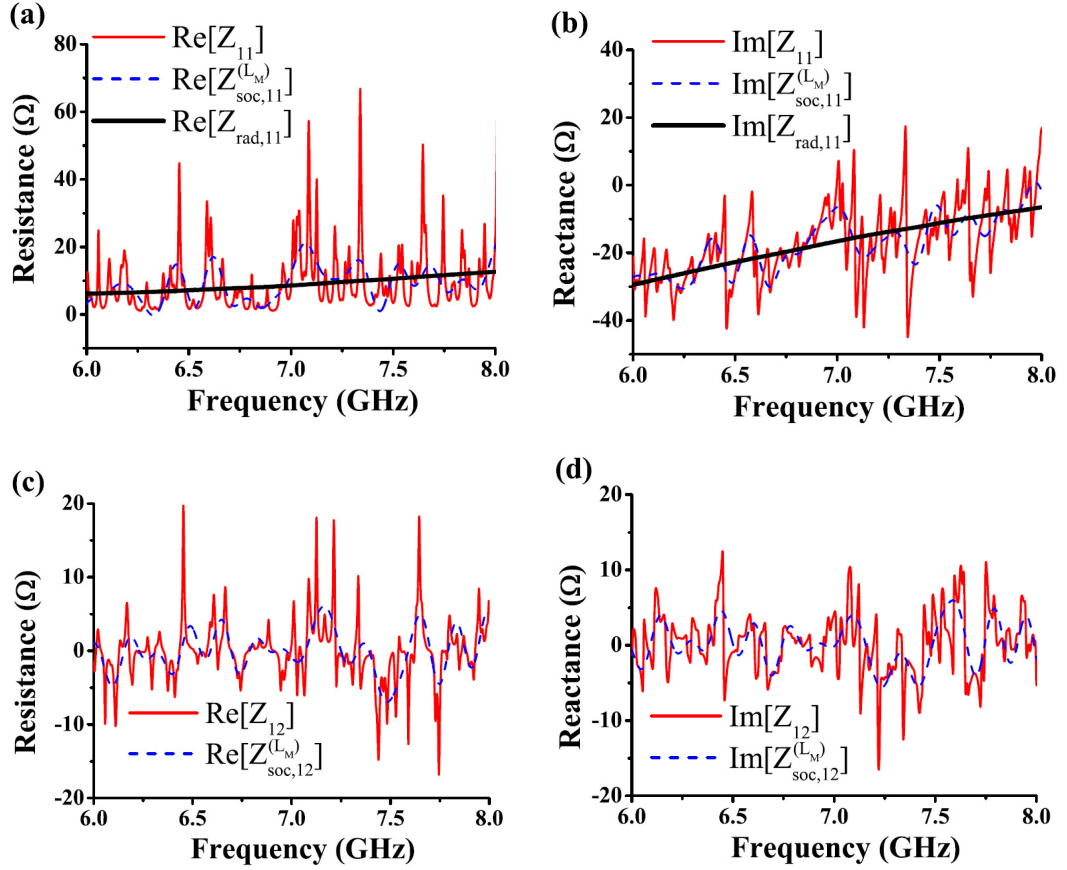


Figure 4.3: The impedance of the empty 1/4-bowtie cavity with two ports. Shown are (a) the real part of Z_{11} , (b) the imaginary part of Z_{11} , (c) the real part of Z_{12} , and (d) the imaginary part of Z_{12} with the measured impedance $Z_{n,m}$ (red thinner), the short-orbit-corrected radiation impedance $Z_{soc,n,m}^{(LM)}$ (blue dashed), as well as the radiation impedance $Z_{rad,n,m}$ (black).

and σ_f is the standard deviation of the Gaussian smoothing function. Applying the operation (4.4) to our short-orbit correction formulas, Eq. (4.1), with $k = 2\pi f/c$, we see that the summations acquire an additional multiplicative factor,

$$\exp\left[-\frac{1}{2}(L_{b(n,m)} + L_{port(n,m)})^2(2\pi\sigma_f/c)^2\right]. \quad (4.6)$$

Thus, as the orbit length $L_{b(n,m)}$ increases (i.e., longer orbits are included), the factor [Eq. (4.6)] eventually becomes small, thus providing a natural cutoff to the summations in Eq. (4.1).

We compare the frequency-smoothed impedance matrices $\underline{\underline{Z}}_{soc}^{(LM)}$ and $\underline{\underline{Z}}$ in the one-port experiment and the two-port experiment. Both are single-realization measurement in the empty 1/4-bowtie cavity, and the results are shown in Fig. 4.4. The frequency smoothing [Eqs. (4.4) and (4.5)] suppresses the impedance fluctuations due to long orbits and reveals the system-specific features associated with short orbits. Figure 4.4 shows the radiation impedance (black thick), the smoothed measured impedance $\underline{\underline{Z}}$ (red solid) and the smoothed theoretical impedance $\underline{\underline{Z}}_{soc}^{(LM)}$ (blue dashed). The smoothing is made by a Gaussian smoothing function with the standard deviation $\sigma_f = 240$ MHz [Eq. (4.5)]. Gaussian frequency smoothing inserts an effective low-pass Gaussian filter on the orbit length, and thus, the components of impedances ($\underline{\underline{Z}}$ and $\underline{\underline{Z}}_{soc}^{(LM)}$) in the length domain are limited by the cutoff length $c/\sigma_f = 125$ cm. Figure 4.4 shows that the smoothed short-orbit feature matches the smoothed experimental data very well. Therefore, the short-orbit correction correctly captures the effects of ray trajectories up to the cutoff length (125 cm).

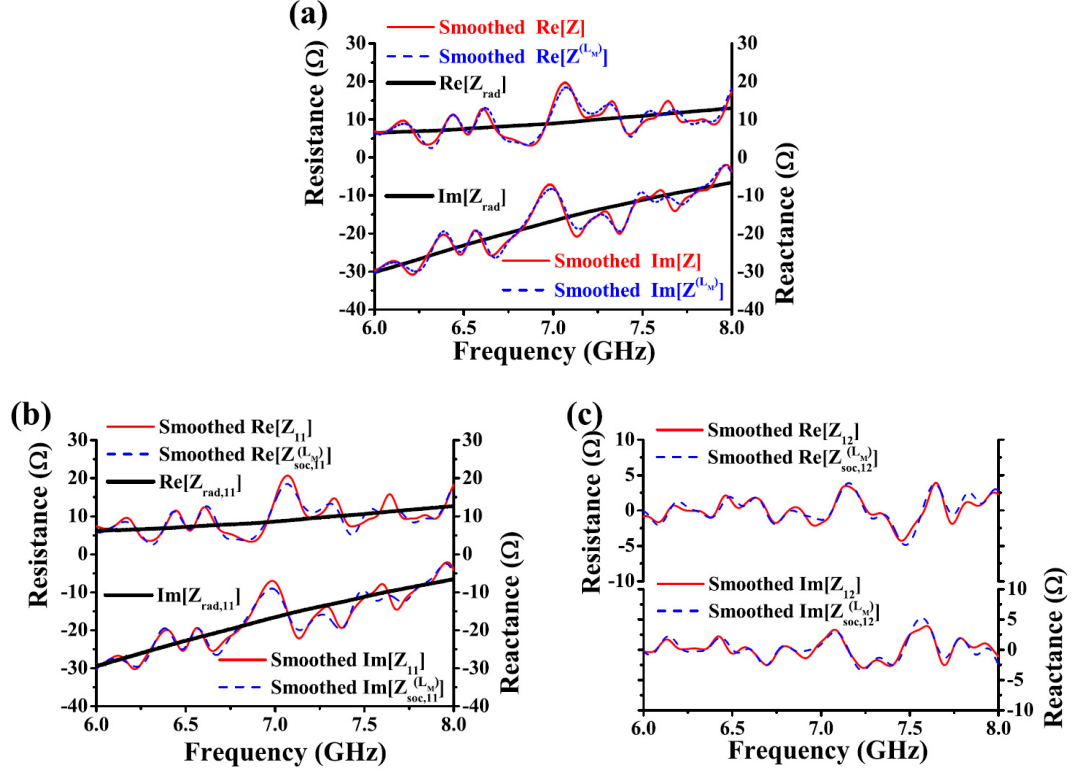


Figure 4.4: The smoothed impedance of the 1/4-bowtie cavity versus frequency of (a) Z_{11} in the one-port experiment, (b) Z_{11} in the two-port experiment, and (c) Z_{12} in the two-port experiment. Shown are the real (three upper curves) and the imaginary parts (three lower curves) of the smoothed impedance for the theory $Z_{\text{soc},n,m}^{(L_M)}$ (blue dashed curves) and the experiment $Z_{n,m}$ (red solid curves), as well as the measured (un-smoothed) radiation impedance of the port ($Z_{\text{rad},n,m}$, black thick).

4.3 Short-Orbit Correction and Configuration Ensemble

We have tested that the short-orbit-corrected radiation impedance $\underline{\underline{Z_{soc}^{(LM)}}}$ and the frequency smoothed impedance (frequency ensemble) can both represent the system-specific features of a complicated wave scattering system. In this section we will compare the short-orbit correction with another major method to reveal the system-specific features, the configuration averaging.

Many efforts to determine universal RMT statistics in experimental systems are based on a configuration averaging approach that creates an ensemble average from realizations with varied configurations. In principle, one can recover the nonuniversal (system-specific) properties of the system [24, 111] via the configuration averaging approach, which is motivated by the “Poisson kernel” theory of Mello, Pereyra, and Seligman [63]. Specifically, ensemble averages of the measured cavity data are used to remove the system-specific features in each single realization. Note that in the past, the configuration averaging approach was explicitly assumed to only remove the effects of the nonuniversal coupling; however, it was later generalized to include the nonuniversal contributions of short orbits [75].

We compare the short-orbit-corrected radiation impedance $\underline{\underline{Z_{soc}^{(LM)}}}$ and the ensemble-averaged impedance $\underline{\underline{Z_{avg}}}$ (configuration ensemble) in a one-port experiment and a two-port experiment. In order to collect a realization ensemble, two metal perturbers are used in the 1/4-bowtie cavity. In the one-port experiment, two irregular-shaped pieces of metal are added as perturbers; in the two-port experiment, two cylindrical pieces of metal are added as perturbers. Both are shown

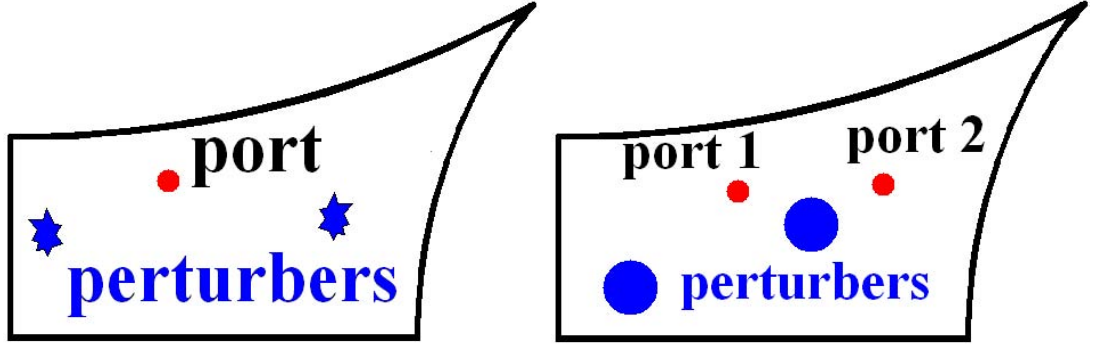


Figure 4.5: Left: the one-port experiment system with two irregular-shaped perturbers. Right: the two-port experiment system with two cylindrical perturbers.

in the Fig. 4.5, where the dots represent the ports, and the blue objects represent the perturbers. In each experiment, the locations of the two perturbers inside the cavity are systematically changed and accurately recorded to produce a set of 100 realizations for the ensemble [36, 40, 41, 60]. The impedance matrix \underline{Z} is measured from 6 to 18 GHz, covering roughly 1100 modes of the closed cavity. Typically, the shifts of resonances between two realizations are about one mean level spacing. Then we compute the average over the 100 realizations, $\underline{Z}_{avg} = \langle \underline{Z} \rangle$. After the ensemble averaging, longer orbits have higher probability of being blocked by the two perturbers in the 100 realizations; therefore, the main nonuniversal contributions are due to shorter orbits. We compare the ensemble-averaged impedance \underline{Z}_{avg} and the short-orbit-corrected radiation impedance $\underline{Z}_{soc}^{(L_M)}$ which is calculated from Eqs. (2.8) and (2.10) with the maximum orbit length $L_M = 200$ cm.

In the configuration ensemble, contrary to the previous cases of an empty cavity without perturbers, we need to introduce a survival probability $p_{b(n,m)}$ for each orbit term in Eq. (2.10).

$$\zeta_{n,m}^{(L_M)} = \sum_{b(n,m)}^{L_{b(n,m)} \leq L_M} \left\{ -p_{b(n,m)} \sqrt{D_{b(n,m)}} \exp[-(ik + \kappa)L_{b(n,m)} - ikL_{port(n,m)} - i\beta_{b(n,m)}\pi] \right\}. \quad (4.7)$$

Notice that the two perturbers can block orbits and influence their presence in the ensemble realizations. Thus, we multiply each term in the sum by a weight $p_{b(n,m)}$ equal to the fraction of perturbation configurations in which the orbit is not intercepted by the perturbers. The values of $p_{b(n,m)}$ are between 0 and 1, and a longer ray trajectory generally has a higher chance of being blocked by perturbers, and thus it has smaller $p_{b(n,m)}$. Note that by recording the positions of perturbers in all realizations, we are able to calculate the short-orbit correction individually for each realization, similar to the procedures in the empty cavity case [Eq. (4.1)]. Here we introduce $p_{b(n,m)}$ as a more general description for the case in which only the probabilities of survival of particular short orbits are known. In addition, we ignore the effect of newly created orbits by the perturbers in each specific realization because they are averaged out in the ensemble. Note that the attenuation parameter κ in the short-orbit correction terms [Eq. (4.7)] is recalculated by using the measured PDFs of impedance in the ensemble case, using procedures similar to those for the case of the empty cavity [36, 60]. Due to the presence of two perturbers in the cavity, the attenuation parameter and loss parameter are slightly larger (~ 0.1 for α) than in the empty cavity case (Fig. 4.2).

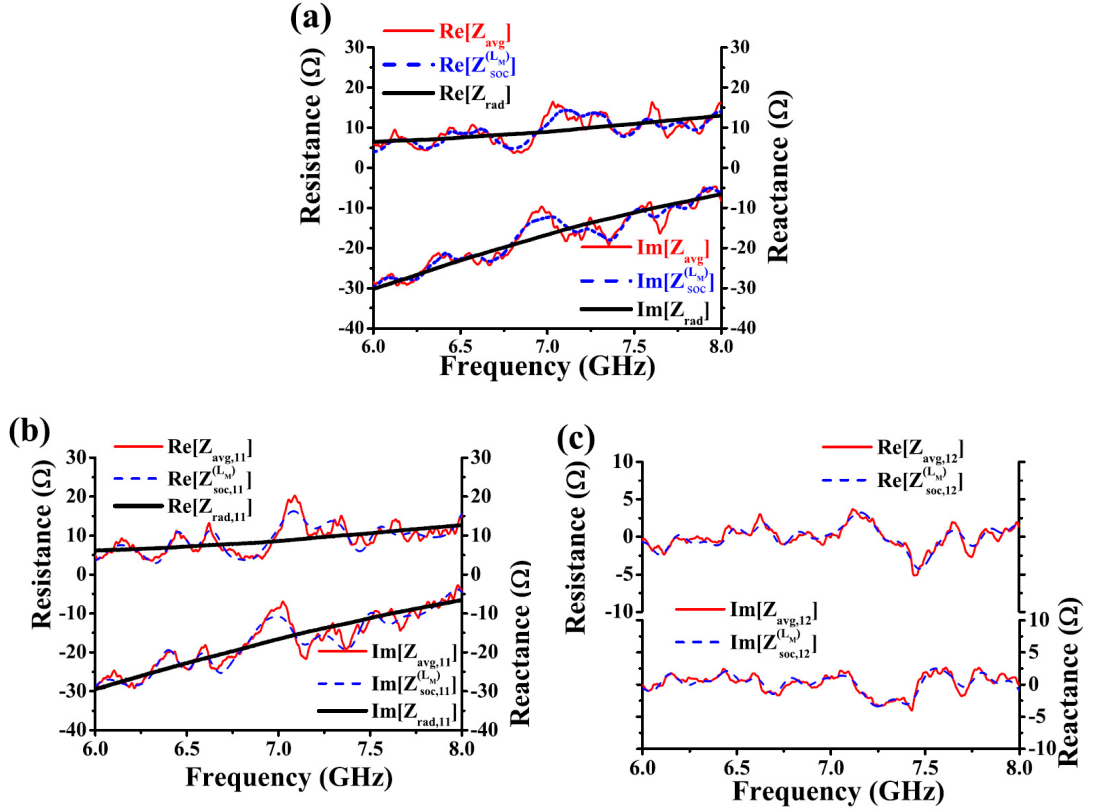


Figure 4.6: The averaged impedance versus frequency of (a) Z_{11} in the one-port experiment, (b) Z_{11} in the two-port experiment, and (c) Z_{12} in the two-port experiment. Shown are the real (three upper curves) and the imaginary parts (three lower curves) of the ensemble-averaged impedance $Z_{\text{avg},n,m}$ (red solid curves), comparing with the theory $Z_{\text{soc},n,m}^{(L_M)}$ (blue dashed curves) and the radiation impedance of the port ($Z_{\text{rad},n,m}$, black thick).

The result of comparisons between the ensemble-averaged impedance $\underline{\underline{Z_{avg}}}$ and the short-orbit-corrected radiation impedance $\underline{\underline{Z_{soc}^{(L_M)}}}$ are shown in Fig. 4.6. Figure 4.6 (a) shows the comparison of the impedance in the one-port experiment, Fig. 4.6 (b) shows the first diagonal component of the impedance, and Fig. 4.6 (c) shows the comparison of the off-diagonal component in the two-port experiment. The measured data (red solid) follow the trend of the radiation impedance (black thick), and the theory (blue dashed) reproduces most of the fluctuations in the data by including only a modest number of short-orbit correction terms (584 orbits for $Z_{soc,11}^{(L_M)}$ and 1088 orbits for $Z_{soc,12}^{(L_M)}$ with $L_M = 200$ cm). Note that no frequency smoothing (or wavelength averaging) is used here. The good agreement between the measured data and the theoretical prediction verifies that the short-orbit correction theory predicts the nonuniversal features embodied in the ensemble-averaged impedance well.

The deviations between the $\underline{\underline{Z_{avg}}}$ curves and the $\underline{\underline{Z_{soc}^{(L_M)}}}$ curves in Fig. 4.6 may come from several effects. The first is the remaining fluctuations in the $\underline{\underline{Z_{avg}}}$ due to the finite number of realizations. We estimate this to be on the order of $\sigma_{Z_{avg}} \simeq \sigma_Z / \sqrt{100} \sim 1\Omega$, where $\sigma_{Z_{avg}}$ is the standard deviation of ensemble-averaged impedance $\underline{\underline{Z_{avg}}}$ of 100 realizations, and σ_Z is the standard deviation of the measured impedance $\underline{\underline{Z}}$ of a single realization. This accounts for the remaining sharp features in $\underline{\underline{Z_{avg}}}$. Another source of errors is that we ignore the effect of newly created orbits by the perturbers. Even though these new orbit terms are divided by 100 (the number of realizations), the remaining effects create small deviations.

4.4 Benefits of the Short-Orbit Correction

In previous sections we have verified that the short-orbit correction can represent the system-specific features of the measured data. Next, we will demonstrate that including the short-orbit correction in the random coupling model (RCM) can improve the ability to reveal underlying universal statistical properties. Recall the RCM normalization [Eq. (2.15)] introduced in Chapter 2, in this section, we will compare the statistical results of the three different types of the RCM normalization:

$$\underline{\underline{z_n^{(0)}}} = \underline{\underline{R_{rad}}}^{-1/2} \left(\underline{\underline{Z}} - i \underline{\underline{X_{rad}}} \right) \underline{\underline{R_{rad}}}^{-1/2}, \quad (4.8)$$

$$\underline{\underline{z_n^{(1)}}} = \underline{\underline{R_{avg}}}^{-1/2} \left(\underline{\underline{Z}} - i \underline{\underline{X_{avg}}} \right) \underline{\underline{R_{avg}}}^{-1/2}, \quad (4.9)$$

$$\underline{\underline{z_n^{(L_M)}}} = \underline{\underline{R_{soc}^{(L_M)}}}^{-1/2} \left(\underline{\underline{Z}} - i \underline{\underline{X_{soc}^{(L_M)}}} \right) \underline{\underline{R_{soc}^{(L_M)}}}^{-1/2}. \quad (4.10)$$

$\underline{\underline{z_n^{(0)}}}$ is the normalized impedance based on the original RCM [Eq. (2.1)] which only takes account of the radiation impedance $\underline{\underline{Z_{rad}}}$ as the system-specific feature. $\underline{\underline{z_n^{(1)}}}$ is the normalized impedance of the extended RCM [Eq. (2.15)] which includes the radiation impedance and the effect of short orbits by directly utilizing the ensemble-averaged impedance $\underline{\underline{Z_{avg}}}$. $\underline{\underline{z_n^{(L_M)}}}$ is the short-orbit correction version of $\underline{\underline{z_n^{(1)}}}$, and we will tune the maximum orbit length L_M to examine the influence of short orbits in the RCM normalization.

4.4.1 Statistics of the Impedance Matrix

Hemmady *et al.* have compared the statistical predictions of random matrix theory (RMT) with the statistics of the normalized impedance matrix based on the

original RCM ($\underline{z_n^{(0)}}$) [36, 60, 88]. Their results show good agreement between the statistics of $\underline{z_n^{(0)}}$ and $\underline{z_{rmt}}$ when the data of $\underline{z_n^{(0)}}$ are collected from a large enough frequency window [3]. Here we demonstrate the benefit of using the short-orbit correction that the statistics of the revealed universal properties ($\underline{z_n^{(L_M)}}$) by the extended RCM have better agreement with the prediction of RMT ($\underline{z_{rmt}}$) than the original version ($\underline{z_n^{(0)}}$) when the bandwidth of the frequency window is small. A small frequency window means $f_{bw} < c/\min\{L_o\}$, where f_{bw} is the frequency bandwidth, and $\min\{L_o\}$ is the shortest orbit length. For example, in the one-port experiment in the 1/4-bowtie cavity, the shortest orbit is the one launching from the port, bouncing on wall D, and returning back ($L_o = 15$ cm and $c/L_o = 2$ GHz).

We compare the probability distributions of the eigenvalues of the normalized impedance matrices ($z_{n,eig}^{(0)}$ and $z_{n,eig}^{(L_M)}$), and the PDFs that are generated from numerical RMT [36, 60, 88] in Fig. 4.7. The experimental data are measured from the 100 realizations of the 1/4-bowtie cavity and in a frequency range of 200 MHz. Then we compute the eigenvalues of the 2×2 normalized impedance matrix for each realization and each frequency. For the short-orbit correction case ($\underline{z_n^{(L_M)}}$, the blue curves with squares), we use $L_M = 200$ cm. Here we show two examples for frequency ranges 6.8 – 7.0 GHz in Figs. 4.7(a) (the real part) and 4.7(b) (the imaginary part); and 11.0 – 11.2 GHz in Figs. 4.7(c) (the real part) and 4.7(d) (the imaginary part). For the numerical RMT data ($\underline{z_{rmt}}$ the black curves), we use the Monte Carlo method to generate $\underline{z_{rmt}}$ and then compute the eigenvalues, and the loss parameters ($\alpha = 0.3$ for 6.8 – 7.0 GHz and $\alpha = 0.4$ for 11.0 – 11.2 GHz) were determined by the best-matched distribution with a much wider frequency range (2

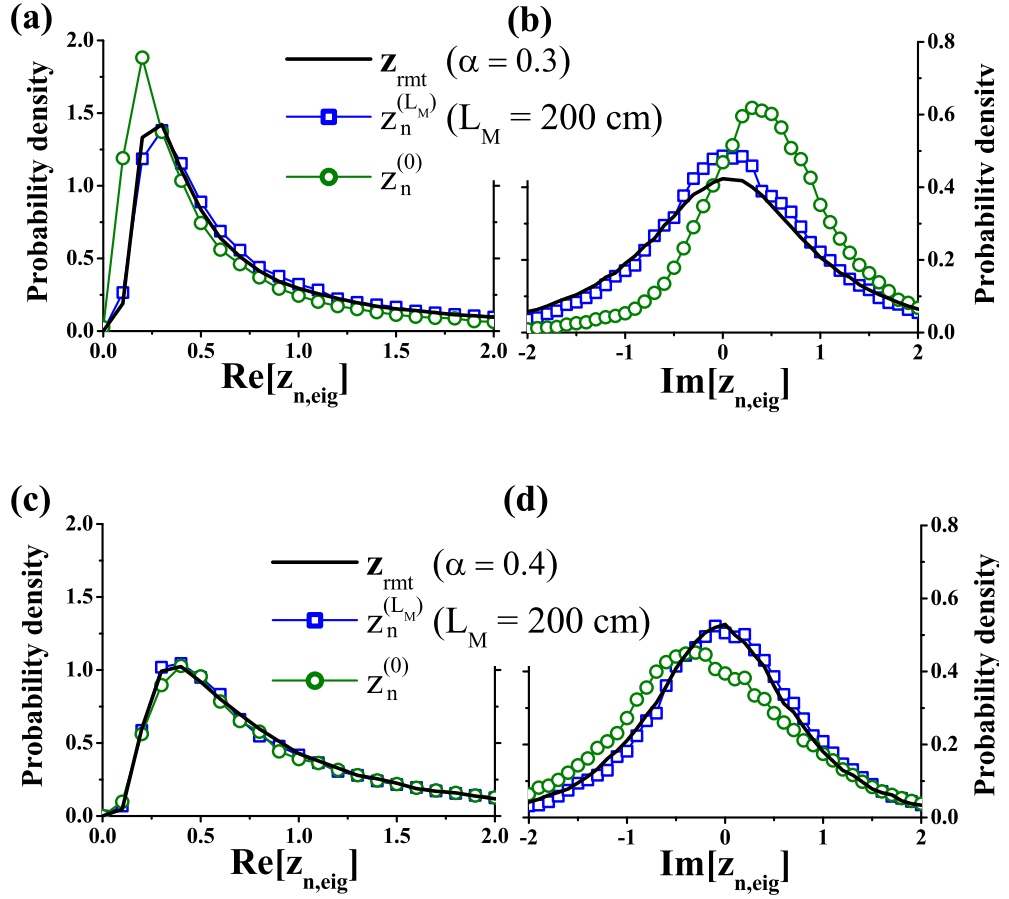


Figure 4.7: The probability distributions of (a) the real part and (b) the imaginary part of the normalized impedance eigenvalues in the frequency range 6.8 – 7.0 GHz, and (c) the real part and (d) the imaginary part of the normalized impedance in the frequency range 11.0 – 11.2 GHz.

GHz). As seen in Fig. 4.7 the distribution of the eigenvalues of the normalized impedance has much better agreement with the prediction of RMT when we consider the short-orbit correction up to the orbit length of 200 cm.

We have also compared the statistics of $\underline{z_n^{(L_M)}}$ ($L_M = 200$ cm) and $\underline{z_n^{(1)}}$ which directly use $\underline{Z_{avg}}$ in the RCM normalization [Eq. (4.9)]. In small frequency windows, the statistics of $\underline{z_n^{(L_M)}}$ and $\underline{z_n^{(1)}}$ are similar, and they both agree better with the theoretical prediction $\underline{z_{rmt}}$ than the statistics of $\underline{z_n^{(0)}}$. However, when we enlarge the frequency window, the PDFs of the $\underline{z_n^{(0)}}$ get closer to the other two. This is because the fluctuations in the impedance due to a short orbit can be compensated in a wide enough frequency window (i.e., the required window is 2 GHz for the shortest orbit with $L_{b(1,1)} = 15$ cm). Therefore, we take a 2 GHz frequency window to obtain a universal distribution that is independent of which normalization methods we use [Eqs. (4.8), (4.9) or (4.10)], and we also determine the loss parameter from this universal distribution [3, 88, 90].

Furthermore, the deviations shown in Fig. 4.7 match the difference between $\underline{Z_{avg}}$ and $\underline{Z_{rad}}$ shown in Fig. 4.6. For example, in the frequency range 6.8 – 7.0 GHz the ensemble-averaged impedance $Z_{avg,11}$ is smaller than the radiation impedance $Z_{rad,11}$ in the real part and larger in the imaginary part. In Figs. 4.7(a) and 4.7(b) we can see the same bias of the distribution of the normalized impedance $\underline{z_n^{(0)}}$ that is normalized with the radiation impedance only. Therefore, with the short-orbit correction, we can better explain the deviations between the statistics of the measured data and the universal properties predicted by RMT.

4.4.2 Statistics of the Scattering Matrix

We now test the benefits of the short-orbit correction in uncovering universal statistics of the scattering matrix (\underline{s}_{rmt}) predicted by RMT. We find that including short orbits in the RCM normalization improves our determination of the RMT statistical properties of the scattering matrix \underline{S} , given the same number of samples from the ensemble realizations and the frequency window. In other words, we show that the need to resort to a wide frequency window over large numbers of modes is significantly reduced after including the short-orbit correction in the impedance normalization. We show the results of the one-port experiment and the two-port experiment in the 1/4-bowtie cavity with 100 realizations varied by the two perturbations.

Random matrix theory predicts that the eigenvalue of the scattering matrix $\underline{s}_{rmt} = (\underline{z}_{rmt} - \underline{1})(\underline{z}_{rmt} + \underline{1})^{-1}$ should have an independent uniformly-distributed phase. In other words, the phases φ_s of the eigenvalues of \underline{s}_{rmt} should have a uniform distribution from 0 to 2π independent of loss, frequency, and mean level spacing [63, 111]. Hemmady *et al.* [60, 88] have experimentally verified this prediction in the 1/4-bowtie cavity by the original RCM. Here we examine the statistics of the phase φ_s of the eigenvalues of the normalized scattering matrix

$$\underline{s}_n^{(L_M)} = \left(\underline{z}_n^{(L_M)} - \underline{1} \right) \left(\underline{z}_n^{(L_M)} + \underline{1} \right)^{-1} \quad (4.11)$$

in varied frequency bandwidths and L_M , in order to analyze the influence of the short-orbit correction.

Firstly, we show an example in Fig. 4.8 to illustrate the benefits of using

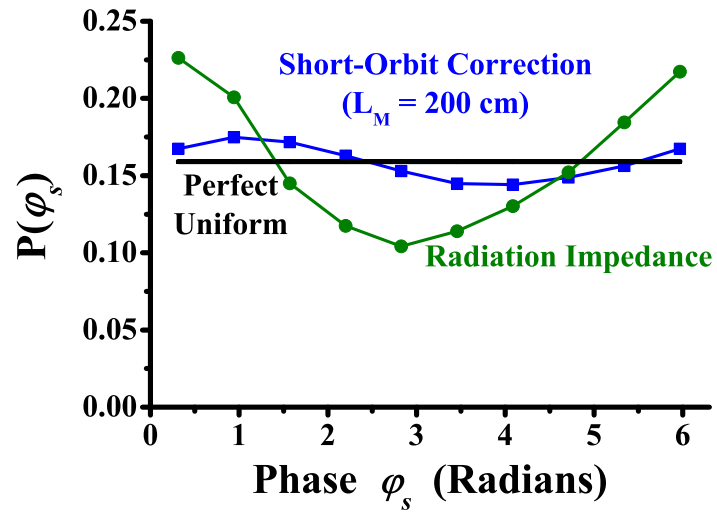


Figure 4.8: An example of the probability distributions $P(\varphi_s)$ of the phase φ_s of eigenvalues of the normalized scattering matrices, taken over from the 11.0 – 11.5 GHz frequency window.

short-orbit-corrected data to determine the statistical properties of the scattering matrix. We do the RCM normalization with (i) the radiation impedance matrix (\underline{Z}_{rad}) only [Eq. (4.8)] and (ii) with the short-orbit-corrected radiation impedance matrix ($\underline{Z}_{soc}^{(L_M)}$) [Eq. (4.10)] from a two-port 1/4-bowtie cavity. The data of the normalized scattering matrix are formed by taking the measured impedance from each of the 100 realizations and in a 500 MHz frequency range (11.0 – 11.5 GHz). The blue (squares) curve is from data normalized with $\underline{Z}_{soc}^{(L_M)}$ ($L_M = 200$ cm), the green (circles) curve is from data normalized with the radiation impedance only, and the black line shows the uniform distribution for comparison. In this frequency range, it is clear that the distribution normalized with the short-orbit correction is significantly closer to a uniform distribution than the one normalized with the radiation impedance only.

In order to do a thorough analysis of the benefits of the short-orbit correction, we define a parameter, the average root-mean-square (RMS) error to evaluate how uniform the resulting phase distributions $P(\varphi_s)$ are. Here the RMS error is defined as

$$RMS\ error \equiv \frac{1}{\langle n_i \rangle} \sqrt{\frac{1}{10} \sum_{i=1}^{10} (n_i - \langle n_i \rangle)^2}, \quad (4.12)$$

where n_i is the number of elements in the i th bin in the 10-bin histogram of $P(\varphi_s)$, and $\langle n_i \rangle$ is the mean of n_i . The RMS error is the standard deviation of the 10-bin histogram normalized by its mean. Therefore, when a distribution is closer to a uniform distribution, its RMS error is smaller. We compute the RMS errors of the phase distributions $P(\varphi_s)$ from the normalized scattering matrices with different

RCM normalization methods and varied frequency window sizes, then we compute the average RMS error of each frequency window size, given the data in the spectral range from 6 to 18 GHz in 100 realizations. Figure 4.9 shows the average RMS error versus the frequency window sizes of (a) the one-port case and (b) the two-port case.

In Fig. 4.9(a) the one-port case, the normalized scattering parameter are calculated from impedance normalized with the radiation impedance only (green circles) and with additional short orbits according to the maximum orbit length from $L_M = 50$ cm (red triangles) up to $L_M = 200$ cm (blue squares), versus frequency window sizes from 0.1 to 4.0 GHz. The results indicate that the distributions of the measured data are systematically more uniform as more orbits are taken into account in the impedance normalization [Eq. (4.10)] for a given window size. The improvement is dramatic after including just a few short orbits ($L_M = 50$ cm, 7 trajectories) and saturates beyond $L_M = 100$ cm (36 trajectories). The periodic wiggles represent the effects of the strongest remaining orbit not taken into account in the theory. Note that the radiation impedance curve (green circles) has local minimums near 1.8 GHz and 3.6 GHz, which correspond with the effect of the shortest remaining orbit [the one launching from the port, bouncing on wall D, and returning back, with the orbit length $L_o = 15$ cm and $L_{port(1,1)} = 1.86$ cm, and thus $c/(L_o + L_{port(1,1)}) \simeq 1.8$ GHz]. Thus, we see that nonuniversal effects of short orbits in the ensemble of a wave chaotic system can be efficiently removed by considering a few short orbits or by increasing the window size for the frequency ensemble. It is observed that the improvement of statistical properties with the short-orbit correction is more significant when the frequency window size is smaller.

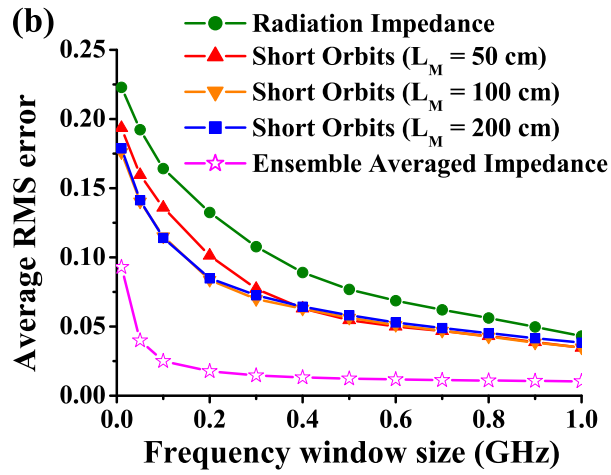
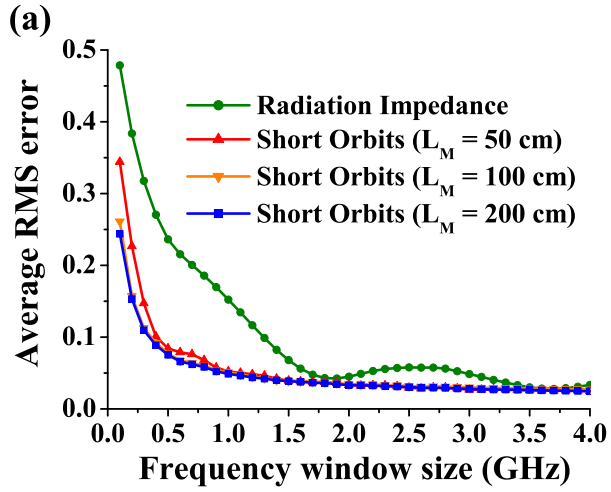


Figure 4.9: The average RMS error of the phase distributions $P(\varphi_s)$ of the eigenvalues of the normalized scattering matrices from different normalization methods and varied frequency window sizes. Shown are (a) the one-port case and (b) the two-port case.

Figure 4.9(b) shows the data of the two-port case, and the results agree with the one-port case. The average RMS errors are in general smaller because we have two times of eigenvalues in the two-port experiment than the one-port experiment. Therefore, the phase distributions are more uniform. For comparison, we also add a curve (pink stars) for the data normalized by the ensemble averaged impedance matrix $\underline{\underline{Z_{avg}}}$, and it is the most uniform case. Thus, in Chapter 5 and Chapter 6, I may directly use $\underline{\underline{Z_{avg}}}$ [Eq. (4.9)] when we need to apply the extended RCM normalization.

4.4.3 Statistics of a Single Realization

In Section 4.4.1 we see the extended RCM works similarly with $\underline{\underline{Z_{avg}}}$ or $\underline{\underline{Z_{soc}^{(LM)}}}$ to reveal the universal statistical properties of the normalized impedance matrix $\underline{\underline{z_n}}$; in Section 4.4.2 the extended RCM with $\underline{\underline{Z_{avg}}}$ works better on the statistics of the phase of the eigenvalues of the normalized scattering matrix $\underline{\underline{s_n}}$. Nevertheless, the extended RCM with the short-orbit correction is still useful when creating an ensemble of configuration realizations by perturbers is not conveniently applicable.

To show the benefit of the short-orbit correction in this stringent situation, we examine the statistical properties of the normalized impedance matrix $\underline{\underline{z_n}}$ in 500 MHz frequency windows from 6 to 18 GHz for a single realization of the empty 1/4-bowtie cavity. Random matrix theory predicts that the distribution of the complex eigenvalues of $\underline{\underline{z_n^{(LM)}}}$ should have the mean = 1 and identical standard deviations in the real and the imaginary parts [56, 57, 58]. For the one-port case, we use the

normalized impedance directly, and for the two-port case, we consider the eigenvalues of the 2×2 normalized impedance matrix. We compute the errors between the experimental results and the theoretical prediction for a series of frequency windows covering the range from 6 to 18 GHz, and the results are shown versus different short-orbit corrections with varied maximum orbit lengths L_M in Fig. 4.10.

Figure 4.10 shows that the errors (δ_μ and δ_σ) decrease upon including more short orbits in the correction (i.e., increasing L_M). In each 500 MHz frequency window, the error δ_μ is defined as the root-mean-square value of $|\mu_Z - 1|$ for the difference of the measured mean from the theoretical mean 1, and δ_σ is defined as the root-mean-square value of $|\sigma_R - \sigma_X|/(\sigma_R + \sigma_X)$ for the difference of standard deviations between the real part and the imaginary part of the normalized impedance eigenvalues. μ_Z is the means of the eigenvalues of $\underline{\underline{z_n^{(L_M)}}}$ in each window, and σ_R and σ_X are the standard deviations of the real part and the imaginary part of the eigenvalues in each window, respectively. Notice that the case of $L_M = 0$ denotes the impedance normalized by only the radiation impedance without any short-orbit corrections. For both one-port and two-port cases, the errors (δ_μ and δ_σ) decrease when we use more short orbits to remove the nonuniversal features in the complicated wave system. This verifies that using the short-orbit correction in a single realization of the wave chaotic system can more effectively reveal the universal statistical properties in the data.

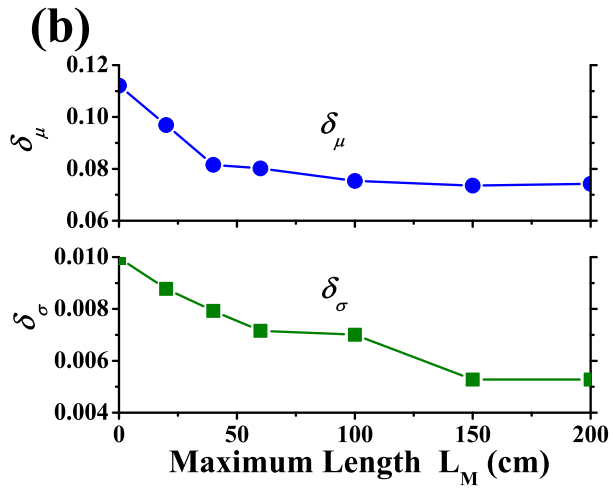
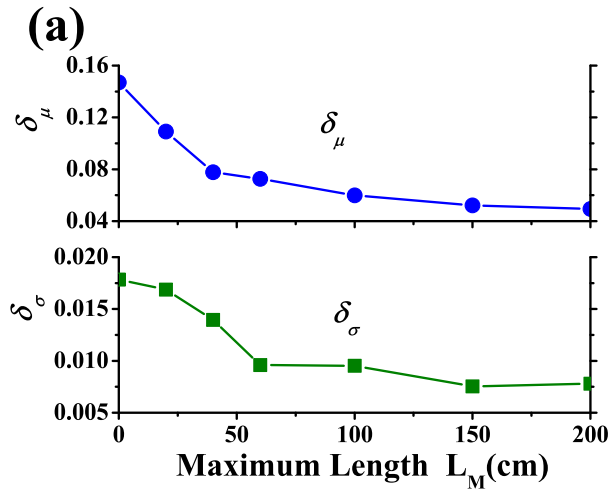


Figure 4.10: The errors for (a) the one-port experiment and (b) the two-port experiment. Shown are δ_μ for the errors in the mean (blue circles) of the normalized impedance eigenvalues and δ_σ for the errors in the standard deviations (green squares).

4.5 Chapter Summary

In this chapter we test the extended random coupling model, a theory for the nonuniversal effects of port coupling and short orbits on wave-chaotic scattering systems, in the 1/4-bowtie cavity of the one-port and the two-port systems. In particular, the theoretical predictions of random matrix theory match the statistics of the measured data in the cases of a frequency ensemble in a single realization and a configuration ensemble of 100 realizations. By removing nonuniversal effects from measured data, we can reveal underlying universally fluctuating quantities in the scattering and impedance matrices. These results should be useful in many fields where similar wave phenomena are of interest, such as nuclear scattering, atomic physics, quantum transport in condensed matter systems, electromagnetics, acoustics, geophysics, etc.

Chapter 5

Application of the Random Coupling Model in Fading

We have introduced the extended random coupling model (RCM) in Chapter 2 and also experimentally analyzed the effect of the short orbits and demonstrated the benefits of using the extended RCM in Chapter 4. The extended RCM is a statistical model for a complicated wave scattering system, and it can be applied to different kinds of waves. On the other hand, fading is a wave propagation phenomenon in complicated wave systems and is broadly studied in the field of wireless communications, satellite-to-ground links, and time-dependent transport in mesoscopic conductors [8, 76, 77, 78, 79, 80, 112]. In this chapter we apply the extended RCM to establish a statistical model of fading.

In Section 5.1, we introduce the first-principles model for fading based on the extended RCM. This random matrix theory (RMT) model of fading provides a more general understanding of the most common statistical fading models (the Rayleigh fading model and the Rice fading model) and provides a detailed physical basis for their parameters. We also report experimental tests on the 1/4-bowtie cavity and the superconducting cut-circle cavity in Section 5.2 and Section 5.3. The results show that our RMT model agrees with the Rayleigh/Rice models in the high loss regime, but there are strong deviations in low-loss systems where the RMT approach describes the data well.

5.1 Fading Model based on the Random Coupling Model

Considering wave propagation between a source and a receiver in a complex medium, fading is the time-dependent variation in the received signal strength through a complex medium due to interference or temporally evolving multipath scattering [8]. To model fading in a wave system, one can use a scattering matrix \underline{S} that describes a linear relationship between the input and the output voltage waves on a network. I consider a 2×2 scattering matrix, where the two ports of the network system correspond to the transmitter and the receiver of the wave scattering system. The complicated scattering system is modeled by the scattering matrix. The magnitude of the matrix element $|S_{21}|$ therefore corresponds to the fading amplitude, which is defined as the ratio of the received signal to the transmitted signal [8].

To apply the random matrix approach, I start with an RMT description of the 2×2 scattering matrix of a wave chaotic system, based on Brouwer and Beenakker's work in a chaotic quantum dot [21]. The scattering matrix \underline{s}_{rmt} of the time-reversal-invariant (TRI) case and $\tilde{\underline{s}}_{rmt}$ of the time-reversal-invariance-broken (TRIB) case do not contain any system-specific information and are totally ergodic. The statistics of $|s_{rmt,21}|$ and $|\tilde{s}_{rmt,21}|$ depend only on the dephasing rate γ of the quantum dot [21]. Note that the statistics of the scattering matrix generated according to Brouwer and Beenakker's formulas [21] are equivalent with the statistics of the impedance matrix generated by Zheng's method [57, 58] as $\underline{z}_{rmt} = (\underline{1} + \underline{s}_{rmt})(\underline{1} - \underline{s}_{rmt})^{-1}$, which we introduced in Chapter 2. Hemmady et al. [90] found the relationship between γ

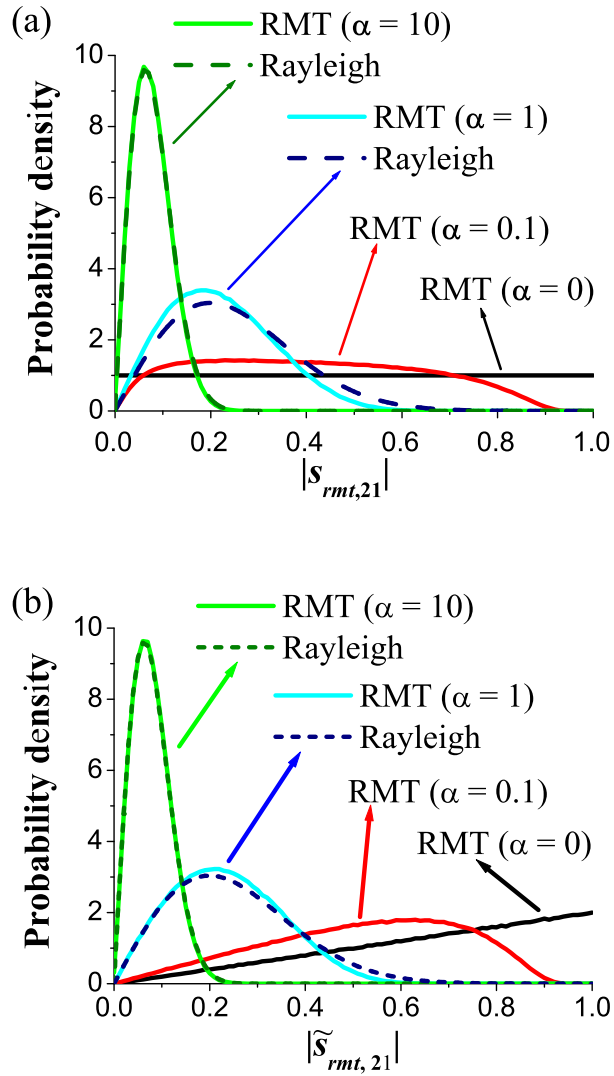


Figure 5.1: The probability density functions of the fading amplitude (a) $|s_{rmt,21}|$ for the TRI case and (b) $|\tilde{s}_{rmt,21}|$ for the TRIB case. Solid curves show the numerical results from the RMT approach with different loss parameters. For the higher loss cases ($\alpha = 1$ and $\alpha = 10$), the corresponding Rayleigh distributions are shown as dashed curves.

and the loss parameter α of the corresponding closed system as $\gamma = 4\pi\alpha$. Figure 5.1 illustrates some probability density functions (PDFs) of (a) $|s_{rmt,21}|$ for the TRI case and (b) $|\tilde{s}_{rmt,21}|$ for the TRIB case generated by the Monte Carlo method with varying loss parameters α . In practice, time-reversal invariance for wave systems can be continuously broken [26, 49, 53, 113], so in the partially broken case the statistical properties would be in between the TRI case and the TRIB case. Our group did work on partial TRI breaking in wave function statistics [49], and Schäfer's research also shows the experimental methods of partially breaking time-reversal invariance by adding magnetized ferrite objects in the wave scattering cavity [52].

In extreme loss cases, the probability density functions (PDFs) of $|s_{rmt,21}|$ and $|\tilde{s}_{rmt,21}|$ can be analytically derived [62]. For a lossless system ($\alpha = 0$), the distribution of the fading amplitude is uniform for $0 \leq |s_{rmt,21}| \leq 1$ in the TRI case, and the probability distribution $P(|\tilde{s}_{rmt,21}|)$ is a triangular distribution $P(x) = 2x$ for $0 \leq x = |\tilde{s}_{rmt,21}| \leq 1$ in the TRIB case. Both cases are illustrated as the black curves in Fig. 5.1. For high loss systems ($\alpha \gg 1$), the distribution of $|s_{rmt,21}|$ and the distribution of $|\tilde{s}_{rmt,21}|$ both go to [61, 62]

$$P(x = |s_{rmt,21}|; \alpha) = P(x = |\tilde{s}_{rmt,21}|; \alpha) = 8\pi\alpha x e^{-4\pi\alpha x^2}, \quad (5.1)$$

which is identical to the Rayleigh distribution

$$P(x; \sigma) = \frac{x}{\sigma^2} e^{-x^2/(2\sigma^2)} \quad (5.2)$$

with the relation

$$\sigma^2 = \frac{1}{8\pi\alpha}. \quad (5.3)$$

In other words, the statistics of the complex quantities $s_{rmt,21}$ and $\tilde{s}_{rmt,21}$ have the phase distributed uniformly from 0 to 2π , and the real and imaginary parts go to an independent and identically distributed Gaussian distribution of zero mean and σ standard deviation. More detailed derivations of the statistics of the fading amplitude in the high loss regime are shown in Appendix D.

The fading amplitudes $|s_{rmt,21}|$ and $|\tilde{s}_{rmt,21}|$ have not included the system-specific features yet. Therefore, in order to apply wave chaos theory to practical systems, one can convert \underline{s}_{rmt} to \underline{z}_{rmt} and then use the random coupling model [Eq. (2.7)] to describe the experimental impedance matrix as

$$\underline{Z} = i\underline{X}_{avg} + \underline{R}_{avg}^{1/2} \underline{z}_{rmt} \underline{R}_{avg}^{1/2}, \quad (5.4)$$

to combine the chaotic properties and the non-chaotic system-specific features of a wave system in the impedance domain [3, 39, 40, 41]. One then can convert the impedance matrix \underline{Z} back to the scattering matrix \underline{S} and have a complete statistical model for the measured fading amplitude $|S_{21}|$. We call this the RMT fading model. The non-zero off-diagonal elements of \underline{Z}_{avg} bring S_{21} a non-zero bias in the complex plane. In Section 5.3 we will use experimental results to show that this non-zero bias is due to the short-orbit effect, and in the high-loss limit it can be related to the ν parameter of the Rice fading model [61, 62]. The Rice fading model uses the Rice distribution

$$P(x; \sigma, \nu) = \frac{x}{\sigma^2} \exp\left(-\frac{x^2 + \nu^2}{2\sigma^2}\right) I_0\left(\frac{x\nu}{\sigma^2}\right), \quad (5.5)$$

which contains an additional parameter ν ($\nu \rightarrow 0$ recovers the Rayleigh distribution), and $I_0(\cdot)$ is the modified Bessel function of the first kind of order zero.

5.2 Comparison with the Rayleigh Fading Model

We have carried out experimental tests of the RMT fading model by measuring the complex 2×2 scattering matrix \underline{S} in two quasi-two-dimensional ray-chaotic microwave cavities, the 1/4-bowtie cavity and the superconducting cut-circle cavity introduced in Chapter 3 (Figs. 3.1 and 3.5). Both of these cavities have two coupling ports, which we treat as a transmitter and a receiver. Microwaves are injected through each port antenna, and the waves introduced are quasi-two-dimensional for frequencies below the cutoff frequency for higher order modes (~ 19 GHz) due to the thin height of the cavities (8 mm in the \hat{z} -direction). The scales of the billiards compared to the wavelengths of the microwave signals (1.7 – 5.0 cm) put these systems into the semiclassical limit. Note in both cavities, the systems are in the TRI case.

To create an ensemble for statistical analysis, we add two cylindrical metal perturbers to the interior of the 1/4 bow-tie cavity and systematically move the perturbers to create 100 different realizations. For the cut-circle cavity, the perturber is a Teflon wedge that can be rotated inside the cavity. We rotate the wedge by 5 degrees each time and create a total of 72 different realizations. The perturbers can be considered as scattering objects in the propagation medium, so changing the positions creates the equivalent of time-dependent scattering variations that give rise to fading. The 1/4 bow-tie cavity is made of copper, and measurements of the transmission spectrum at room temperature suggest the loss parameter goes from $\alpha = 0.3$ to 1.9, varying with the frequency range [41]. The superconducting

cut-circle cavity is made of copper with Pb-plated walls and cooled by a pulsed tube refrigerator to a temperature of 6.6 K, below the transition temperature of Pb [101, 102, 105]. Measurements of the transmission spectrum suggest the loss parameter from $\alpha = 0.02$ to $\alpha = 0.2$.

The experimental data show good agreement with the RMT fading model. We first use the extended RCM to reveal the universal part of the measured impedance as

$$\underline{\underline{z}}_n = \underline{\underline{R}}_{avg}^{-1/2} \left(\underline{\underline{Z}} - i \underline{\underline{X}}_{avg} \right) \underline{\underline{R}}_{avg}^{-1/2}, \quad (5.6)$$

where $\underline{\underline{Z}}$ is the measured impedance matrix, and the normalized impedance matrix $\underline{\underline{z}}_n$ is expected to correspond to $\underline{\underline{z}}_{rmt}$ in Eq. (5.4). Note that I denote this quantity as $\underline{\underline{z}}_n^{(1)}$ [Eq. (4.9)] in Chapter 4, where the superscript (1) denotes the RCM normalization with $\underline{\underline{Z}}_{avg}$. In this process we remove the system-specific features including the radiation impedance and all short orbits. Because the short-orbit effect has been removed, the situation is equivalent to the Rayleigh fading environment where no direct paths exist. By choosing data over all realizations in a 2-GHz frequency range, we can construct the distribution of $|s_{n,21}|$ and compare with the distribution of $|s_{rmt,21}|$ (the prediction of RMT). Figure 5.2 shows the distributions of the fading amplitude from the RMT model (black solid), the experimental data (red circles), and a best-matched Rayleigh distribution (blue dashed). In Fig. 5.2(a) the room-temperature case in the 1/4-bowtie cavity, the best-matched RMT model gives a value of the loss parameter $\alpha = 0.5$ for the experimental data, which corresponds to $\sigma \simeq (8\pi\alpha)^{-0.5} = 0.282$. The best-matched Rayleigh distribution yields $\sigma = 0.226$.

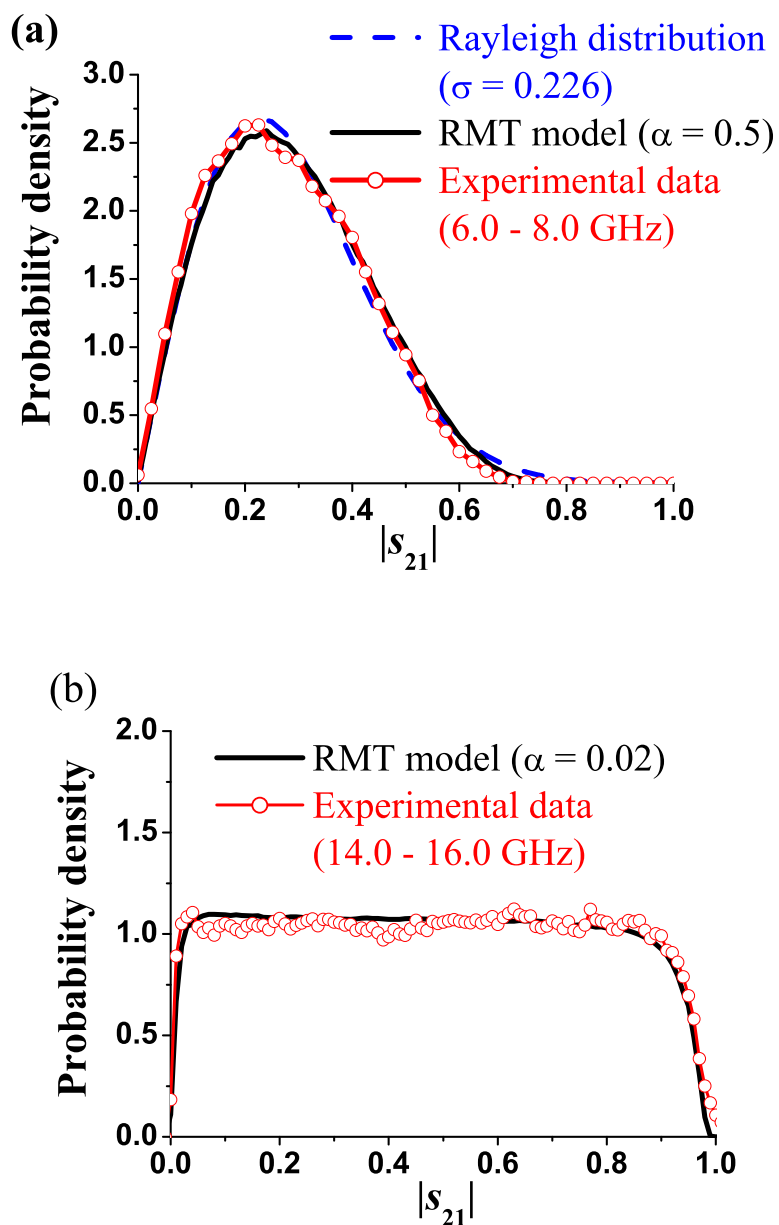


Figure 5.2: Probability density functions from the experimental data [$P(|s_{n,21}|)$, the red curves with circles] in (a) the 1/4-bowtie cavity and in (b) the cut-circle cavity, comparing with the RMT model [$P(|s_{rmt,21}|)$, the black solid curves] and the best-matched Rayleigh distribution (the blue dashed curves).

The difference in σ values is due to the fact that the loss parameter is not very large in this case. Nevertheless, both models agree with the experimental data well in this loss regime. In Fig. 5.2(b) the low temperature case in the superconducting cavity, the agreement between the experimental data and the RMT model is still good, but the distributions are never like a Rayleigh distribution. In fact, in the very-low-loss region ($\alpha \ll 1$), the long exponential tail of a Rayleigh distribution can never match the RMT theoretical distribution that is limited to $0 \leq |s_{rmt,21}| \leq 1$.

5.3 Comparison with the Rice Fading Model

According to RMT, the universal complex parameter $s_{rmt,21}$ has zero mean, but the system-specific features of short orbits (including the direct orbit between the two ports) bring about a non-zero bias in the off-diagonal elements of \underline{Z}_{avg} . Therefore, the measured S_{21} can have a non-zero mean, and this is similar in character to the Rice fading model [Eq. (5.5)]. The Rice fading model is an extension of the Rayleigh fading model in which the real and imaginary parts of S_{21} are still independent and identical Gaussian variables with variance σ^2 , but the means are generalized to a biased mean of magnitude ν . The Rice fading model is used in environments where one signal path, typically the line-of-sight signal, is much stronger than the others [8, 79, 80], and the ν parameter is related to the strength of the strong signal. More generally, we find that the RMT fading model in the high loss limit yields an explicit expression for ν in terms of the short-orbit correction matrix

$$\nu = \langle |s_{\zeta,21}| \rangle_f = \left\langle \left| \frac{2\zeta_{21}}{(1 + \zeta_{11})(1 + \zeta_{22}) - (\zeta_{21})^2} \right| \right\rangle_f, \quad (5.7)$$

and $\langle \cdot \rangle_f$ denotes frequency averaging in the corresponding frequency band. Here the short-orbit correction matrix $\underline{\underline{\zeta}}$ is the sum of short-orbit effects introduced in Eq. (2.10), and we use $\underline{\underline{\zeta}}^{(L_M)}$ to denote the sum up to the maximum orbit length L_M . The matrix $\underline{\underline{s}}_{\underline{\underline{\zeta}}} = (\underline{\underline{1}} + \underline{\underline{\zeta}})/(\underline{\underline{1}} - \underline{\underline{\zeta}})^{-1}$ is the corresponding scattering matrix of $\underline{\underline{\zeta}}$. This result generalizes the meaning of ν to include the influence of all major (short) paths. Note that when there is a single strong signal that dominates the sum of all paths, the ν parameter reverts to the original interpretation of the Rice fading model.

In the room-temperature experiment in the 1/4-bowtie cavity, the loss parameter is high enough, and we can use the result to compare the relationship between the RMT model and the Rice fading model [Eq. (5.7)]. In Fig. 5.3, we compute $\underline{\underline{\zeta}}^{(L_M)}$ to include short orbits with length up to $L_M = 200$ cm in the 1/4-bowtie cavity, apply Eq. (5.7) to compute $|s_{\zeta,21}^{(L_M)}|$, perform a sliding average over a 2-GHz frequency band, and plot $\langle |s_{\zeta,21}^{(L_M)}| \rangle_f$ as the red curve. For the ν parameter of the Rice model, we first remove the coupling features of the ports from the measured impedance matrix $\underline{\underline{Z}}$ by

$$\underline{\underline{z}} = \underline{\underline{R}}_{rad}^{-1/2}(\underline{\underline{Z}} - i\underline{\underline{X}}_{rad})\underline{\underline{R}}_{rad}^{-1/2} \quad (5.8)$$

and convert the impedance matrix $\underline{\underline{z}}$ to $\underline{\underline{s}}$. Then we compare the distribution of $|s_{21}|$ over a 2-GHz frequency band and 100 realizations with the best-matched Rice distribution. Since the σ parameter has been determined by the best-matched Rayleigh distribution as described above for the fully universal data [Fig. 5.2(a)], we can use ν as the only fitting parameter. In Fig. 5.3, we plot the ν parameters of the

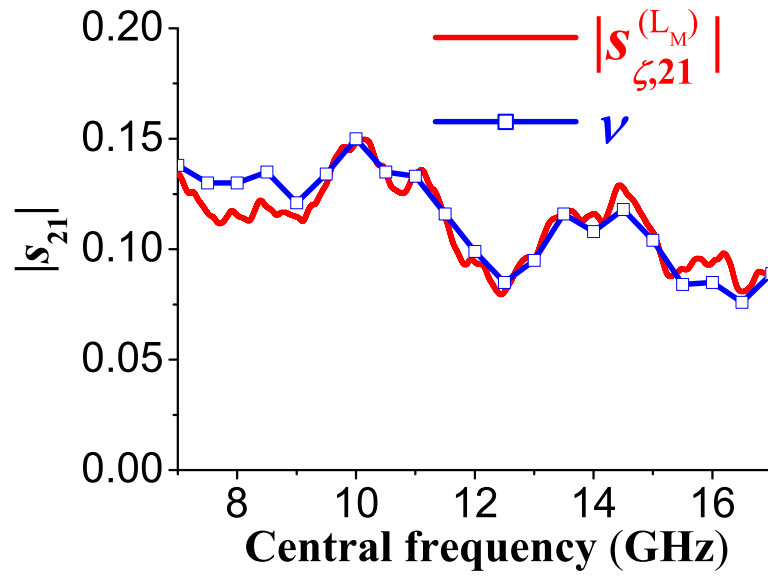


Figure 5.3: Magnitude $|s_{\zeta,21}^{(L_M)}|$ averaged over a 2-GHz frequency band versus the central frequency of the frequency band of the experimental result (red), and the ν parameter of the best-matched Rice distribution (blue square).

best-matched Rice distributions (blue squares) along with the system-specific average magnitudes of s_{21} versus the central frequency of a 2-GHz frequency band. The value of the Rice ν parameter and the system-specific feature described by the RMT model agree well.

One more advantage of applying the RCM is that we can extend the relations Eq. (5.3) and (5.7) from the normalized data to the raw measured data in the high loss cases, in which the effect of the radiation impedance \underline{Z}_{rad} of the antenna ports are included. In high loss cases, the magnitude of the elements of s_{rmt} are much less than one, so we take the approximation to the lowest order [114]. For the generalized $\tilde{\nu}$ parameter, we only need to replace the matrix $\underline{\zeta}^{(L_M)}$ in Eq. (5.7) by $\underline{Z}_{avg}(\underline{Z}_0)^{-1}$ or $\underline{Z}_{soc}^{(L_M)}(\underline{Z}_0)^{-1}$ [see Eq. (2.8)], for example

$$\tilde{\nu} = \langle |S_{soc,21}^{(L_M)}| \rangle_f = \left\langle \left| \frac{2\sqrt{Z_{0,11}Z_{0,22}Z_{soc,21}^{(L_M)}}}{(Z_{0,11} + Z_{soc,11}^{(L_M)})(Z_{0,22} + Z_{soc,22}^{(L_M)}) - (Z_{soc,21}^{(L_M)})^2} \right| \right\rangle_f, \quad (5.9)$$

where \underline{Z}_0 is a diagonal matrix representing the characteristic impedance of the ports.

On the other hand, the generalized $\tilde{\sigma}$ parameter is a function of the loss parameter α and all elements of the matrix $\underline{Z}_{soc}^{(L_M)}$ or \underline{Z}_{avg} . If the transmission between the ports is much less than the coupling reflection at the ports (i.e. $|Z_{avg,21}| \ll |Z_{avg,11}|$ and $|Z_{avg,22}|$), the modified Rayleigh $\tilde{\sigma}$ parameter can be simplified to

$$\tilde{\sigma} \simeq \sigma \frac{4\sqrt{Z_{0,11}R_{avg,11}Z_{0,22}R_{avg,22}}}{|Z_{0,11} + Z_{avg,11}| |Z_{0,22} + Z_{avg,22}|}. \quad (5.10)$$

5.4 Chapter Summary

In conclusion, we have provided a first-principles derivation of a RMT fading model. In high-loss scattering environments, this model reduces to the traditional

Rayleigh and Rice fading models, and hence it provides a more general understanding of the detailed physical basis for their parameters σ and ν . If one use the RCM to normalize out the effect of the radiation impedance \underline{Z}_{rad} , then the σ parameter is only determined by the loss parameter α of the scattering system, and the ν parameter is determined by the effect of short orbits. Moreover, in low-loss environments, the RMT model can better predict the distribution of the fading amplitude $|S_{21}|$. This is a new application of wave chaos theory in the field of wireless communications. Because fading is a general phenomenon for all sorts of waves [8, 76, 77, 78, 79, 80, 112], the RMT fading model can, in addition to the wireless communication field, also be applied to other wave scattering related applications.

Chapter 6

Wave Scattering Properties in Varied Loss Systems

The extended random coupling model (RCM) gives a complete statistical model of the impedance matrix of a complicated wave scattering system. One can use it to reveal the universal features, namely the normalized impedance matrix \underline{z}_n , by applying the RCM normalization

$$\underline{z}_n = \underline{R}_{avg}^{-1/2} \left(\underline{Z} - i \underline{X}_{avg} \right) \underline{R}_{avg}^{-1/2}, \quad (6.1)$$

where \underline{Z} is the raw cavity impedance, as we have shown in Chapter 5 and Eq. (2.15). The normalized impedance matrix \underline{z}_n can be converted to the normalized scattering matrix \underline{s}_n , and one can use these two matrices to derive more wave properties, such as the variance ratio and the thermopower. Therefore, the extended RCM can predict the statistics of all of these wave properties, and the statistics of these universal features only depend on the loss parameter α .

In Chapter 3 we introduced three microwave systems with varied loss. The superconducting cut-circle cavity has the loss parameter from $\alpha = 0.02$ to $\alpha = 0.2$ as we increase the temperature from 6.6 K to room temperature. The 1/4-bowtie cavity has the loss parameter from $\alpha = 0.3$ to $\alpha = 1.9$ for the frequency range from 6 GHz to 19 GHz. The GigaBox has the loss parameter from $\alpha = 1$ to $\alpha = 10$ for the frequency range from 3.0 GHz to 10.1 GHz. With these systems, we can test the predictions of the RCM with a wide spectrum of the loss parameter.

6.1 Impedance and Scattering Matrices

Firstly, we compare the statistics of the normalized impedance matrix \underline{z}_n , the normalized scattering matrix \underline{s}_n , and the predictions of RMT. We use the ensemble-averaged impedance \underline{Z}_{avg} to represent the system-specific features, and we remove it from the measured impedance \underline{Z} by Eq. (6.1). In Chapter 4 we have tested the results in the 1/4-bowtie cavity, and here we use four sets of data from the three different experimental systems. The first set of data is from the superconducting cut-circle cavity at the temperature 6.6 K with 72 configuration realizations and the frequency range 14 – 16 GHz. The second set of data is from the cut-circle cavity at the temperature 270 K (and therefore not superconducting) with 72 configuration realizations and the frequency range 17 – 19 GHz. The third set of data is from the 1/4-bowtie cavity at room temperature with 100 configuration realizations and the frequency range 17 – 19 GHz. The fourth set of data is from the GigaBox at room temperature with 199 configuration realizations and the frequency range 9.0 – 9.1 GHz. All of these experiments are two-port. The reason I chose these representative data sets is because their loss parameters are all different and on the order of 10^{-2} , 10^{-1} , 10^0 , and 10^1 , spanning a wide range.

For the numerical results, we generate a series of sets of the impedance matrix \underline{z}_{rmt} according to RMT [Eq. (2.2)] with varied loss parameter values (ranging from $\alpha = 0$ to $\alpha = 10$ with the step $\Delta\alpha = 0.01$), and we also derive the scattering matrix \underline{s}_{rmt} from \underline{z}_{rmt} . To determine the best-fit distribution, we compare the probability density function (PDF) of the measured results and the numerical results of the

normalized scattering matrix component $|s_{n,21}|$ (i.e. the fading amplitude). The loss parameter values of the best-fit $P(|s_{n,21}|)$ are $\alpha = 0.02$, $\alpha = 0.21$, $\alpha = 1.90$, and $\alpha = 9.31$ for the four sets of experimental data (with the coefficients of determination $R^2 = 0.9962$, $R^2 = 0.9976$, $R^2 = 0.9996$, and $R^2 = 0.9999$) respectively. The results of the best-fit PDFs will be shown in Fig. 6.2(b). I choose $P(|s_{n,21}|)$ to find the best-fit loss parameters because these results are directly from the analysis of fading statistics in Chapter 5. In addition, the scattering matrix elements are bounded in magnitude (between 0 and 1) making it more reliable for fitting than the elements of the impedance matrix, which are unbounded. Since the RCM is a complete model for the entire matrices \underline{z}_n and \underline{s}_n , the loss parameter determined from one component (i.e. $s_{n,21}$) should be able to predict the PDFs for all the other components.

Figure 6.1 shows the comparison of the PDFs of (a) the real part and (b) the imaginary part of the normalized impedance component $z_{n,11}$. Figure 6.2 shows the comparison of the PDFs of the magnitude of the normalized scattering matrix components (a) $|s_{n,11}|$ and (b) $|s_{n,21}|$. In all plots I use gray curves for the measured data from the cut-circle cavity at 6.6 K, pink curves for the measured data from the cut-circle cavity at 270 K, light green curves for the measured data from the 1/4-bowtie cavity, and light blue curves for the measured data from the GigaBox. Respectively, the numerical data are shown in dashed curves in black, dark red, green, and blue. Since the loss parameter values are determined by the best-fit to $P(|s_{n,21}|)$, Fig. 6.2(b) shows very good agreement between the experimental data and the RMT predictions. For the other plots, there are small deviations, but the agreement is still good. This shows that the extended RCM gives a complete sta-

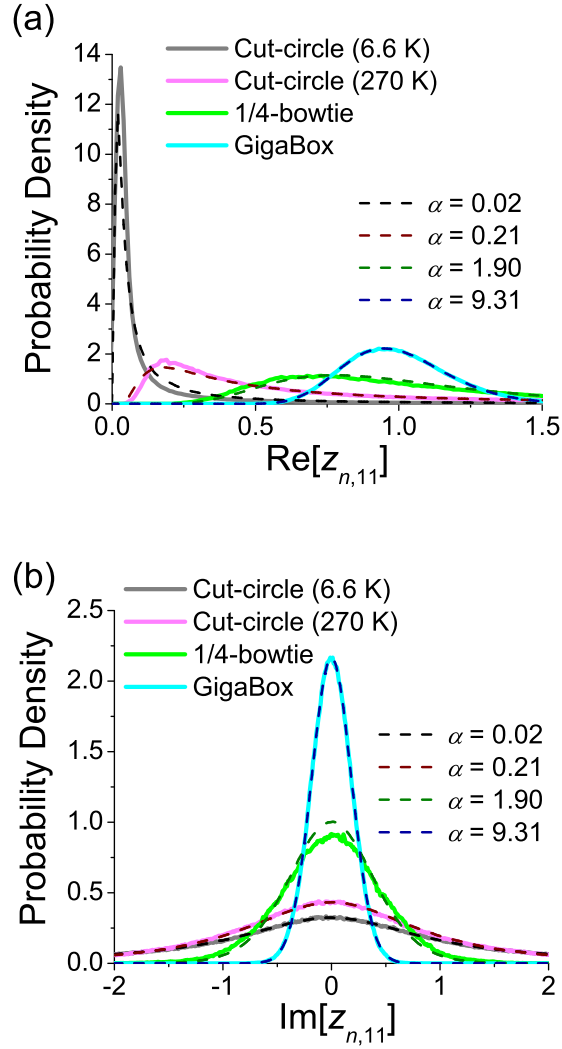


Figure 6.1: Probability density functions of (a) the real part and (b) the imaginary part of the normalized impedance component $z_{n,11}$ from four sets of experimental data. The thicker solid curves represent measured results from the cut-circle cavity at 6.6 K (gray), the cut-circle cavity at 270 K (pink), the 1/4-bowtie cavity (light green), and the GigaBox (light blue). The dashed curves are the best-fit numerical results (from fits to $P(|s_{n,21}|)$) to the four experimental results with the loss parameters shown respectively.

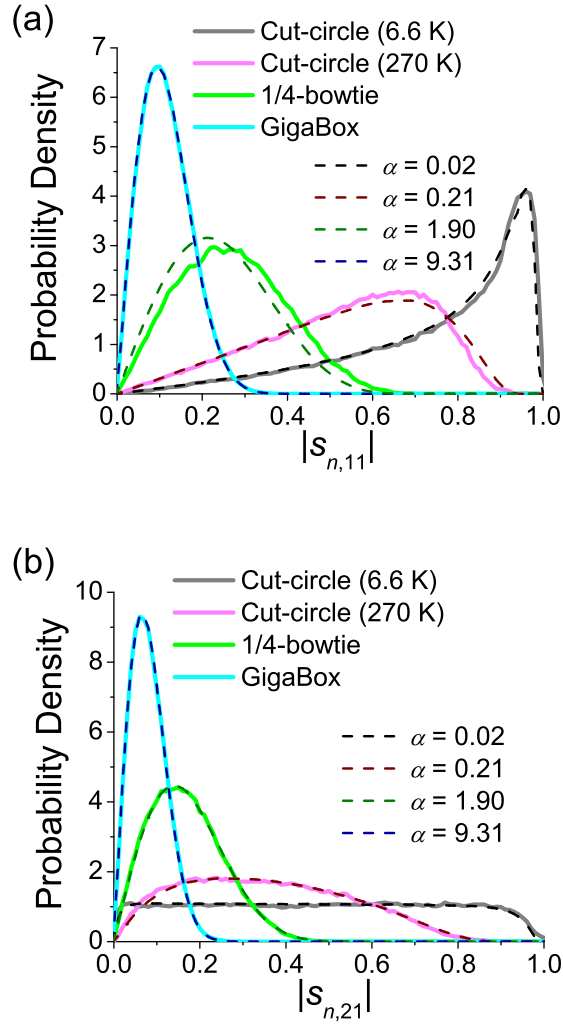


Figure 6.2: Probability density functions of the magnitude of the normalized scattering matrix components (a) $|s_{n,11}|$ and (b) $|s_{n,21}|$ from four sets of experimental data. The thicker solid curves represent measured results from the cut-circle cavity at 6.6 K (gray), the cut-circle cavity at 270 K (pink), the 1/4-bowtie cavity (light green), and the GigaBox (light blue). The dashed curves are the best-fit numerical results (from fits to $P(|s_{n,21}|)$) to the four experimental results with the loss parameters shown respectively.

tistical model for different components of the impedance matrix and the scattering matrix of a complicated wave scattering system.

Another test of the RCM is to examine the statistical properties of the phase of the normalized scattering matrix component $s_{n,21}$. RMT predicts the statistics of this quantity to be independent of the loss parameter, and the distribution should be uniform from 0 to 2π . The comparison of the PDFs of the experimental data and the theory, a uniform distribution, is shown in Fig. 6.3. It shows that the experimental PDFs are all very uniform and independent of the loss parameter.

Here we have examined the statistics of the normalized impedance matrix and the normalized scattering matrix. We can also use the extended RCM to combine the predictions of RMT (\underline{z}_{rmt}) and the system-specific features (\underline{Z}_{avg}) to examine the statistics of the raw measured impedance matrix \underline{Z} and the raw measured scattering matrix \underline{S} . Presumably the statistics should be a function of not only the loss parameter but also all of the components of \underline{Z}_{avg} . However, in the next section we will introduce the variance ratio of the impedance matrix, which is independent of \underline{Z}_{avg} , hence this variance ratio has the same value before and after the RCM normalization.

6.2 Variance Ratio

The variance ratio of the impedance matrix is defined as [59]

$$\Xi_Z \equiv \frac{\text{Var}[Z_{ij}]}{\sqrt{\text{Var}[Z_{ii}]\text{Var}[Z_{jj}]}} \quad i \neq j, \quad (6.2)$$

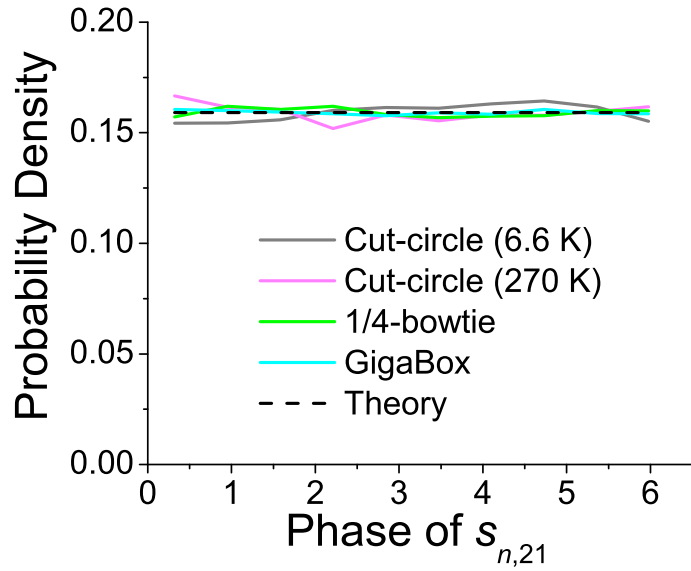


Figure 6.3: Probability density functions of the phase of the normalized scattering matrix component $s_{n,21}$ from four sets of experimental data. The thicker solid curves represent measured results from the cut-circle cavity at 6.6 K (gray), the cut-circle cavity at 270 K (pink), the 1/4-bowtie cavity (light green), and the GigaBox (light blue). The dashed black curve is the uniform distribution.

where $\text{Var}[x]$ stands for the variance of the x variable. For the experimental data, I take the variance over configuration realizations at each frequency, so $\text{Var}[x]$ is a function of frequency. Z_{ii} and Z_{jj} are the diagonal components of the impedance matrix, and they are Z_{11} and Z_{22} in the two-port case. Z_{ij} is the off-diagonal component, and it is Z_{12} or Z_{21} in the two-port case. In all of my experiments, the systems are reciprocal, i.e. $Z_{12} = Z_{21}$.

Considering the RCM normalization [Eq. (6.1)], in general the variance ratios of the impedance matrices before (\underline{Z}) and after (\underline{z}_n) the RCM normalization could be different. However, if the two ports of the wave scattering system are far apart, then the off-diagonal components of system-specific features, namely the ensemble-averaged impedance matrix components $Z_{avg,21}$ and $Z_{avg,12}$, are small and negligible [59]. More specifically, $R_{avg,11}, R_{avg,22} \gg |R_{avg,12}|, |R_{avg,21}|$. In this case, one can take \underline{R}_{avg} as a diagonal matrix. Therefore, the relationship of impedance variances over configuration realizations at a frequency f will be

$$\text{Var}[Z_{11}] = R_{avg,11}(f)\text{Var}[z_{n,11}], \quad (6.3)$$

$$\text{Var}[Z_{22}] = R_{avg,22}(f)\text{Var}[z_{n,22}], \quad (6.4)$$

$$\text{Var}[Z_{12}] = \sqrt{R_{avg,11}(f)R_{avg,22}(f)}\text{Var}[z_{n,12}], \quad (6.5)$$

and therefore

$$\Xi_Z = \Xi_{z_n}. \quad (6.6)$$

This shows the significance of the variance ratio of the impedance: the quantity is independent of the system-specific feature \underline{Z}_{avg} and is directly related to the universal fluctuating quantity \underline{z}_n whose statistics only depend on the loss parameter α [59].

Therefore, the variance ratio of the measured impedance matrix Ξ_Z is a universal property of the wave scattering system and only depends on the loss parameter α . On the other hand, the variance ratio of the scattering matrix Ξ_S does not have this universality, and we will discuss this in more detail later in this section.

We can test this prediction [Eq. (6.6)] in the experimental systems with varied loss parameter values. In each experimental system, I choose a 100 MHz frequency window where the assumption $R_{avg,11}, R_{avg,22} \gg |R_{avg,12}|, |R_{avg,21}|$ is valid, and the data are shown in Fig. 6.4. Note that if the off-diagonal terms are not negligible, the simple equations (6.3) – (6.6) will not be true. I compute the variance ratio of the impedance matrix at each frequency point over the configuration realizations and then calculate the averaged variance ratio in the 100 MHz frequency window. The results of the averaged variance ratio are shown in Fig. 6.5 versus the loss parameter on a logarithmic scale. The loss parameter values of the experimental data are $\alpha = 0.02$, $\alpha = 0.21$, $\alpha = 1.90$, and $\alpha = 9.31$ from the previous section. The results show that the relationship $\Xi_Z = \Xi_{z_n}$ is valid to good approximation in all four cases.

Zheng *et al.* have an analytical prediction for the variance ratio of impedance versus the loss parameter [59], which is shown as the blue curve in Fig. 6.5. The agreement between the theory and the experimental results is also good. However, the agreement of the lower loss cases is not as good as the higher loss cases. This is because the impedance values fluctuate enormously when the loss is reduced. In principle, as the loss parameter goes to zero, the fluctuations should diverge [57, 58]. Our numerical test of computing the variance ratio of $\underline{z_{rmt}}$ shows that the standard

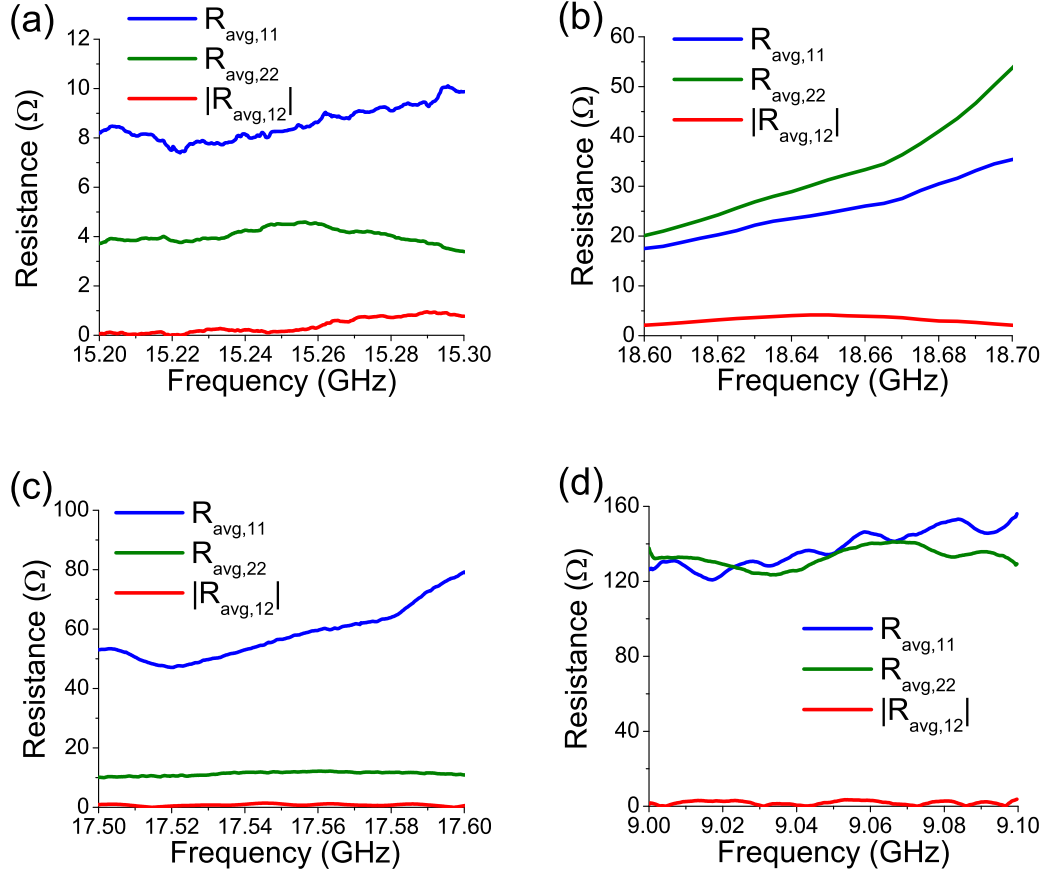


Figure 6.4: The ensemble-averaged resistances $R_{avg,11}$ (blue), $R_{avg,22}$ (green), and $|R_{avg,12}|$ (red) versus frequency in (a) the cut-circle cavity at 6.6 K over 72 realizations, (b) the cut-circle cavity at 270 K over 72 realizations, (c) the 1/4-bowtie cavity over 100 realizations, and (d) the GigaBox over 199 realizations. In all of these cases the condition $R_{avg,11}, R_{avg,22} \gg |R_{avg,12}|, |R_{avg,21}|$ is well satisfied for these data sets.

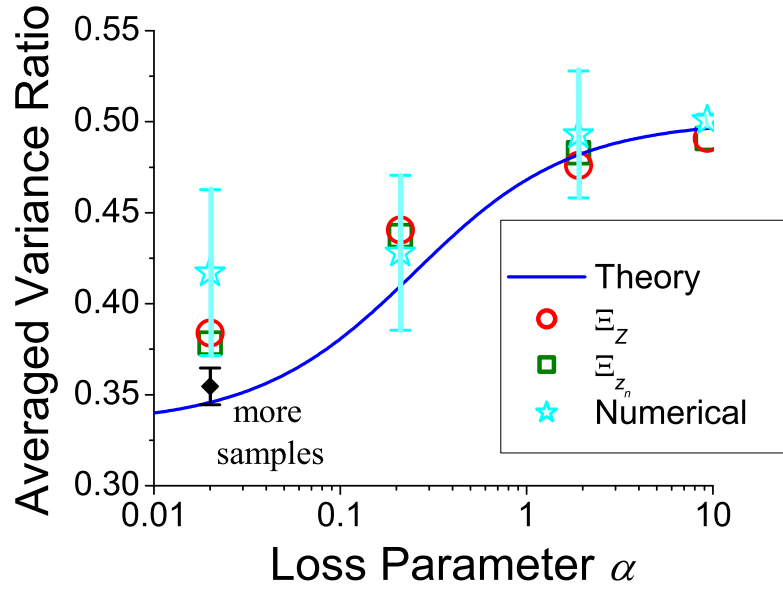


Figure 6.5: The averaged variance ratios of the impedance matrix before the RCM normalization (Ξ_Z , red circles) and after the RCM normalization (Ξ_{z_n} , green squares) from the four sets of experimental data. The blue curve is the theoretical prediction for Ξ_{z_n} versus the loss parameter α [55]. The light blue stars with error bars are the numerical data with the same ensemble sizes as the measured data. The black diamond with an error bar is the numerical result with many more samples (40001 realizations). The horizontal axis is on a logarithmic scale.

error of the averaged variance ratio (in a fixed number of realizations and in a fixed frequency range) grows as the loss parameter decreases. More specifically, I numerically generate $\underline{z_{rmt}}$ with the same loss parameters as the measured data, the same frequency windows, and the same number of realizations as the measured data. Then I compute the averaged variance ratio of the numerical data, as well as the standard error bars of the numerical data. The results are plotted in Fig. 6.5 as the light blue stars and the error bars. Note that the number of realizations (72, 72, 100, and 199 in the four sets of data, in order of increasing α) influences the accuracy of the variances and the length of the standard error bars, and the number of frequency points in 100 MHz windows (1001, 1001, 401, and 16001 in the four sets of data, respectively) for computing the average also influences the length of the standard error bars. Due to the finite number of samples, the light blue stars do not agree well with the theory (the blue curve) in lower loss cases. In the numerical test, if we increase the number of samples, the numerical results converge to the theoretical prediction. I have tried the numerical data for the $\alpha = 0.02$ case with 40001 realizations and 1000 frequency points in the 100 MHz frequency window. This result is shown as the black diamond with an error bar in Fig. 6.5. Therefore, for the lower loss cases, one needs many more realizations to get better statistics to properly calculate the impedance variance ratio.

In contrast with the variance ratio of the impedance matrix, one can similarly define the variance ratio of the scattering matrix [59]

$$\Xi_S \equiv \frac{\text{Var}[S_{ij}]}{\sqrt{\text{Var}[S_{ii}]\text{Var}[S_{jj}]}} , \quad i \neq j. \quad (6.7)$$

However, the relationship of \underline{S} and \underline{s}_n is not a simple additive equation as Eq. (6.1). Therefore, Ξ_S is not equal to Ξ_{s_n} in general. In addition Ξ_S is not universal, and there is no simple Ξ_S function of α , such as the blue curve in Fig. 6.5. Only in the high loss limit, can one make the assumption $|Z_{12}|, |Z_{22}| \ll |Z_{11}|, |Z_{22}|$, and it will lead to [59]

$$\Xi_S = \Xi_{s_n} = \Xi_Z, \quad (\alpha \gg 1). \quad (6.8)$$

I use the same data sets from Fig. 6.5 to test this prediction. The computing process is similar, but the impedance matrices are replaced by the scattering matrices. The results are shown in Fig. 6.6. The results show that the averaged Ξ_S and the averaged Ξ_{s_n} do not agree with each other in lower loss cases. However, when the loss parameter increases, the deviation between the averaged Ξ_S and the averaged Ξ_{s_n} decreases, and the value approaches 0.5, as predicted by RMT in the high-loss limit [59].

6.3 Quantum Dot Properties and the Thermopower

Another interesting application of random matrix theory (RMT) is to condensed matter physics, including the research of quantum electronics and classical and quantum optics [115]. In order to compare the experimental results with the predictions of RMT, one can use the RCM to remove the system-specific features of the condensed matter system. In this section, we focus on the RMT predictions of the properties of a quantum dot.

A common type of quantum dots are cavities etched in a semiconducting two-

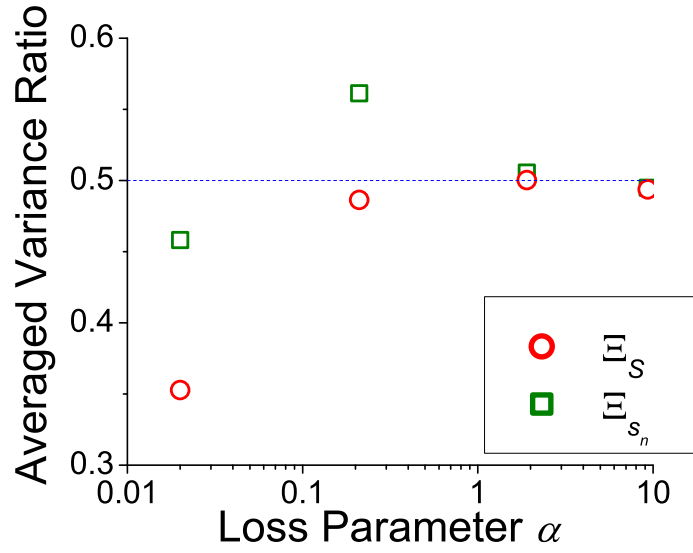


Figure 6.6: The averaged variance ratios of the scattering matrix before the RCM normalization (Ξ_S , red circles) and after the RCM normalization (Ξ_{s_n} , green squares) from the four sets of experimental data. The horizontal axis is the loss parameter α on a logarithmic scale. The blue dashed line is the theoretical prediction of Ξ_S for $\alpha \gg 1$.

dimensional electron gas. Such cavities are usually of sub-micron scale [115]. A ballistic quantum dot (the mean free path greater than the quantum dot's linear dimension) can be viewed as a wave scattering system of quantum waves. Since the wave equations are the same, researchers have utilized microwave cavities to study the statistics of the properties of a quantum dot [37, 72, 90, 94, 116]. These properties include the conductance [117, 118, 119] and the thermopower [120]. In this wave chaos (quantum chaos) analogy, the statistics of these properties can also be investigated by RMT models.

In this section, I utilize the data from the two quasi-two-dimensional microwave cavities (the cut-circle cavity and the 1/4-bowtie cavity) to test these RMT predictions. I apply the RCM normalization [Eq. (6.1)] to remove the system-specific features and unveil the perfectly-coupled impedance matrix \underline{z}_n . On the other hand, I generate numerical results \underline{z}_{rmt} , using the loss parameter values that are determined by matching the PDFs of $|s_{n,21}|$ and $|s_{rmt,21}|$. Note that the experimental and the numerical data are in the time-reversal invariant (GOE) case.

6.3.1 Transmittance

The first property we test is the transmittance τ of a quantum dot. We define the transmittance $\tau \equiv |s_{n,21}|^2$ for our two-port microwave cavity. A port of our microwave cavity is like a single-channel ballistic point contact to a quantum dot. According to the RMT prediction, the transmittance is the sum of the transmission eigenvalues of random transmission matrices [115, 119]. Schanze *et al.* have studied

the statistics of the transmittance (as the transmission coefficient in their work) in microwave cavities [94]. Our superconducting cut-circle cavity allows us to test the theoretical predictions in the previously inaccessible case, namely the extremely-low-loss case. For a lossless system ($\alpha = 0$), $P(|s_{n,21}|)$ is uniform between 0 and 1 (shown in Chapter 5), and therefore [117, 118]

$$P(\tau; \alpha = 0) = \frac{1}{2}\tau^{-1/2}. \quad (6.9)$$

I show the measured distributions of the transmittance in Fig. 6.7. In Fig. 6.7(a), the experimental data are from the superconducting cut-circle cavity at the temperature 6.6 K with 72 realizations and in the frequency range 14 – 16 GHz. In Fig. 6.7(b), the experimental data are from the 1/4-bowtie cavity with 100 realizations and in the frequency range 9 – 11 GHz. The best-fit loss parameter values are $\alpha = 0.02$ and $\alpha = 0.80$ [according to $P(|s_{n,21}|)$], respectively. The agreement between the theoretical PDFs and the experimental PDFs is very good. In Fig. 6.7(a) I add the lossless case [Eq. (6.9)] as the green curve for comparison.

6.3.2 Thermopower

Another important property of a quantum dot is the thermopower [120]. The thermopower P_{th} , or thermoelectric power, of a material is the magnitude of an induced thermoelectric voltage ΔV produced by a temperature difference ΔT across that material at zero electrical current, as

$$P_{th} = \frac{\Delta V}{\Delta T}, \quad (6.10)$$

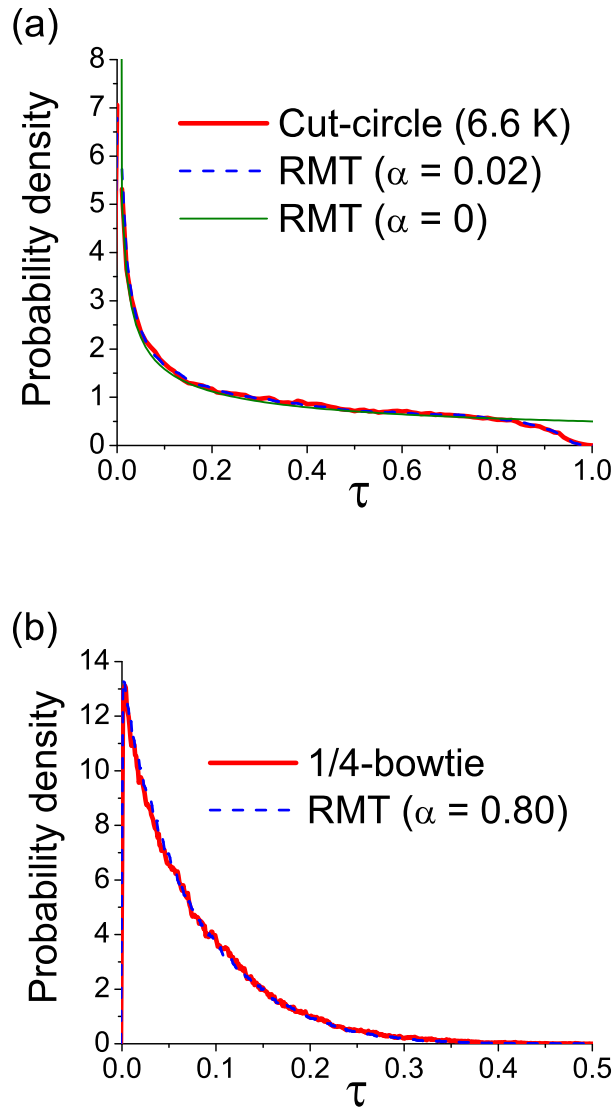


Figure 6.7: The PDFs of the transmittance τ in (a) the cut-circle cavity at 6.6 K and (b) the 1/4-bowtie cavity. Shown are the experimental data (solid red) and the numerical data (dashed blue). The thin green curve in (a) is the RMT prediction for the lossless case.

and it has units of volts per kelvin. In a chaotic quantum dot,

$$P_{th} \propto \frac{d}{dE} (\ln \tau), \quad (6.11)$$

where τ is the transmittance, and E is the energy [115, 120].

The statistics of thermopower P_{th} can be related to the symmetrized Wigner-Smith matrix

$$\underline{\underline{Q}}_{WS} = -i\hbar \underline{\underline{S}}^{-1/2} \left(\frac{d}{dE} \underline{\underline{S}} \right) \underline{\underline{S}}^{-1/2}, \quad (6.12)$$

whose eigenvalues are called proper delay times [115, 121]. These quantities not only depend on the statistics of the scattering matrix $\underline{\underline{S}}$, but also the information of the energy dependence of $\underline{\underline{S}}$ [115, 120].

In our experiments, the measured data $\underline{\underline{z}}_n$ are in the frequency domain, and the numerical data $\underline{\underline{z}}_{rmt}$ [Eq. (2.2)] can also be generated with frequency dependence [3]. The numerical method is introduced in Appendix A.1.1. Therefore, we convert the frequency spectrum to the energy spectrum and compute the energy derivatives of the impedance matrix, the scattering matrix, or the transmittance. To examine the statistics of the thermopower, we define a normalized thermopower as

$$\tilde{P}_{th} = \frac{d}{d\tilde{E}} (\ln \tau), \quad (6.13)$$

where \tilde{E} is the normalized energy $\tilde{E} \equiv k^2/\Delta k^2$, which is the eigen-energy k^2 normalized by the mean eigen-energy spacing Δk^2 . The experimental data and the generated numerical data are the same as those used in the analysis of the statistics of the transmittance τ , and the results for $P(\tilde{P}_{th})$ are shown in Fig. 6.8.

The comparison between the experimental data and the numerical data shows good agreement. For the extremely-low-loss case in Fig. 6.8(a), the thermopower

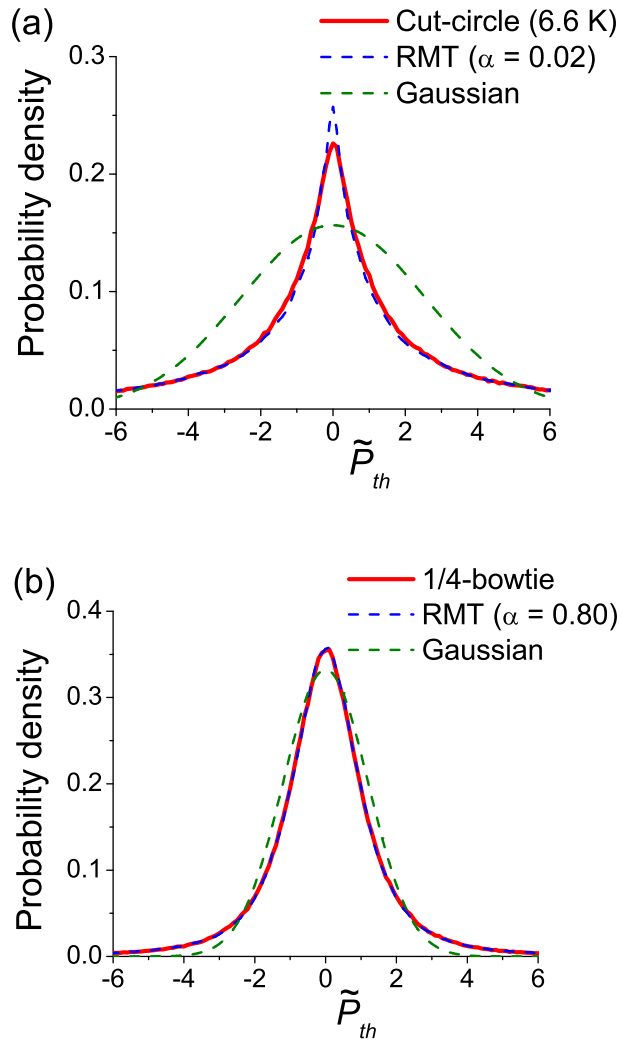


Figure 6.8: The PDFs of the normalized thermopower \tilde{P}_{th} in (a) the cut-circle cavity at 6.6 K and (b) the 1/4-bowtie cavity. Shown are the experimental data (solid red), the RMT numerical data (dashed blue), and the best-fit Gaussian distributions (dashed green) to the experimental data.

distribution is strongly non-Gaussian as the RMT prediction [115, 120]. When the loss increases, the thermopower distribution tends to a Gaussian-like distribution, as the results shown in Fig. 6.8(b).

The deviation of the experimental PDF and the numerical PDF at the peak in Fig. 6.8(a) is due to the noise in the measured data. Since the measured data have fluctuating noise as a function of frequency, when we compute the energy derivative, the chance to get a near-zero derivative is reduced. We have utilized smoothing approaches to eliminate the noise, but there are still remaining noisy fluctuations. On the other hand, we have added noise to the noise-free RMT calculation $s_{21,rmt}$ and found the same effect. In fact we added Gaussian random noise of the same magnitude (seen in the measured data, the standard deviation of the noise $\Delta s = 0.002$) and found that the PDF of \tilde{P}_{th} of the noisy RMT calculation agrees almost exactly with the data (see Fig. 6.9).

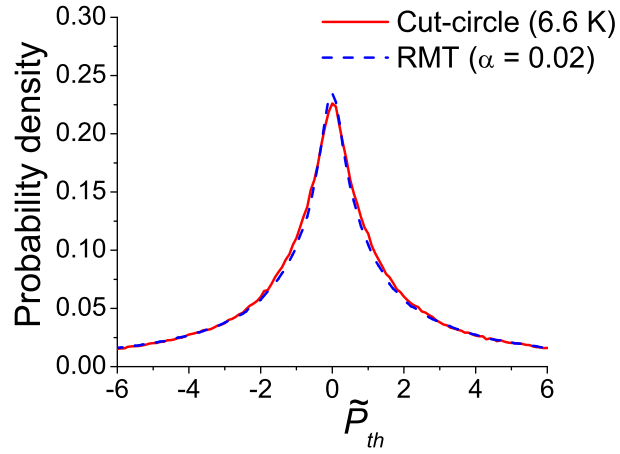


Figure 6.9: The PDFs of the normalized thermopower \tilde{P}_{th} in the cut-circle cavity at 6.6 K. Shown are the experimental data (solid red) and the RMT numerical data with additional noise in $s_{rmt,21}$ (dashed blue). Compare to Fig. 6.8(a).

Chapter 7

Conclusions and Future Work

7.1 Conclusions

Wave scattering in a complicated environment is a common challenge in many engineering fields because the complexity makes exact solutions impractical to find. On the other hand, chaos theories offer useful approaches to analyze the statistical properties of these complicated dynamical systems [27]. Therefore, there is great interest in studying the wave properties of systems that show chaos in the semiclassical (short wavelength, or ray) limit [11]. These wave-chaotic systems appear in many contexts, including nuclear physics, acoustics, quantum dots, and electromagnetic enclosures.

Researchers have developed wave-chaotic models to understand wave statistics in complicated scattering environments. The random coupling model (RCM) is one wave-chaotic approach that applies ideas from the field of wave chaos to practical questions in complicated scattering environments [2]. The theory of the RCM has been extended to combine universal wave-chaotic features and the specific details of a practical system [4], and the extended RCM is the core theory of this dissertation.

In this dissertation I first introduced the wave chaos theory, random matrix theory (RMT) [1], and reviewed the development of the random coupling model [2, 3, 4]. One of my major contributions is to thoroughly test the RCM and the

short-orbit correction in a wave scattering system with a quasi-two-dimensional microwave cavity [40, 41]. The experimental results show that the extended RCM can well describe the statistics of a complicated wave scattering system even under stringent conditions, such as a single configuration realization or a small frequency window.

In addition to the quasi-two-dimensional microwave cavity, I have utilized two more experimental systems to test the extended RCM in systems with varied loss. In order to achieve extremely-low-loss, I have used a superconducting microwave cavity and built an *in-situ* broadband cryogenic calibration system to measure wave scattering properties [108]. For the high loss limit, a three-dimensional microwave cavity offers a high-loss wave scattering environment.

Another contribution of this dissertation is demonstrating new applications of the RCM. One application is for the fading phenomenon of wave propagation in a complicated system, which is well known in the wireless communication field [8]. The extended RCM offers a complete model for fading statistics [61, 62], which encompasses the traditional Rayleigh and Rice fading models as its high-loss limit case and further predicts the fading statistics to the low-loss limit. Other applications of the extended RCM include offering a complete statistical model for wave properties, such as the impedance matrix, the scattering matrix, the variance ratio, and the thermopower. These results are beneficial for physical and engineering fields, including nuclear scattering, atomic physics, quantum transport in condensed matter systems, electromagnetics, acoustics, geophysics, etc.

7.2 Future Work

I have experimentally tested and applied the extended random coupling model in linear microwave systems with time-reversal invariance (the GOE case). There are other interesting systems where we have not tested the RCM yet, such as mixed (regular and chaotic) systems, time-reversal invariance broken (TRIB, the GUE case) systems, and nonlinear wave systems. One would want to ask if the RCM can be extended to these systems. In order to answer this question, I will explain these systems in the following sections and point out possible experimental systems for testing the RCM. Another direction for the future work is utilizing the information of short orbits to locate the source of emitted waves in a complex scattering environment.

7.2.1 Random Coupling Model for Mixed Systems

In Chapter 1, I have introduced wave scattering systems whose boundaries are a billiard with a ray-chaotic shape. More generally, according to the shape, there are three categories of billiards: (i) chaotic, (ii) integrable, and (iii) mixed. For example, the 1/4-bowtie and the cut-circle are both chaotic billiards. A rectangular box like the GigaBox is an integrable billiard, but we add perturbers in the GigaBox cavity to make it a complicated wave scattering system. For the third type, the mixed billiards are systems where there are chaotic regions and integrable regions in their phase space [27, 122]. Fig. 7.1 gives some examples of mixed billiards, as (a) a cut-circle with a circular insert, (b) an annular billiard, (c) a 1/2-mushroom billiard,

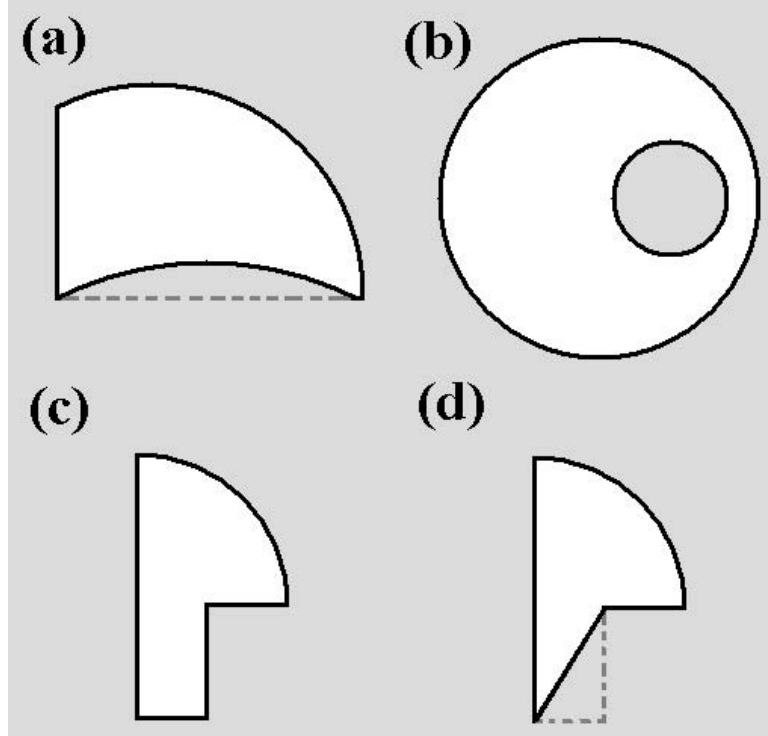


Figure 7.1: Mixed two-dimensional billiards: (a) a cut-circle with a circular insert, (b) an annular billiard, (c) a 1/2-mushroom billiard, and (d) a 1/2-mushroom billiard with a triangular stem.

and (d) a 1/2-mushroom billiard with a triangular stem.

The RCM introduced in this dissertation assumes the wave system is purely chaotic in the semiclassical limit. Ming-Jer Lee *et al.* in our group have established a more extended RCM [122] to encompass the mixed wave systems by modifying the RCM expression [Eq. (2.7)] to

$$\underline{Z} = i\underline{X}_{avg} + \underline{A}_C^{1/2} \underline{R}_{avg}^{1/2} \left(\underline{z}_{rmt} \right) \underline{R}_{avg}^{1/2} \underline{A}_C^{1/2} + \underline{A}_I^{1/2} \underline{R}_{rad}^{1/2} \left(\underline{z}_{int} \right) \underline{R}_{rad}^{1/2} \underline{A}_I^{1/2}. \quad (7.1)$$

$\underline{\underline{A_C}}$ and $\underline{\underline{A_I}}$ are diagonal matrices of the weight coefficients of the chaotic portion and the integrable portion in the phase space [122]. The elements of $\underline{\underline{A_C}}$ and $\underline{\underline{A_I}}$ are functions of the port positions, i.e. $A_{C,nn} = A_{C,nn}(\vec{r}_n)$ and $A_{I,nn} = A_{I,nn}(\vec{r}_n)$ for $1 \leq n \leq N$, where \vec{r}_n is the position vector of the n^{th} port. For each port, the weight coefficients of the chaotic portion and the integrable portion are determined by the position of the port in the billiard, and $A_{C,nn} + A_{I,nn} = 1$ with $0 \leq A_{C,nn} \leq 1$ and $0 \leq A_{I,nn} \leq 1$. If the ports are in the purely chaotic regions, $\underline{\underline{A_C}}$ becomes an identity matrix, $\underline{\underline{A_I}}$ vanishes, and the RCM expression goes back to Eq. (2.7). $\underline{\underline{z_{int}}}$ is the impedance matrix for orbits originating from the ports in the integrable regions, and it is also a deterministic quantity depending on the positions of the ports [122]. Therefore, only $\underline{\underline{z_{rmt}}}$ is a random matrix based on RMT, and all of the other terms are deterministic and can be measured or calculated by knowing the geometry of the boundary shape and the port positions.

The theoretical model of the RCM for mixed systems is developed [122], and some examples of the mixed billiards are shown in Fig. 7.1. Therefore, one can build a wave scattering system with a cavity of one of these mixed billiards, and then one can do experiments by using a network analyzer (as the experimental systems in Chapter 3) to test the RCM [Eq. (7.1)]. This can broaden the range of applications of the RCM.

7.2.2 Random Coupling Model for TRIB Systems

Another way to broaden the range of applications of the RCM is to expand it to time-reversal invariance broken (TRIB) systems. The random matrix theory for TRIB systems is ready, so one can generate $\underline{z_{rmt}}$ in the GUE case [13, 17, 57, 58]. Zheng and Hemmady *et al.* have developed the TRIB version of the original RCM [57, 58, 88]. For the extended RCM [Eq. (2.7)], the calculation of the short-orbit correction (for $\underline{z_n^{(LM)}}$) and the measurement of the ensemble-averaged impedance $\underline{Z_{avg}}$ can also be generalized to the TRIB systems [39]. Therefore, the expression of the RCM for TRIB systems is similar to the TRI version as

$$\underline{Z^{(TRIB)}} = i \underline{X_{avg}^{(TRIB)}} + \left(\underline{R_{avg}^{(TRIB)}} \right)^{1/2} \left(\underline{z_{rmt}^{(TRIB)}} \right) \left(\underline{R_{avg}^{(TRIB)}} \right)^{1/2}. \quad (7.2)$$

This expression is for a pure TRIB system. In practice, researchers have found that the time-reversal invariance for wave systems can be continuously broken [26, 49, 53, 113], so one may need to introduce weight coefficients for the partially broken cases, like what we introduced for the mixed systems. Our group have worked on partial TRI breaking in wave function statistics [49], and Schäfer's research also shows the experimental methods of partially breaking time-reversal invariance by utilizing magnetized ferrite objects in the wave scattering cavity [52]. Researchers have also used quantum dots in an external magnetic field to test RMT in the TRIB cases [120].

The partially time-reversal invariance broken RCM would provide a more complete fading model as we introduced in Chapter 5 and thermopower model as we introduced in Chapter 6. Applications of this research include satellite-to-ground

communications in which waves propagate through the ionosphere [79, 123, 124] and quantum dots in an external magnetic field [120]. One challenge is to achieve a low-loss TRIB system since external magnetic fields and magnetized ferrite objects all increase the loss parameter of the system [94, 120]. In the high loss cases, the statistics of wave properties, such as the fading amplitude, are similar in the TRI case or in the TRIB case. Therefore, one would like to build a low-loss system in order to observe a clear difference in the statistics.

7.2.3 Random Coupling Model for Nonlinear Systems

All of the wave systems we have discussed are assumed to be linear, and we have used linear wave equations to describe the wave scattering. However, there are wave systems with strong nonlinearity in the real world, and one cannot approximate these nonlinear wave systems by linear wave equations. In the following section, I will introduce rogue waves as an example and discuss the application of the RCM to this nonlinear wave system.

7.2.3.1 Rouge Waves

One new application of the wave chaos approach is to study rogue waves. Rogue waves, also known as freak waves or giant waves, are waves of extreme height relative to the typical wave in a given sea state [125]. Because of their extreme height, rogue waves are a significant risk to cargo ships and even to large cruise liners. Documents show damage to oil platforms or ships caused by rogue waves

[125]. Therefore, there is great interest to build a statistical model or to understand the fundamental origins of this rogue wave phenomenon.

The Longuet-Higgins random seas model offers a simple statistical model for the occurrence of rogue waves by assuming linear superposition of many random plane waves with different directions and wavelengths [126]. This model predicts that the probability of crest height h follows a Rayleigh distribution in the limit of a narrow frequency spectrum. However, observational data [127] suggest that the actual probability of rogue waves should be significantly higher than the prediction of this pure stochastic Rayleigh model. Several alternative theories of the rogue wave phenomenon have appeared and have been reviewed in Ref. [128].

An extensively studied mechanism for the formation of rogue waves is nonlinear instability effects [129], in which the instabilities depend sensitively on initial conditions. For a generic random sea state, the full numerical computations are costly, and deriving quantitative predictions of the statistics of the crest height h is difficult, except in approximations such as the nonlinear Schrödinger (NLS) equation [130, 131, 132]. These methods are valid for small to moderate values of the wave steepness. In addition to purely nonlinear effects, other researchers suggest that strongly nonlinear evolution is likely to be triggered in an initial condition where the waves are already unusually high [125]. Combining a linear triggering mechanism, such as the focusing or refraction of an incoming plane wave by random current eddies [133, 134] with nonlinear evolution is a potential model for quantitative predictions of the rogue wave statistics.

Recently, the research on rogue waves has gathered more interest. More non-

linear theories have been suggested by Peregrine as the solutions (the so-called Peregrine soliton) of the scalar NLS equation [135] and by Baronio *et al.* as the solutions of the vector NLS equation [136]. The existence of rogue waves has been observed not only in oceans [137], but also in the atmosphere [138], in optics [139, 140, 141], in plasmas [142], in Bose-Einstein condensates [143], and in microwave scattering cavities [144]. Chabchoub *et al.* have also presented experimental results of the Peregrine soliton in a water wave tank [145].

7.2.3.2 Nonlinear Wave Models

The existing random coupling model has been applied to linear wave systems. Extending the applications of the RCM to include nonlinear dynamics is an interesting objective. One potential application for this nonlinear model is for studying rare intense events or rogue waves, which can cause severe damage and have been observed in varied wave systems [136]. Previous work has investigated rogue wave phenomenon by microwaves on purely linear systems [144, 146]. It would be more interesting to analyze systems that include nonlinearity.

Many researchers have used nonlinear Schrödinger (NLS) equations to model nonlinear self-reinforcements presented in the rogue wave phenomenon [147]. In particular, the two-dimensional NLS equation is

$$\frac{\partial u}{\partial t} = iA_N|u|^2u + iA_L\nabla^2u, \quad (7.3)$$

where the amplitude $u = u(x, y, t)$, and A_N and A_L are coefficients of the nonlinear term and the Laplace term, respectively. A more generic NLS equation is the com-

plex Ginzburg-Landau (CGL) equation [148], which can be viewed as a dissipative extension of the nonlinear Schrödinger equation. One can consider the CGL equation on a two-dimensional domain, which corresponds to the quasi-two-dimensional wave cavities.

In order to study the nonlinear model, one will need to add nonlinearity in the wave system. The results of this research can be applied to investigate the relationship between the formation of rogue waves and nonlinear dynamics.

7.2.3.3 Proposal of Experimental Systems

Researchers have investigated rogue wave phenomenon in linear microwave cavities [144, 146]. We would like to use our chaotic microwave cavities with nonlinearity to test the model of the CGL equation. One idea is to connect diodes as a net structure and put it evenly in the 1/4-bowtie cavity. The diodes will be biased by an external voltage, and the microwave will be used to trigger the nonlinearity of the diodes. When the microwaves propagate in the cavity, these evenly distributed diodes will become nonlinear sources with a quite homogeneous distribution. Because the nonlinear wave phenomenon is modeled by the NLS equation, one can tune the coefficients of the equation to achieve rogue wave solutions (such as the Peregrine solitons [136]). The advantage of a diode net is that one can adjust the distribution of the nonlinearity sources, and the experimental parameters can be designed based on Eq. (7.3) or the CGL equation.

In order to measure the rogue wave phenomenon, which is in the space and

time domain, it will be better to have a movable scanning antenna rather than fixed antennas [144]. In the original design of the 1/4-bowtie cavity, the ports are all fixed. Therefore, one can build a scanning lid for the measurement, in which one can translate the position of a port by shifting the lid. Notice that the vector network analyzer actually measures the scattering matrix in the frequency domain, but one can transfer it to time domain by the Fourier transform. The challenge is that the diode net may make the system very lossy, and the nonlinearity may not be strong enough.

7.2.4 Source Localization

Short orbits are considered a system-specific feature in the extended RCM [39, 40]. James Hart has developed an algorithm for finding short orbits in a two-dimensional cavity with given geometry, and Bo Xiao in our group has developed a more complete algorithm. Based on this algorithm and the quasi-two-dimensional microwave cavities with perturbers, one can further analyze the effect of short orbits and utilize the information of short orbits for other applications, such as source localization and energy focusing.

One application is to utilize the information of short orbits to create a source localization algorithm. Given measurements with an ensemble of perturber locations, I have investigated the relationship between perturber locations and the strength of the short-orbit effect of each individual orbit. These short orbits are like a fingerprint of the geometry of the wave scattering system. Fig. 7.2 shows an example of

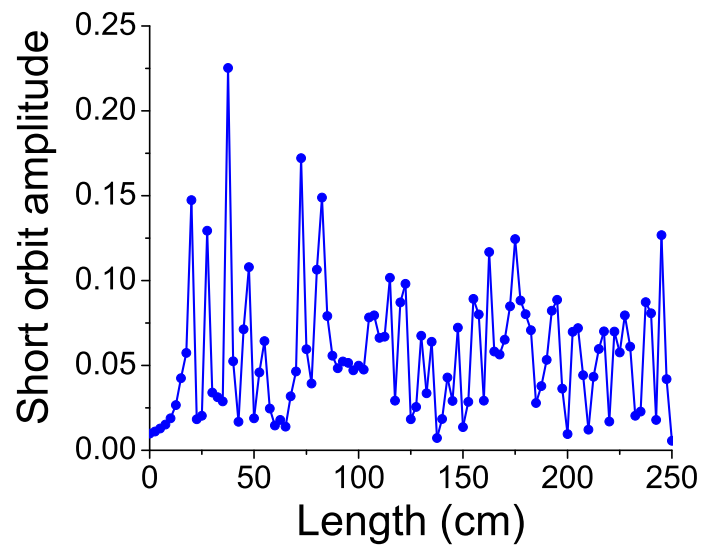


Figure 7.2: The short orbit amplitude versus the orbit length in one realization of the two-port 1/4-bowtie cavity with two perturbers.

the short orbit amplitude versus the orbit length in the two-port 1/4-bowtie cavity with two perturbers. The short orbit amplitude $|\text{IFT}\{z_{cor,21}(f)\}|$ is computed by the inverse Fourier transform of the impedance correction matrix component $z_{cor,21}$ [Eq. (4.2)], where $\text{IFT}\{\cdot\}$ stands for the inverse Fourier transform, and the horizontal axis of Fig. 7.2 is transformed from the time domain to the length domain. One can analyze short orbits that are created or destroyed at each perturber location and use this information to make a series of estimates of the distance to the source. Therefore, it is possible to create an algorithm that utilizes the short orbit information and perturber locations to find out the location of another port, or at least construct the best estimate of the port location. This algorithm could be used to discover a wave source, which might be useful for wireless communication, radio frequency coupling to a target, and other localization applications.

I have created an algorithm to utilize the short-orbit information to find the wave source, and this algorithm has been tested in the 1/4-bowtie cavity experiment. In this two-port system, one port is treated as an observer, and the other port is the wave source that the algorithm aims to discover. We use the known geometry of the cavity, the locations of the perturbers, and the measured short-orbit information ($|\text{IFT}\{z_{cor,21}(f)\}|$) to find the possible locations of the other port. The algorithm makes a grid on the quasi-two-dimensional 1/4-bowtie cavity, where the size of the grid cells is equal to 1/2 of the applied wavelength, and the algorithm computes the possibility of the wave source being located in each grid cell. Examples of the results of this algorithm are shown in Fig. 7.3. Fig. 7.3(a) shows the geometry of the cavity and the positions of the two perturbers (blue circles). The two red dots are

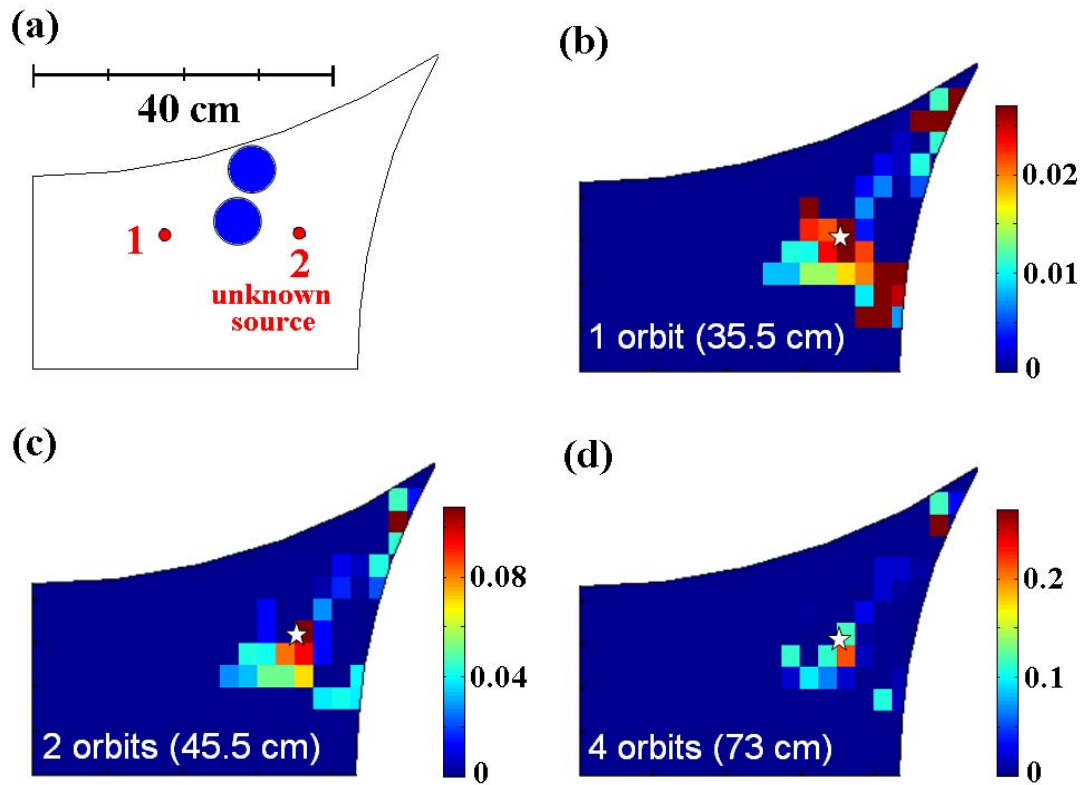


Figure 7.3: (a) The 1/4-bowtie cavity, the two ports (red dots), and the two perturbers (blue circles). The wave source probability distributions are shown as (b) with the information of one short orbit, (c) with the information of two short orbits, and (d) with the information of four short orbits. In each case, the longest orbit length is shown, and the white star indicates the correct position of the wave source.

the positions of the ports, and Port 1 is the observer; Port 2 is the unknown wave source. Three examples of the results of this algorithm are illustrated in Fig. 7.3, as (b) utilizing information of one short orbit, (c) utilizing information of two short orbits, and (d) utilizing information of four short orbits. The probability in each cell is color-coded as the color bar shows, and the white star indicates the correct position of Port 2.

The results in Fig. 7.3 show that the high probability region of the wave source narrows down when the algorithm includes more information of short orbits. However, there is an error in the upper right corner of the cavity, where the probability is high, but the location is wrong. One may improve this algorithm by including additional short orbits.

Another application of utilizing short orbits is creating coherent-in-time-and-space spikes of electromagnetic energy after propagation through a cluttered environment. Each orbit can be viewed as a wave propagation channel, and short orbits can be viewed as independent channels when the length difference between two orbits is much larger than the wavelength. The many independent channels of propagation through a cluttered environment allow one to stimulate them independently with a superposition waveform. By carefully considering the phases of pulses and the lengths of short orbits, one can compute a synthetic waveform which makes a series of pulses through different channels accumulate a strong spike at a controllable point in time and space. This algorithm will be beneficial for energy focusing applications.

Appendix A

Numerical Algorithms

A.1 Impedance Matrix Based on Random Matrix Theory

In Sec. 2.1.1, I have introduced how we numerically generate the impedance matrix $\underline{z_{rmt}}$ based on random matrix theory. In this section, we discuss more details of the numerical algorithm of generating $\underline{z_{rmt}}$.

For an N -port system, $\underline{z_{rmt}}$ is an $N \times N$ matrix. Eq. 2.2 gives the impedance matrix based on random matrix theory in the Gaussian orthogonal ensemble (GOE) case. From Eq. 2.2, the (a, b) element of $\underline{z_{rmt}}$ is

$$z_{rmt,a,b} = \frac{-i}{\pi} \sum_{m=1}^M \frac{W_{am}W_{bm}}{\lambda_m^{(rmt)} - i\alpha}. \quad (\text{A.1})$$

This element $z_{rmt,a,b}$ represents the impedance element between Port a and Port b , and the sum is over the M eigenmodes of the wave scattering enclosure, where W_{am} (or W_{bm}) stands for the coupling between the Port a (or the Port b) and the m^{th} eigenmode. Based on the assumption of the random plane wave hypothesis [57], W_{am} and W_{bm} are independent Gaussian random variables of zero mean and unit variance. $\lambda_m^{(rmt)}$ is the m^{th} eigenvalue of the wave scattering enclosure, and it is generated based on random matrix theory [3]. Note that α is the dimensionless loss parameter, and it is determined by the system of interest.

The algorithm of generating $\lambda_m^{(rmt)}$ has been introduced in Sameer Hemmady's

thesis (in Sec. 2.5) [3]. For the GOE case (time-reversal-invariant), one first generates a big $M \times M$ random matrix (with $M > 1000$) where (i) the diagonal elements are independent Gaussian random variables of zero mean and unit variance; (ii) the off-diagonal elements are independent Gaussian random variables of zero mean and $1/2$ variance. The second step is to computing the M eigenvalues $\lambda^{(0)}$ of the $M \times M$ random matrix. According to random matrix theory, the $M \times M$ random matrix needs to be large in order to reduce the finite-sample-size problem. However, computing eigenvalues of a big matrix requires a large amount of computational resources. This original algorithm used a MATLAB function to directly operate the matrix decomposition, and the computation process was time consuming. Ming-Jer Lee in our group has written a modified MATLAB code which transforms the big matrix to a sparse matrix first and then computes the eigenvalues of the sparse matrix [149]. His code significantly accelerates this computation, so we can do $M = 10^6$ now. For large M , the eigenvalues $\lambda^{(0)}$ have a semi-circle distribution following “Wigner’s Semi-Circle Law” [1]. The third step of this algorithm is applying a mapping function (Eq. 2.15 in [3]) which transforms $\lambda^{(0)}$ (with a semi-circle distribution) to $\lambda^{(rmt)}$ (with a uniform distribution). Finally, the M generated eigenvalues $\lambda^{(rmt)}$ are inserted in Eq. A.1.

For our experiments, we only need to generate 2×2 $\underline{z_{rmt}}$ matrices. Note that $z_{rmt,12} = z_{rmt,21}$ due to reciprocity of the network system, and $z_{rmt,11}$ and $z_{rmt,22}$ have the same statistics according to Eq. A.1. Figure A.1 shows examples of the numerically generated $z_{rmt,11}$ and $z_{rmt,12}$ in the complex plane with the loss parameters $\alpha = 0.1$ and $\alpha = 1.0$.

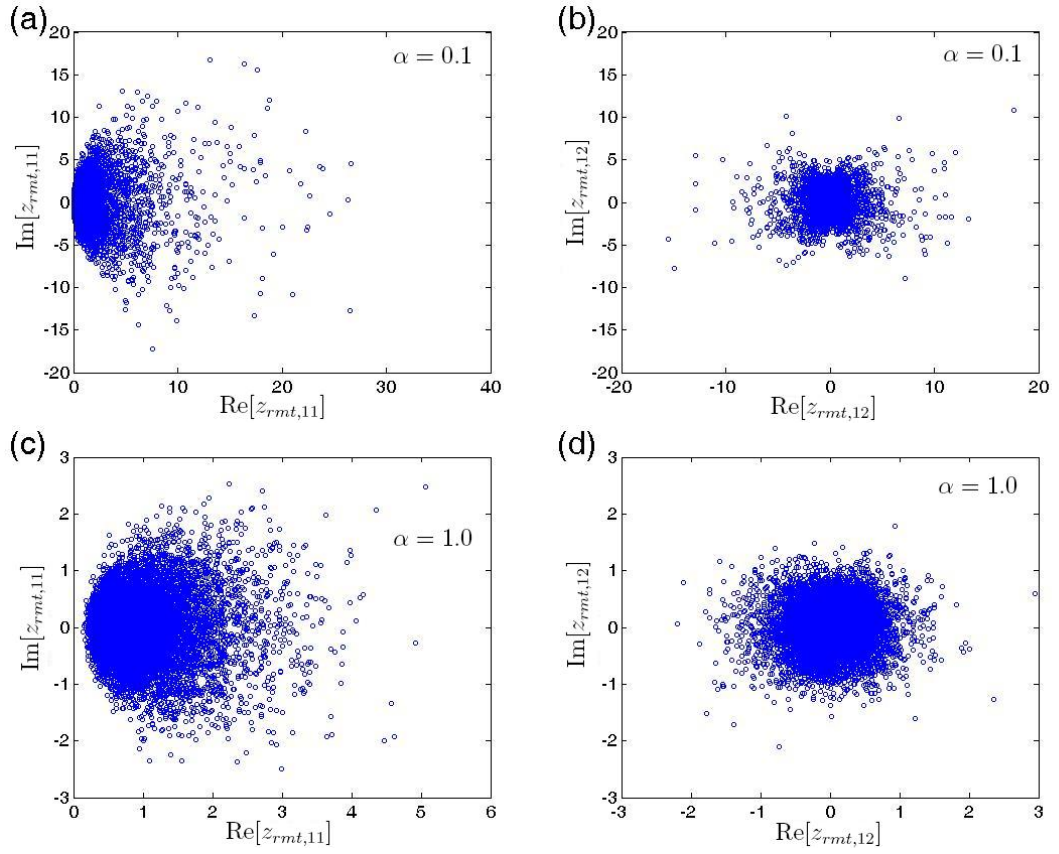


Figure A.1: Shown are examples (blue circles) of (a) $z_{rmt,11}$ with $\alpha = 0.1$, (b) $z_{rmt,12}$ with $\alpha = 0.1$, (c) $z_{rmt,11}$ with $\alpha = 1.0$, and (d) $z_{rmt,12}$ with $\alpha = 1.0$ in the complex plane. Each plot has 10000 samples from Eq. A.1, and $M = 10^6$.

A.1.1 Frequency Dependence of z_{rmt}

If one took the loss parameter as constant, the impedance matrix $\underline{z_{rmt}}$ generated by Eq. A.1 has no explicit frequency dependence. This expression of the impedance is a simplified version. When frequency dependence is not of concern, this form is convenient and requires less computation time. In Sec. 6.3.2, we discuss the statistics of the thermopower which concerns the energy derivative of the transmittance, and therefore, the frequency-dependent version of $\underline{z_{rmt}}$ is needed. Xing Zheng *et al.* has introduced the frequency-dependent $\underline{z_{rmt}}$ as [57, 58]

$$z_{rmt,a,b}(k) = \frac{-i}{\pi} \sum_{m=1}^M \frac{W_{am}W_{bm}}{\left(\frac{k^2-k_m^2}{\Delta k_m^2}\right) - i\alpha}, \quad (\text{A.2})$$

where $k = 2\pi f/c$ is the wave number, f is the frequency of the wave, and c is the speed of light. Here Δk_m^2 is the mean spacing of the eigen-energies (k_m^2). Comparing with Eq. A.1, the frequency-independent $\lambda_m^{(rmt)}$ has been replaced by the frequency-dependent $\left(\frac{k^2-k_m^2}{\Delta k_m^2}\right)$. Note that the loss parameter can also be frequency-dependent.

With Eq. A.2, one can numerically generate $z_{rmt,a,b}$ over a frequency window. Note that Eq. A.2 is based on the assumption of random matrix theory and the random plane wave hypothesis, so it is only valid under the condition $k^2 \gg \Delta k_m^2$ when the eigenmodes are dense enough [2]. For our microwave cavities in the semiclassical limit (the short-wavelength limit), this condition is valid. We choose a frequency window and take the frequency-dependent loss parameter determined from the experimental results. More details of determining the loss parameter are introduced in Sec. 4.1. Δk_m^2 is approximated by Weyl's formula in the limit of small wavelength compared to the system size. For a quasi-two-dimensional microwave cavity,

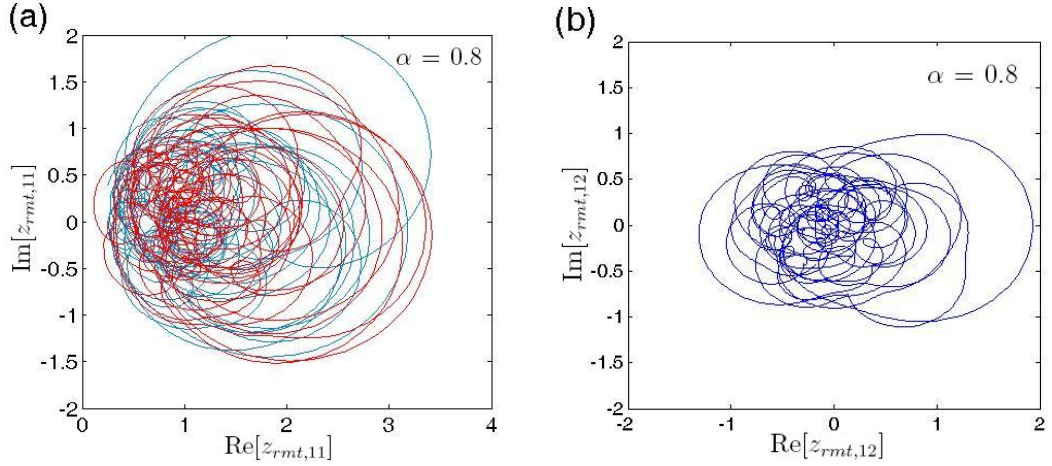


Figure A.2: Shown are (a) frequency-dependent $z_{rmt,11}$ (light blue) and $z_{rmt,22}$ (red) and (b) $z_{rmt,12}$ (blue) in the complex plane. The numerical results are generated as a single realization of the frequency window 9 – 11 GHz with the loss parameter $\alpha = 0.8$ and the two-dimensional cavity area $A = 0.112 \text{ m}^2$ using Eq. A.2.

$\Delta k_m^2 \simeq 4\pi/A$, where A is the area of the wave enclosure, and $\Delta k_m^2 \simeq 2\pi^2/(kV)$ for a three-dimensional cavity, where V is the volume of the wave enclosure [91]. The coupling W_{am} (or W_{bm}) is generated in the same way as a Gaussian random variable based on the random plane wave hypothesis. The normalized eigen-energy $k_m^2/\Delta k_m^2$ is generated the same way as $\lambda_m^{(rmt)}$ according to random matrix theory [2, 3].

For example, I generate a single realization of the frequency window 9 – 11 GHz of a quasi-two-dimensional ray-chaotic microwave cavity with the (constant) loss parameter $\alpha = 0.8$ and the two-dimensional cavity area $A = 0.112 \text{ m}^2$. The mean spacing of the eigen-energies Δk_m^2 is determined by the area. I use $M = 2000$

eigenmodes to compute the sum in Eq. A.2. The results are shown in Fig. A.2 as (a) $z_{rmt,11}$ (light blue) and $z_{rmt,22}$ (red) and (b) $z_{rmt,12}$ (blue) in the complex plane. The results from both Eq. A.1 and Eq. A.2 show the same statistics of $\underline{z_{rmt}}$ when the number of samples are large enough. However, instead of discrete and independent results from Eq. A.1, Eq. A.2 gives continuous results with frequency-dependent information and correlations.

A.1.2 Gaussian Unitary Ensemble Case

Both Eq. A.1 and Eq. A.2 use random matrix theory based on the Gaussian orthogonal ensemble (GOE) case. For time-reversal-invariance-broken systems, one should use the Gaussian unitary ensemble (GUE) to generate random matrices. Zheng *et al.* have also developed the numerical model of $\underline{\tilde{z}_{rmt}}$ for the GUE case [57, 58].

$$\tilde{z}_{rmt,a,b}(k) = \frac{-i}{\pi} \sum_{m=1}^M \frac{\tilde{W}_{am} \tilde{W}_{bm}^*}{\left(\frac{k^2 - k_m^2}{\Delta k_m^2}\right) - i\alpha}, \quad (\text{A.3})$$

where the random coupling \tilde{W}_{am} (or \tilde{W}_{bm}) for the GUE case is a “complex” random variable whose real part and imaginary part are independent Gaussian variables of zero mean and 1/2 variance. Note that the superscript * stands for the complex conjugate, and the average $\langle \tilde{W}_{am} \tilde{W}_{bm}^* \rangle = \delta_{ab}$. The other difference from the GOE case is about generating the energy eigenvalues $\tilde{\lambda}_m^{(rmt)}$ or $\tilde{k}_m^2 / \Delta k_m^2$. For the GUE case, these eigenvalues are computed from a big $M \times M$ random matrix (with $M > 1000$). For the matrix elements (H_{pq} , $1 \leq p \leq M$ and $1 \leq q \leq M$), (i) the diagonal elements (H_{pp}) are independent real Gaussian random variables of zero mean and unit vari-

ance; (ii) the upper-diagonal elements are independent complex random variables whose real part and imaginary part are independent real Gaussian variables of zero mean and $1/2$ variance; (iii) the lower-diagonal elements are complex-conjugates of the corresponding upper-diagonal elements ($H_{pq} = H_{qp}^*$). All other procedures of generating $\tilde{z}_{rmt,a,b}(k)$ are the same as in the GOE case.

A.2 Short Orbit Terms

In Sec. 2.2.2, we introduce the semiclassical approach to compute short-orbit terms in impedance, as the short-orbit correction matrix $\underline{\zeta}$ [39, 41]. For an N -port system, the (n, m) element of the $N \times N$ matrix $\underline{\zeta}$ is described by Eq. 2.10 as

$$\zeta_{n,m} = \sum_{b(n,m)} \left\{ -p_{b(n,m)} \sqrt{D_{b(n,m)}} \exp[-(ik + \kappa)L_{b(n,m)} - ikL_{port(n,m)} - i\beta_{b(n,m)}\pi] \right\}, \quad (\text{A.4})$$

where $b(n, m)$ is an index over all classical trajectories which leave the n^{th} port, bounce $\beta_{b(n,m)}$ times, and return to the m^{th} port. $p_{b(n,m)}$ is the survival probability of the trajectory due to the positions of the perturbing objects in the ensemble. The orbit stability factor $D_{b(n,m)}$ is a geometrical factor of the trajectory. k is the wave number, and κ is the effective attenuation parameter taking account of wave propagation loss. $L_{b(n,m)}$ is the length of the trajectory $b(n, m)$, and $L_{port(n,m)}$ is the port-dependent constant length between the n^{th} port and the m^{th} port.

In this section, we introduce our numerical algorithm for computing $p_{b(n,m)}$, $D_{b(n,m)}$, $L_{b(n,m)}$, and $\beta_{b(n,m)}$ of short orbits. For other parameters, more details of κ and $L_{port(n,m)}$ are introduced in Sec. 4.1. This algorithm was initially developed

by James Hart *et al.* for a two-dimensional billiard with N ports [4], and it has been further modified by Michael Johnson and Jen-Hao Yeh. For this algorithm, the billiard can have multiple straight segment or circular arc walls, and specular reflection of the walls can have reflection coefficient -1 for the metal walls or reflection coefficient 0 for walls covered by microwave absorbers.

A.2.1 Short-Orbit-Searching Algorithm

The first part of our numerical algorithm is to find short orbits. To use this algorithm, one first defines the boundary geometry of the two-dimensional billiard and inputs the locations of the source port (the n^{th} port) and the target port (the m^{th} port). Note that these two locations can be the same for the diagonal element $\zeta_{n,n}$. One also needs to set the maximum orbit length L_M . Then the algorithm launches trajectories from the source port over different angles θ_{so} , and it traces each of these trajectories bouncing in the billiard until: (i) it gets close enough to the target port (the distance from the trajectory to the target port less than d_{so}) or (ii) the length of the trajectory reaches L_M . If the algorithm finds one short orbit as in the case (i), it records the length (l_i) of each segment of the orbit between bounces and the reflection angle (θ_i) after each bounce. For example, Fig. A.3 illustrates a short orbit with two bounces and labels θ_{so} , d_{so} , l_1 , l_2 , l_3 , θ_1 , and θ_2 . The dashed circle centered at the target port has radius d_{so} .

There are two parameters to control the accuracy of this algorithm. One is the resolution of the scanning angles $\Delta\theta_{so}$ of the trajectories from the source port.

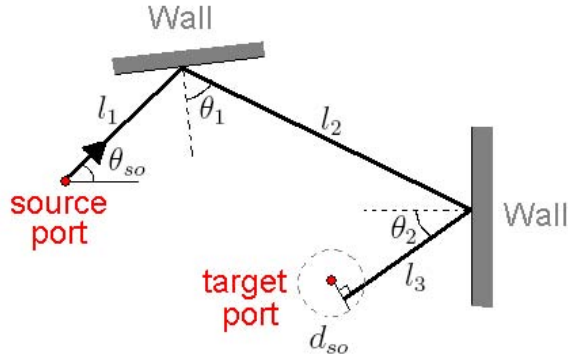


Figure A.3: A short orbit with two bounces. The red dots are the source port and the target port. The billiard walls (gray) are only shown near the bounces for illustration, and they can be straight segments or circular arcs.

A finer $\Delta\theta_{so}$ will reduce the chance of missing an orbit. The other parameter is the threshold distance d_{so} for determining arrival at the target port. A smaller d_{so} makes the results of this algorithm more correct. However, a small $\Delta\theta_{so}$ or a small d_{so} make the algorithm very time consuming. When the short orbits are not uniformly distributed in launch angle from the source, a lot of computation is wasted if one sets a small constant $\Delta\theta_{so}$. Therefore, this algorithm utilizes a port-crossing detection strategy and dynamically varies $\Delta\theta_{so}$ to save time and also preserve accuracy.

The port-crossing detection strategy is based on the intermediate value theorem and only works for a two-dimensional system. Considering two scanning trajectories next to each other from the source port at angles $\theta_{so,1}$ and $\theta_{so,2} = \theta_{so,1} + \Delta\theta_{so}$,

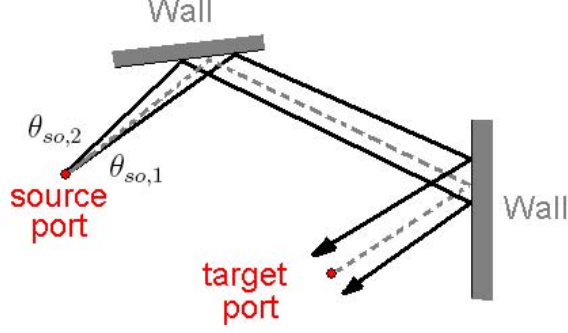


Figure A.4: An example of the port-crossing detection. The two solid lines are trajectories launching at angle $\theta_{so,1}$ and angle $\theta_{so,2}$, and the dashed line represent the true orbit between them.

the algorithm can record the two trajectories in each segment and determine if they pass the target port on the same side. Once the algorithm discovers the two trajectories passing the target port on different sides after a certain bounce, this means that there should be an orbit launched at the angle between $\theta_{so,1}$ and $\theta_{so,2}$ and it will hit right on the target port. We call this method “the port-crossing detection” and illustrate the idea in Fig. A.4, where the two solid lines are the two scanning trajectories, and the dashed line represents the true orbit.

Our algorithm starts with a larger scanning angle resolution $\Delta\theta_{so}^{(0)} = 2\pi/1000$, and once the port-crossing detection discovers the port-crossing situation, the algorithm utilizes a smaller resolution ($\Delta\theta_{so}^{(1)} = \Delta\theta_{so}^{(0)}/2$) to scan the angle region between $\theta_{so,1}$ and $\theta_{so,2}$. The algorithm recursively applies this angle refinement ($\Delta\theta_{so}^{(n)} = \Delta\theta_{so}^{(n-1)}/2$) until $\Delta\theta_{so}^{(n)} \leq 10^{-9}$. In addition to this port-crossing detec-

tion, in order to make sure that there is no short orbit missing, the algorithm utilizes half of its scanning angle resolution ($\Delta\theta_{so}^{(1)} = \Delta\theta_{so}^{(0)}/2$) to scan again and compares the results. If the result with the finer scanning resolution includes newly-discovered orbits, then the algorithm keeps utilizing a smaller scanning resolution ($\Delta\theta_{so}^{(n)} = \Delta\theta_{so}^{(n-1)}/2$) until the two results of $\Delta\theta_{so}$ and $\Delta\theta_{so}/2$ are the same. Note that the algorithm will ultimately stop since we have the threshold $\Delta\theta_{so}^{(n)} \leq 10^{-9}$, and there might still be missing orbits, especially for longer orbits.

Bo Xiao in our group is developing a new short-orbit algorithm based on this algorithm. His algorithm can record the wall of each bounce and use this information to eliminate the duplicate orbits. His algorithm also aims to generalize the short-orbit searching to three-dimensional systems. In this dissertation, I have not applied Xiao's algorithm.

A.2.2 Computing Parameters

Since the algorithm records every segment of an orbit, the parameters $p_{b(n,m)}$, $D_{b(n,m)}$, $L_{b(n,m)}$, and $\beta_{b(n,m)}$ can be computed. The number of bounces $\beta_{b(n,m)}$ is straightforward, and the orbit length $L_{b(n,m)}$ is the sum of all segment lengths. For the survival probability $p_{b(n,m)}$, one needs the position and shape/size of the perturbers in each realization, then one can determine that the orbit is blocked or not in each realization and compute the overall survival probability $p_{b(n,m)}$ of the orbit in all realizations.

The orbit stability factor $D_{b(n,m)}$ determines the contribution of an orbit to the

impedance. This parameter measures how the energy spreads out along the orbit in each segment [4, 150]. For example, if all the bounces are on straight segment walls, in the two-dimensional system the energy along the orbit spreads out as [150]

$$D_{b(n,m)} = \frac{2}{\pi k} \left(L_{b(n,m)} \right)^{-1}, \quad (\text{A.5})$$

where $L_{b(n,m)}$ is the orbit length, and k is the wave number. If there are bounces on circular arc walls, the algorithm can still compute $D_{b(n,m)}$ by considering the segment length (l_i), the incident angle (θ_i), and the radius of curvature (R_i) of the circular arc wall of each of these bounces, as

$$D_{b(n,m)} = \frac{2}{\pi k} \left| \left[L_{\beta_{b(n,m)}+1} \prod_{i=1}^{\beta_{b(n,m)}} \left(1 + \frac{2L_i}{R_i \cos(\theta_i)} \right) \right]^{-1} \right|, \quad (\text{A.6})$$

where L_i are effective lengths after bounces on circular arc walls, and they are recursively computed as [150]

$$\begin{aligned} L_1 &= l_1, \\ L_{i+1} &= l_{i+1} + L_i \left(1 + \frac{2L_i}{R_i \cos(\theta_i)} \right)^{-1}, \quad \text{for } 1 \leq i \leq \beta_{b(n,m)}. \end{aligned} \quad (\text{A.7})$$

Note that walls with positive radius of curvature [Fig. 1.1(c)] have a stronger dispersing effect (smaller $D_{b(n,m)}$) than walls with a negative radius of curvature [Fig. 1.1(b), (d), and (e)]. With all these parameters, the magnitude and the phase of each orbit term in Eq. A.4 can be determined.

Appendix B

Cryogenic Thru-Reflect-Line Calibration

In Chapter 3, I have introduced our three experimental systems, the 1/4-bowtie cavity, the superconducting cut-circle cavity, and the GigaBox. For each system, we use a vector network analyzer (VNA) through transmission lines to measure the scattering matrix of the wave scattering system. In order to measure the scattering matrix \underline{S} with high accuracy over a broad bandwidth, a broadband calibration method of microwave measurement is necessary. The calibration method removes the effect of the transmission lines connecting the vector network analyzer. For measurement at room temperature, we can utilize the electronic-calibration kit of a commercial VNA to conveniently calibrate the measured results. However, the convenient electronic-calibration kit does not function in a cryogenic environment, one must perform a manual calibration by utilizing known standards.

In this appendix, we introduce an improved microwave calibration method for use in a cryogenic environment, based on a traditional three-standard calibration, the Thru-Reflect-Line (TRL) calibration [108]. I review the Thru-Reflect-Line calibration in Sec. B.1 and introduce more details of this *in-situ* broadband cryogenic calibration system in Sec. B.2. With this *in-situ* calibration system, all calibration measurements are done in the same thermal cycle as the measurement of the cavity (requiring only an additional 20 minutes), thus avoiding 4 additional thermal cycles

for traditional TRL calibration (which would require an additional 12 days). In Sec. B.3, I further discuss the modified calibration method that takes advantage of additional information from multiple measurements of an ensemble of realizations of a superconducting cavity, as a new pseudo-Open standard, to correct errors in the TRL calibration. The experimental results of measuring a wave-chaotic microwave billiard shown in Sec. B.4 verify that the new method significantly improves the measured scattering matrix of a high-quality-factor superconducting cavity.

B.1 Thru-Reflect-Line Calibration

Microwave calibration is an important process to remove the systematic errors due to the transmission lines and connectors between the network analyzer and the device under test (DUT) as well as other systematic measurement errors. The calibration process utilizes measurements of known standards to move the reference plane of the measurement to the ports of the DUT [151, 152, 153]. A commonly-used calibration method for two-port measurement is the Thru-Reflect-Line (TRL) calibration [106, 107, 151].

The Thru-Reflect-Line calibration uses three standards to calibrate the effect of the two transmission lines connecting the two ports of the DUT to the VNA. I plot Fig. B.1 to illustrate the three standards in an anatomically-correct manner. For the Thru standard measurement, the two transmission lines are directly connected together; two identical reflectors, shown as the pink objects in Fig. B.1, are connected to the ends of the two transmission lines as the Reflect standard; an ad-

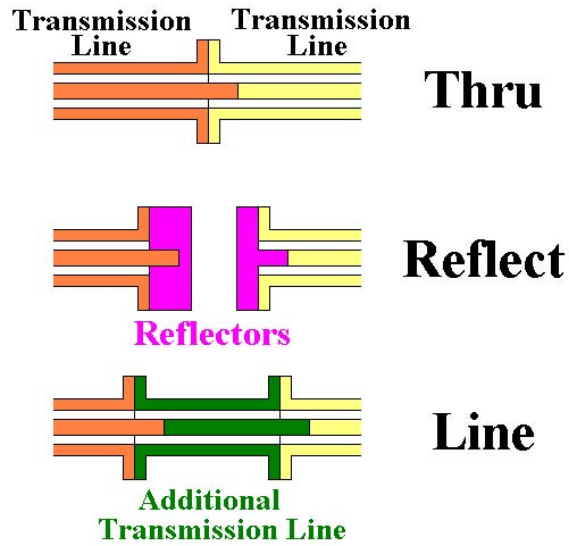


Figure B.1: Illustrations of the Thru, Reflect, and Line standards. The left transmission lines are terminated with a male connector, and the right transmission lines are terminated with a female connector. The Reflect standard consists of one male reflector and one female reflector. The Line standard is a transmission line with a male connector and a female connector in its two ends.

ditional electrically short (on the order of one guided wavelength) transmission line, shown as the green object in Fig. B.1, is added between the two transmission lines as the Line standard [107]. This TRL calibration method calibrates the transmission lines and brings the reference plane to the ends of the transmission lines for connecting to a DUT with one male connector and one female connector. The advantages of the TRL calibration are from two facts: (i) the use of redundant calibration standards reduces the uncertainty due to errors, such as connector irreproducibility, cable flexure, test-set drift, and noise, and (ii) the foundation of the calibration standard definitions depend solely on qualitative requirements (uniformity of the lines, identical cross-sections of the lines, and identical reflection coefficients of the Reflect standards) [154].

For applying TRL calibration in cryogenic systems, one challenge is that measuring multiple standards may involve cooling down and warming up of the system, changing the standard, and repeating the thermal cycle. These thermal cycles can be very time consuming and expensive. In addition, there is enhanced uncertainty of the reproducibility of experimental conditions in different thermal cycles [153, 154]. On the other hand, researchers have developed single-thermal-cycle calibration methods which use an on-wafer cryogenic probe station or electromechanical switches [108, 155, 156]. However, the problem of these single-thermal-cycle methods is that the differences between electrical paths in measurements of different standards, which are assumed to be equal, degrade the measurement accuracy and limit the frequency bandwidth [153].

For two-port systems, researchers have developed cryogenic TRL calibration

methods for measuring the 2×2 scattering matrix of a DUT. Laskar *et al.* [155] utilized the multiline method of the TRL and LRM (Line-Reflect-Match) calibrations introduced by Marks [107], to their cryogenic on-wafer probe station for noise and scattering-parameter measurements, and they emphasized the importance of providing a stable thermal environment [155]. Booth *et al.* also used a cryogenic probe station for scattering-parameter measurements of their coplanar waveguide (CPW) structures in high temperature superconductors [157, 158]. They applied a set of CPW calibration structures of TRL standards to characterize the errors in the network analyzer/probe station system [157], or alternatively three other standards: a Thru, a Reflect, and a series resistor [159]. Shemelin *et al.* used the TRL calibration for waveguides and coaxial cables to measure ferrites at low temperature [160]. In addition to the TRL calibration method, Jun *et al.* used a different calibration method by introducing a cryogenic dip probe for time-domain measurements of nanodevices [161].

Another way to achieve single-thermal-cycle TRL calibration is to utilize cryogenic microwave switches [162]. Ranzani *et al.* [156] have used cryogenic switches (coaxial subminiature latching switches) to switch the coaxial cables from the VNA to coaxial cables with different calibration standards, as well as the device under test. The electromechanical switches simply operate by means of brief electrical pulses to latch the switch to different positions, so no electrical signal is applied to the switch in its quiescent state. Due to the convenience of connecting the coaxial transmission lines to the ports of our superconducting cavity, we use cryogenic switches to develop the *in-situ* calibration system. Similar cryogenic switches have

been applied for calibrating measurement of superconducting quantum interference device (SQUID) amplifiers [163], measuring different superconducting qubit samples [164], or other experiments involving superconducting quantum computing [165].

Although the TRL calibration is less sensitive to the properties of the standards than other calibration method, such as the Open-Short-Load calibration [154], the TRL calibration is still limited by errors in its assumptions, such as irreproducibility of the transmission lines in each measurement, differences in the reflection coefficients of the two reflectors, and irreproducibility of the connector interface [154, 166]. Researchers have tried different methods to reduce the calibration errors, such as the development of precise dimensional characterization techniques for the transmission lines [167], the minimization of the possible center-conductor-gap variation [168], and modeling of the electrical properties combined with self-calibration approaches [154, 169]. In our cryogenic measurements, the temperature dependence of the scattering matrices of all transmission lines and imperfect TRL standards become additional sources of errors. These small errors are especially significant in our extremely-low loss system because the calibrated $|S_{11}|$ and $|S_{22}|$ are very close to 1 while the frequency is away from the resonance frequencies.

B.2 *In-situ* Broadband Cryogenic Calibration System

Figure B.2 shows the setup of our *in-situ* broadband cryogenic calibration system. The term “*in-situ*” means the TRL calibration process can be applied at low temperatures without spending a great deal of time changing standards. Here

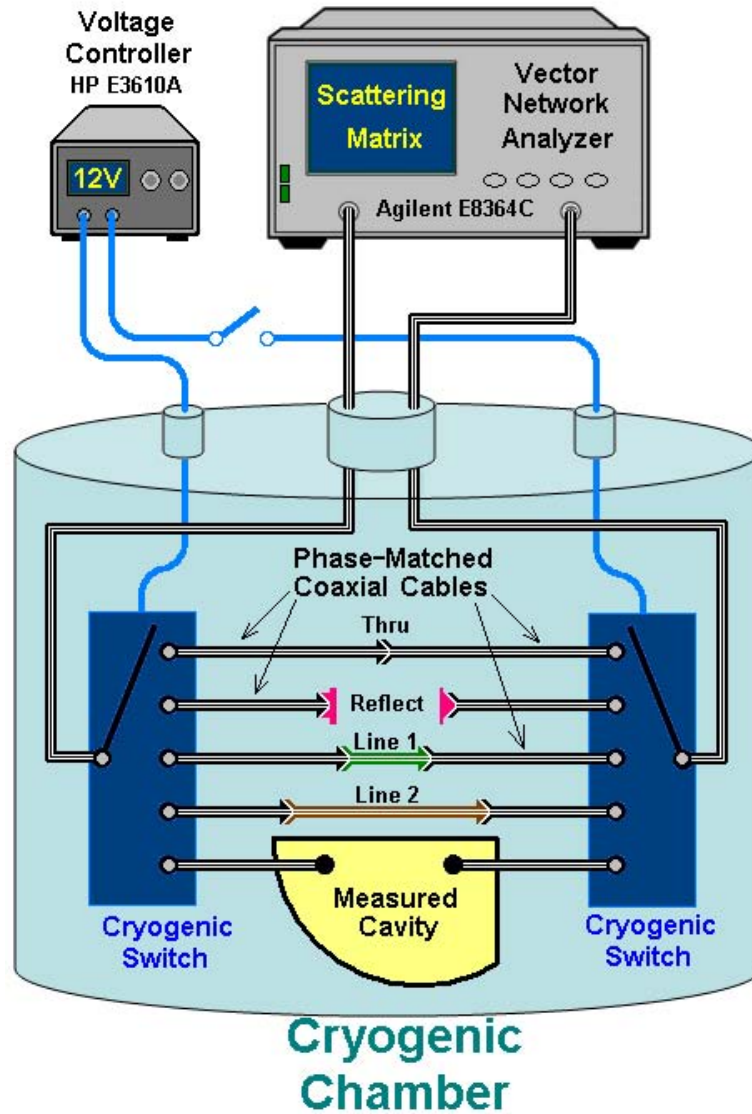


Figure B.2: Schematic experimental setup of the *in-situ* broadband cryogenic calibration system. The five pairs of phase-matched coaxial cables have nearly identical length and are not shown to scale. For the phase-matched coaxial cables and TRL standards, the male (or female) connectors are illustrated. The microwave cavity has a female connector and a male connector for its two ports, respectively.

we utilize two cryogenic 6-position switches (Radiall coaxial subminiature latching switches R591722605) to include one Thru, one Reflect, and two Line standards together with the cavity under measurement. Figure B.3 shows the cryogenic switches [170] (left) and the copper clamp (right) used to mount and thermally anchor the cryogenic switches on the cold plate (see photographs in Fig. B.4). The pink arrow in Fig. B.3 points the position for tightening the clamp by a screw. Each switch connects the transmission line from the VNA through the center connector (see the left plot of Fig. B.3) to the outer connectors which are connected to different standards, or to the cavity, by RF COAX phase-matched (13 inch long between interfaces, electrical length deviations < 1 ps) SMA coaxial cables (S086MMHF-013-1). These cables have male SMA (subminiature version A) microwave connectors in the both ends. Therefore, for the Thru standard, we connect a pair of the coaxial cables with a female-female adapter (Mini-Circuits adapter SF-SF50+). In order to make sure the electrical paths are as identical as possible, the same type of industrially-assembled cables, and adapters, have been used for the other 4 pairs of transmission lines. In future experiments, we plan to replace half of the phase-matched coaxial cables by cables terminated with one male connector and one female connector. In this way we will not need the female-female adapters and can reduce the number of connectors in each electrical path, so the number of error sources can also be reduced. For the Reflect standard, we use two short circuits, one with a male connector and the other with a female connector (Fairview Microwave models SC2136 and SC2141), to terminate the pair of coaxial cables. For the two Line standards, we add two different SMA male-to-female adapters of electrical length 1.94 cm and

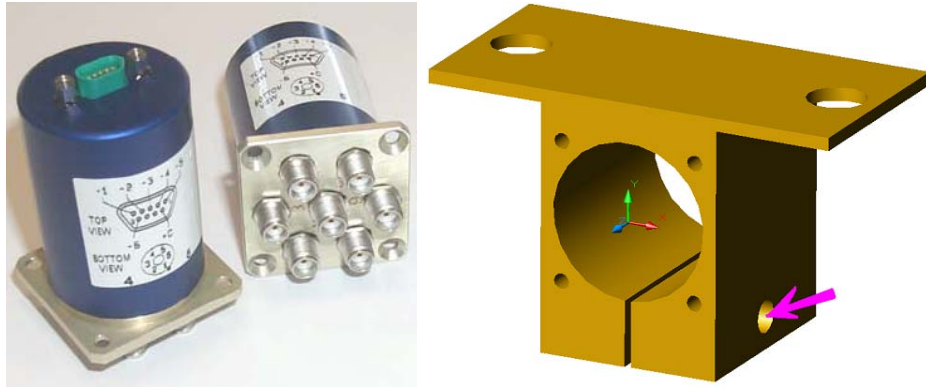


Figure B.3: Left: The Radiall cryogenic switches R591722605. Right: The copper clamp to mount the cryogenic switches on the cold plate. The pink arrow points the position for tightening the clamp by a screw.

2.56 cm (Fairview Microwave models SM4971 and SM5291) to connect the two pairs of coaxial cables, respectively. All of these standards and the cut-circle cavity are at a uniform temperature in the cryostat, and the switches are controlled by voltage pulses from a DC power supply (Hewlett-Packard E3610A) outside the cryostat. The network analyzer is an Agilent Technologies E8364C.

One advantage of using cryogenic switches is to save a great deal of time for the TRL calibration. One full thermal cycle of this cryostat takes about 3 days, so a multiple-thermal-cycle TRL calibration for 4 standards would require an additional 12 days for calibration. However, with the *in-situ* calibration system, we only need an additional 20 minutes for measuring the 4 standards within the same thermal cycle for measuring the superconducting cavity. The cryogenic switches also make the calibration process conveniently accessible each time the system environment is



Figure B.4: Left: The front of the cryogenic switch in the copper clamp. The coaxial cable in the center is connected to the network analyzer. The other coaxial cables around the center one are connected to the microwave cavity and TRL standards. Right: The back of the cryogenic switch in the copper clamp. The black and red wires are connected to the voltage controller to control the state of the switch.

modified, for example, by changing the temperature, microwave power, or external magnetic field. We can adjust the equilibrium temperature of the cavity and standards by tuning the applied DC current to heating resistors installed in the cryostat. The applied microwave power can be controlled by the network analyzer. In addition to increasing the efficiency of the experiment, avoiding opening/closing the chamber for changing standards also reduces the uncertainties created by having different temperatures or different layouts of transmission lines in each measurement.

On the other hand, the disadvantage of using cryogenic switches is that the switches utilize 5 different pairs of transmission lines to connect to the standards or the cavity. The differences of the scattering matrices of these electrical paths are additional errors of the TRL calibration. We have measured the differences at room temperature, and the deviations from the switches are $|\Delta S| < 0.01$; the deviations from the transmission lines are $|\Delta S| < 0.06$. These errors can be reduced from the calibrated results by the pseudo-Open standard, which I will introduce in the following section.

The calibration system is also broadband because we install two Line standards. The TRL calibration is invalid for frequencies where the phase difference between the Thru standard and the Line standard is too small (the phase difference should be greater than 20 degrees and less than 160 degrees)[107, 151]. To solve this problem, one can use two Line standards with different lengths and make sure that the problematic frequency bands do not overlap. In our experiment, one Line standard has problematic frequency bands near 7.7 GHz and 15.3 GHz; the other Line standard has problematic frequency bands near 5.9 GHz, 11.8 GHz, and

17.6 GHz. Therefore, we use the cryogenic switches connected with two different Line standards to achieve broadband calibration, for example, we can measure the scattering matrix continuously from 3 to 18 GHz.

We use MATLAB to operate the TRL calibration according to Rytting's algorithm [171], and we combine the *good* frequency bands from the two Line standards to create a broadband result. We then use the pseudo-Open standard to remove the remaining errors in the TRL-calibrated data. One example of the result after these procedures is shown in Fig. B.5 as the $|S_{11}|$ and $|S_{21}|$ of a single realization from 3 to 18 GHz. We can see the resonance density increase with frequency. In low frequency regions, the resonances are sharp and well-separated, and $|S_{11}|$ is close to 1 in the frequencies away from the resonant frequencies. In high frequency regions, the resonance density increases, and the resonances start to overlap with each other. For example, we do not see the off-resonance background close to 1 in $|S_{11}|$ near 18 GHz.

B.3 Pseudo-Open Standard

The scattering matrices calibrated by the TRL method ($\underline{S_{TRL}}$) still have many errors due to the fact that the practical standards and coaxial cables do not perfectly satisfy the assumptions of the TRL calibration. The remaining issues are: (1) the irreproducibility of the transmission lines and connectors in each electrical path, (2) the difference between the two reflectors in the Reflect standard, and (3) the impedance-mismatch and the imperfection of the Thru and Line standards. These

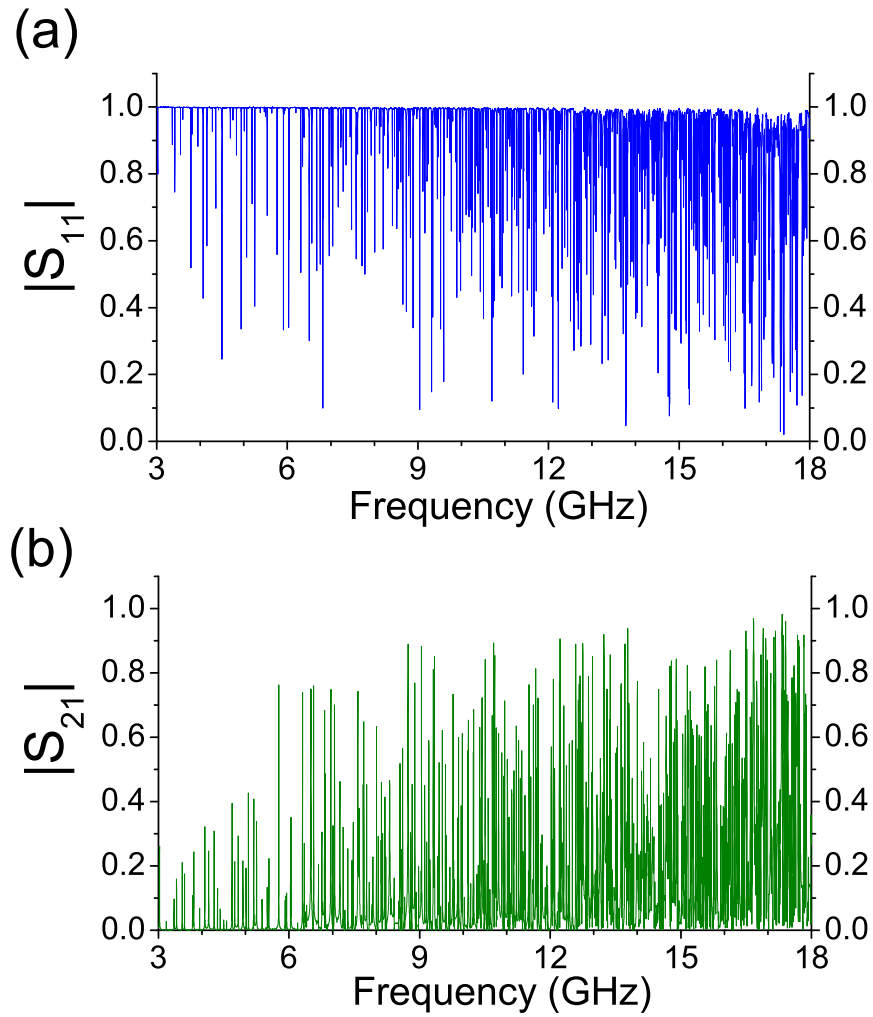


Figure B.5: The magnitude of (a) $|S_{11}|$ and (b) $|S_{21}|$ with high-quality-factor resonances from 3 to 18 GHz of a single realization of the superconducting cut-circle cavity in the *in-situ* cryogenic calibration system. The data have been calibrated with the TRL calibration and corrected by the pseudo-Open method.

errors are especially critical when $|S_{11}|$ and $|S_{22}|$ of the measured cavity are close to 1. In our case, while the frequency is away from the resonant frequencies of the superconducting cavity, $|S_{11}|$ and $|S_{22}|$ are very close to 1 (i.e. the transmission coefficient $|S_{21}|$ is very close to 0, and there is almost no absorption in the cavity) in the extremely low loss environment. Therefore, a small error can make $|S_{11}|$ or $|S_{22}|$ larger than 1 and cause non-physical results. This small error is also critical for analysis of the 2×2 impedance matrix $\underline{\underline{Z}}$, obtained by a bilinear transformation as $\underline{\underline{Z}} = \underline{\underline{Z}}_0^{1/2}(\underline{\underline{1}} + \underline{\underline{S}})(\underline{\underline{1}} - \underline{\underline{S}})^{-1}\underline{\underline{Z}}_0^{1/2}$, where $\underline{\underline{Z}}_0$ is the diagonal characteristic impedance matrix of the transmission lines (50Ω). The denominator $(\underline{\underline{1}} - \underline{\underline{S}})$ makes the impedance matrix sensitive to this small error when S_{11} or S_{22} are close to 1.

Figure B.6 shows two examples of the raw measured data (without calibration) of the magnitude of the scattering matrix elements versus frequency for the superconducting cut-circle microwave cavity at 6.6 K. Because the loss parameter in the superconducting cavity is very low ($\alpha \ll 1$, i.e. high Q), the curves of $|S_{raw,11}|$ and $|S_{raw,21}|$ show sharp and well-separated resonances on a smoothly varying background. Note that all degeneracies are broken in wave-chaotic billiards, which means the resonances occur at different frequencies [11]. The background feature shows the influence of the transmission lines between the cavity and the network analyzer, and this is what we want to remove by calibration. With the cryogenic TRL calibration, we can eliminate most of the influence from the transmission lines. One example of the TRL-calibrated result $|S_{TRL,11}|$ of a single realization is shown as the black curve in Fig. B.7. As we expect for a superconducting cavity, now $|S_{TRL,11}|$ is close to 1 at frequencies away from the resonant frequencies. However, there are still small vari-

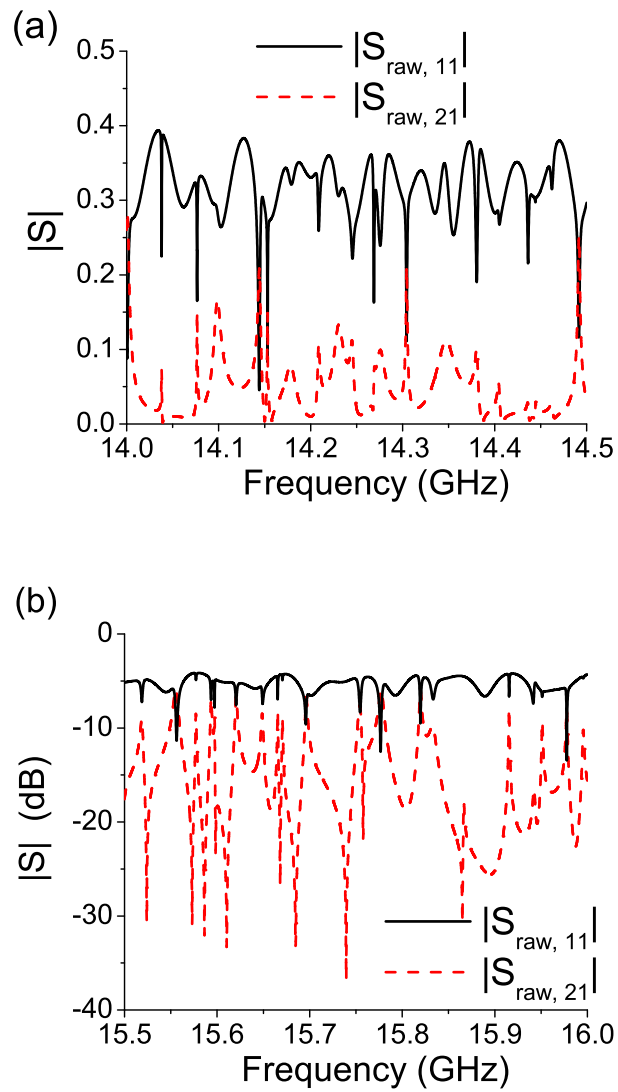


Figure B.6: The magnitude of raw measured scattering matrix element $S_{raw,11}$ (black solid curves) and $S_{raw,21}$ (red dash curves) versus frequency. (a) An example with the frequency band from 14.0 to 14.5 GHz plotted in linear scale; (b) another example with the frequency band from 15.5 to 16.0 GHz plotted in semi-logarithmic scale.

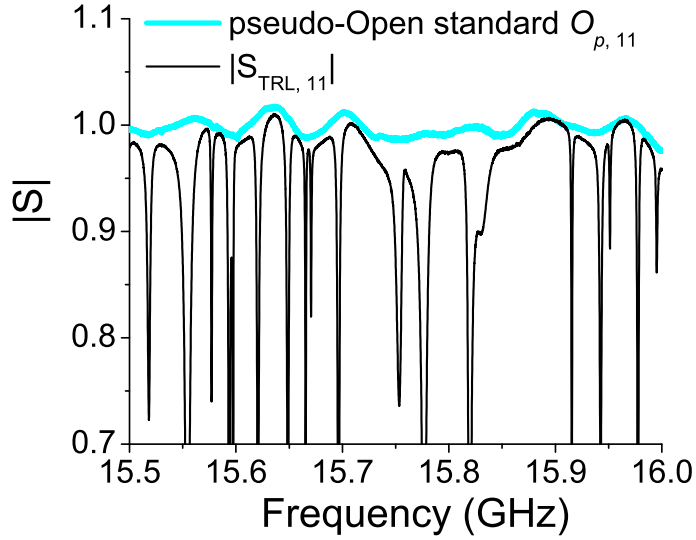


Figure B.7: The magnitude of TRL-calibrated $S_{TRL,11}$ (the black curve) and the pseudo-Open standard (the thicker light-blue curve) versus frequency.

ations in the background due to the systematic errors of the TRL calibration. Note that at some frequencies (e.g. near 15.64 GHz), the small error makes $|S_{TRL,11}| > 1$.

To solve this problem, we introduce the pseudo-Open standard by taking advantage of the multiple measurements of the 72 ensemble realizations of the cavity. In each realization, we only change the orientation of the Teflon perturber (see the blue object in Fig. B.8), and all of the other features, including the transmission lines, cavity volume, coupling, etc., remain the same. Therefore, by comparing the TRL-calibrated data of the 72 realizations, we see a systematically-varying

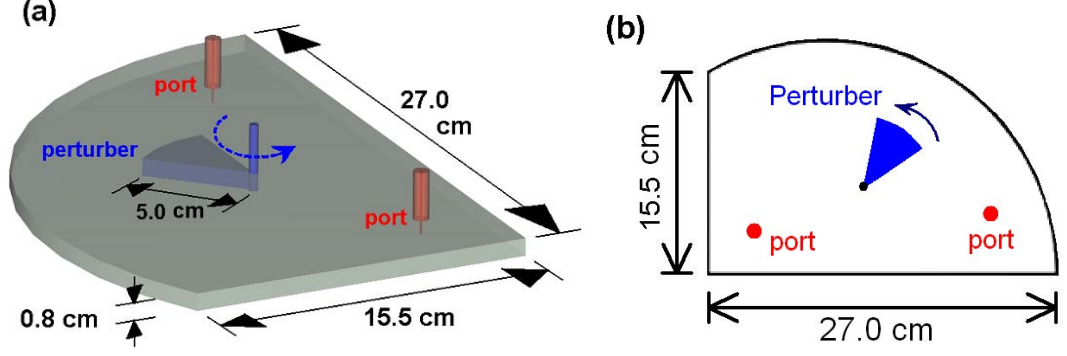


Figure B.8: (a) The quasi-two-dimensional cut-circle microwave cavity in a three-dimensional perspective, showing the cavity dimensions, ports, and the perturber. (b) Projected two-dimensional view of the cut-circle billiard.

background in the scattering matrices in all realizations, but the narrow and well-separated resonances move to various frequencies. For illustration, Fig. B.9 shows the quantity $(|S_{TRL,11}|^2 + |S_{TRL,21}|^2)^{1/2}$ in 12 realizations (each for a perturber orientation 30° apart). Note that the resonances occur at varied frequencies in different realizations, but the off-resonance regions form a systematically-varying background.

We note that $\Sigma_1 \equiv (|S_{TRL,11}|^2 + |S_{TRL,21}|^2)^{1/2}$ and $\Sigma_2 \equiv (|S_{TRL,22}|^2 + |S_{TRL,12}|^2)^{1/2}$ are unity in a lossless system. For a very low loss system, RMT predicts that the Σ_1 and Σ_2 of an ensemble of realizations have statistical distributions [21] where most of the samples are close to 1. If the cavity is weakly coupled through the ports to outside (i.e. $|S_{21}|$ and $|S_{12}|$ are closer to 0; $|S_{11}|$ and $|S_{22}|$ are closer to 1), the distributions show that the samples of Σ_1 or Σ_2 are even closer to 1. Therefore, if

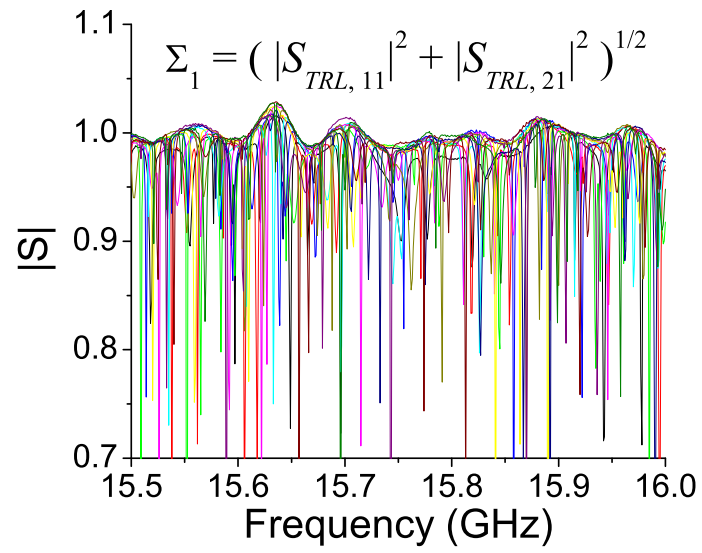


Figure B.9: Shown are 12 examples of different realizations of $\Sigma_1 = (|S_{TRL,11}|^2 + |S_{TRL,21}|^2)^{1/2}$ versus frequency in varied colors.

one takes the maximum of many realizations of Σ_1 or Σ_2 under these conditions, it should be very close to 1.

We have constructed a numerical model to analyze the systematically-varying background. We use RMT and the RCM to numerically generate multiple-realization data to represent a superconducting cavity, and the maxima of Σ_1 or Σ_2 over the realization ensemble are very close to 1 for every frequency. However, if we combine these numerical cavity data with the measured data of our TRL standards and coaxial cables, and carrying out the same TRL calibration, we see a similar systematically-varying background. Therefore, this frequency-dependent feature represents a combination of all errors of the TRL calibration. According to our numerical test, the major error in our experiment is from the Line standards, and it can cause errors for S_{11} and S_{22} of $|\Delta S| < 0.1$ and an error for S_{21} of $|\Delta S| < 0.04$. The errors from the Thru standard and the Reflect standard are all smaller by a factor of 2 to 3.

In order to utilize this feature, we take the maximum values of Σ_1 and Σ_2 of the experimental data over the 72 realizations, and we define a frequency-dependent diagonal matrix $\underline{\underline{O_p}}$, where $O_{p,11}$ (or $O_{p,22}$) is the maximum of Σ_1 (or Σ_2) over the 72 realizations. In a very low loss system or a weakly coupled system, $\underline{\underline{O_p}}$ should be close to the identity matrix if the TRL calibration has no error. Thus, the frequency-dependent variations of $\underline{\underline{O_p}}$ represent the remaining errors in the experimental data after the TRL calibration. We call $\underline{\underline{O_p}}$ the pseudo-Open standard because $\underline{\underline{O_p}}$ is like an Open standard when we exclude all resonances (i.e. no energy is transmitted through the two ports). Figure B.7 shows the pseudo-Open standard response $O_{p,11}$

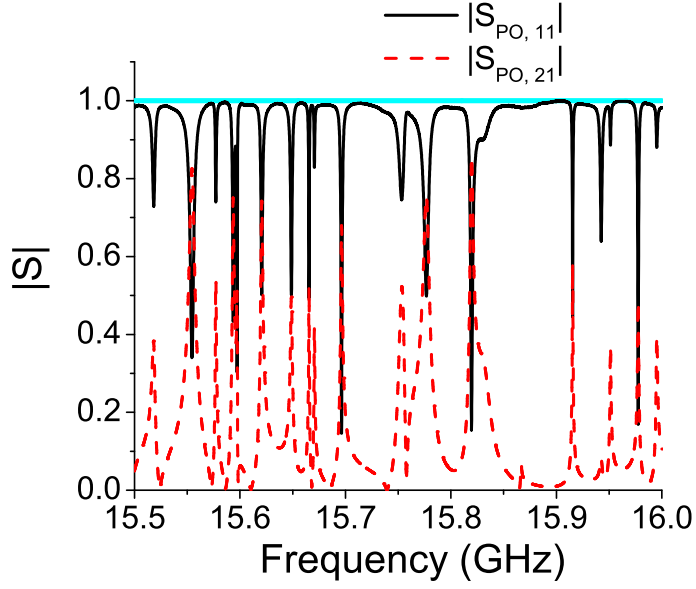


Figure B.10: The magnitude of TRL-calibrated and pseudo-Open-corrected $S_{PO,11}$ (the black solid curve) and $S_{PO,21}$ (the red dash curve) versus frequency. The horizontal blue line shows $|S| = 1$.

as the thicker light-blue curve. By utilizing the information from multiple measurements of the cavity in different realizations, the pseudo-Open standard helps to calibrate out the errors due to the deviations between the transmission lines connected to the TRL standards and the transmission lines connected to the cavity.

We simply remove the errors and obtain a TRL-calibrated and pseudo-Open-corrected scattering matrix $\underline{\underline{S_{PO}}}$ by

$$\underline{\underline{S_{PO}}} = \underline{\underline{S_{TRL}}} \underline{\underline{O_p}}^{-1}. \quad (\text{B.1})$$

Figure B.10 shows the result of the pseudo-Open correction. The small systematic

variations in the TRL-calibrated data $|S_{TRL,11}|$ is removed after applying the pseudo-Open standard. Therefore, by using the TRL calibration with the pseudo-Open standard, we can have well-calibrated data of the scattering matrix, and we are able to do further analysis of the statistics of the scattering matrices or the impedance matrices for wave chaos research [41, 61].

We also use our numerical model to test how the pseudo-Open method resolves the errors from the TRL calibration. Since the pseudo-Open standard is based on the maximum values of $(|S_{TRL,11}|^2 + |S_{TRL,21}|^2)^{1/2}$ and $(|S_{TRL,22}|^2 + |S_{TRL,12}|^2)^{1/2}$, it contains no information about the phase of the elements of the scattering matrix. Therefore, it can only correct the magnitude of the scattering matrix, and the improvement is better when $|S_{11}|$ and $|S_{22}|$ are closer to 1. Other limitations concern determination of the maxima of $(|S_{TRL,11}|^2 + |S_{TRL,21}|^2)^{1/2}$ and $(|S_{TRL,22}|^2 + |S_{TRL,12}|^2)^{1/2}$. In order to get a sampled maximum value close to the true maximum value, one needs to have a very low loss system or a weakly coupled system, or one needs to have a large number of realizations. Our experiment satisfies these requirements for the pseudo-Open standard, and according to the numerical test, the pseudo-Open method can remove the errors of the TRL calibration as measured by the statistical distributions of the magnitudes of the scattering matrix.

B.4 Test of RMT Predictions

With the well-calibrated data of the scattering matrix, we can now apply the extended random coupling model [41, 61] to remove the system-specific features

of the scattering matrix and reveal the universal statistics which are predicted by random matrix theory [21, 61]. Figure B.11 shows a comparison of the universal statistics predicted by RMT (thicker light-blue curves) and the experimental data which are calibrated with cryogenic TRL calibration only (red dash curves) and also with pseudo-Open correction (black curves) in terms of the distributions of the RCM-normalized $|S_{11}|$ and $|S_{21}|$. The probability density functions (PDFs) of the experimental data are taken from all 72 realizations and in frequency from 14.0 to 16.0 GHz. The RMT predictions are the best-matched PDFs with a single parameter (the loss parameter α), and $\alpha = 0.02$ is the fit value. The results show that the pseudo-Open correction makes significant improvement in the PDFs when $|S_{11}|$ or $|S_{21}|$ are close to 1. The non-physical features ($|S| > 1$, seen in the TRL calibrated data in Fig. B.7) are almost entirely eliminated with the correction of the pseudo-Open standard. The PDFs of the experimental data are not as smooth as the theoretical PDFs because we generate many more numerical samples to plot the theoretical curves. One can generalize these results to other resonant systems in which the modes can be perturbed by external means, such as strain, electric field, temperature, magnetic field, etc, to generate an ensemble of multiple measurements for the pseudo-Open method.

B.5 Conclusion

Applying the extended random coupling model for a multiple-port wave scattering system requires measurement of the whole impedance matrix $\underline{\underline{Z}}$ of the system,

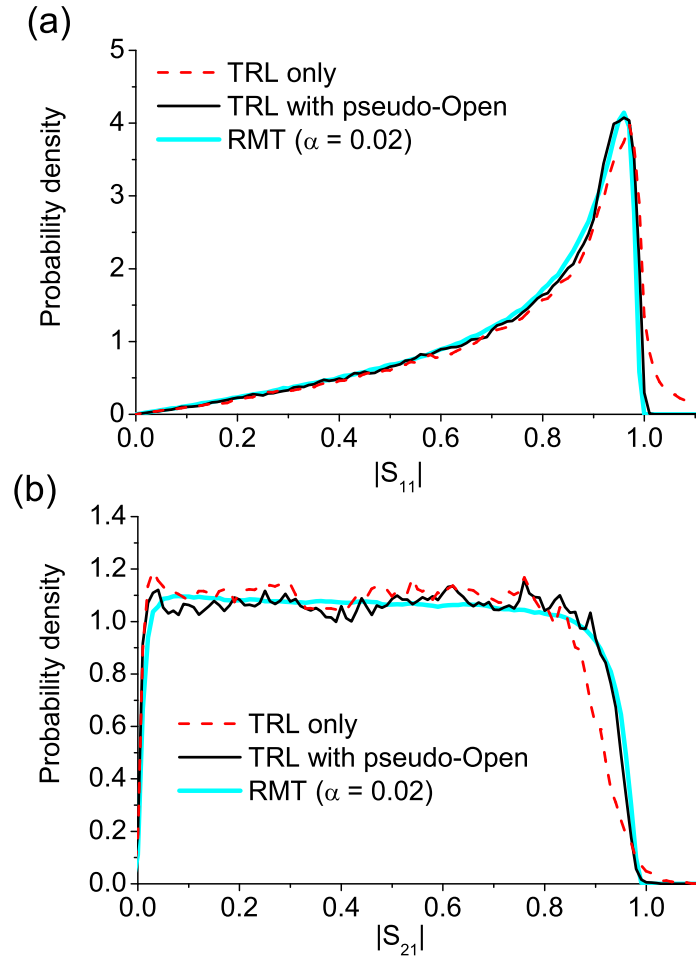


Figure B.11: The probability density of (a) $|S_{11}|$ and (b) $|S_{21}|$ of the RMT predictions (thicker light-blue curves), the experimental data from the superconducting cut-circle cavity at 6.6 K with TRL-calibration (red dash curves), and the data with TRL-calibration and pseudo-Open correction (black curves).

and therefore well-calibrated measurement of the scattering matrix \underline{S} is important. In this appendix we demonstrate the details of our *in-situ* broadband cryogenic calibration system where the calibration process is made dramatically more convenient by installing two cryogenic switches for single-thermal-cycle TRL calibration. We also introduce a pseudo-Open standard by taking advantage of the ensemble realizations of the superconducting cavity with a movable perturber and the feature of well-separated resonances in an extremely low loss environment. Experimental data verify that the pseudo-Open standard can significantly improve the TRL-calibrated data. We have shown that the well-calibrated scattering matrices are beneficial for wave chaos research in Fig. B.11. In addition to this application, this calibration method should broadly benefit various applications related to high-precision cryogenic measurement.

Appendix C

Error Analysis of Short-Orbit Correction

In Chapter 4, I have introduced experimental verification of the effect of short orbits in the measured impedance of a wave scattering system, the 1/4-bowtie cavity. We utilize microwave absorbers to cover specific walls in the metal cavity, and therefore we can examine the effect of individual orbits in Sec. 4.1. The results in Sec. 4.1 can be further analyzed in the length domain, and it can help to figure out the major sources of error in the experiment.

We propose that there are two major sources of the deviations between the theoretical results and the experimental results shown in Fig. 4.1. The first is that the microwave absorbers do not fully suppress the effect of orbits; the second arises from the ends of microwave absorbers that scatter energy back to the ports. To verify this, we transform the frequency-dependent impedance corrections data $z_{cor,n,m}(f)$ in Fig. 4.1 to the time domain (t) by the inverse Fourier transform and then multiply the time by the speed of light c to the length domain $l = ct$. The results are shown in Fig. C.1 as $\varepsilon_{data}(l) \equiv |\text{IFT}\{z_{cor,n,m}\}|$ and $\varepsilon_{theo}(l) \equiv |\text{IFT}\{\zeta_{n,m}^{(LM)}\}|$, where $\text{IFT}\{\cdot\}$ is the inverse Fourier transform ($f \rightarrow t = l/c$). Note that the frequency range of the inverse Fourier transformation is from 6 to 18 GHz, and therefore the resolution in length is 2.5 cm. Figs. C.1 (a) and (b) are the one-port cases, and the shown data are $z_{cor,11}$; Figs. C.1 (c) and (d) are the two-port cases, and the shown data

are $z_{cor,12}$.

In the length domain, the major peaks of the measured data $\varepsilon_{data}(l)$ (red) match the peaks of the theoretical prediction $\varepsilon_{theo}(l)$ (blue and dashed), and this verifies that the short-orbit correction can describe the major features of the measured impedance in the wave scattering system. For example, the matched peak in the theory curve and the data curve in Fig. C.1(a) corresponds to the short orbit from the port to wall B and returning, shown as the red (vertical) line in the inset of C.1(a). However, there are several minor peaks in the measured data not present in the theoretical curves. After further examination of the geometry, the positions of these deviations in Fig. C.1 match the lengths of orbits which are related to the ends of the microwave absorbers, or bounce off the microwave absorbers with a large incident angle. When the microwave absorbers end at the corners, they produce gaps and edges, and these defects create weak diffractive short orbits. For example, the green lines E1 and E2 in the insets in Figs. C.1(a) and (b), E2 and E3 in Fig. C.1(c), and E2 in Fig. C.1(d) represent the diffractive short orbits which leave a port, bounce off the edge of the microwave absorber, and return to a port. Their path lengths match the deviations between the measured data and the theory as labeled in the figure. Furthermore, the blue line E3 in the inset in Fig. C.1(b) represents the short orbit produced by the edge and bounced from one wall.

The other error source is imperfection of the microwave absorbers that reflect ~ -20 dB of the incident signal for normal incidence, and more for oblique incidence. Therefore, the short orbits shown as purple lines E1 in Figs. C.1(c) and (d) with a large incident angle bring about deviations between the theory and experimental

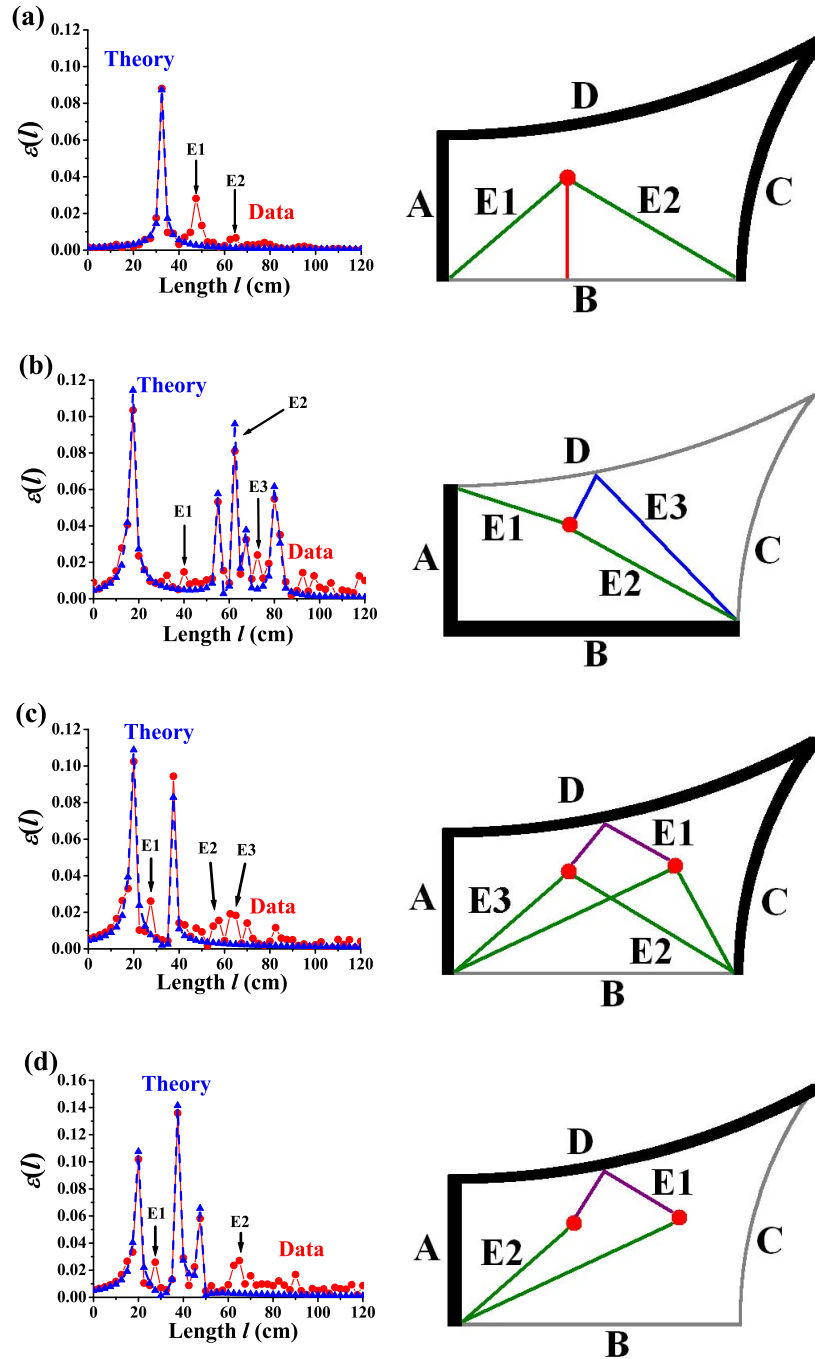


Figure C.1: Four examples of the magnitudes of the impedance correction in the length domain $\varepsilon(l)$. The insets are the corresponding geometry of the labeled orbits and the corresponding error sources. The thick black lines correspond to walls coated with microwave absorber.

data. These sources of error due to the ends of absorbers or large incident angles on absorbers were not included in the short-orbit correction. However, these microwave-absorber-related errors will not concern us further in the experiments where all microwave absorbers are removed. Therefore, the experiments in Secs. 4.2, 4.3, and 4.4 are free from these errors.

In addition to the errors discussed above, another source of error is the difficulty in reproducing the antenna geometry with each measurement as the cavity is opened and re-sealed between the measurement of the radiation impedance and exposed wall cases. This error remains in the experiments where the radiation impedance matrix $\underline{\underline{Z_{rad}}}$ is used. Another concern is multiply-reflected trajectories that bounce off of the antennas. However, because we describe trajectories in terms of the impedance instead of the scattering matrix, the multiply-reflected trajectories are incorporated in a single impedance term. This is an important advantage of using impedance because it can take account of the multiple-reflected trajectories in a simple compact form.

Appendix D

Fading Model in the High Loss Regime

Fading is the time-dependent variations in signal strength measured at a receiver, due to temporally evolving multipath scattering and interference. In Chapter 5, we have introduced a statistical fading model for the time-reversal-invariant (TRI) case and the time-reversal-invariance-broken (TRIB) case by applying the random coupling model (RCM) to combine the predictions of random matrix theory (RMT) and the system-specific features of a practical system. In the high-loss limit this RMT fading model reduced to the most common fading models (the Rayleigh fading model and the Rice fading model) in the wireless communication field. In this appendix we discuss the derivations of the RMT model in the high-loss limit in more detail.

To model the fading amplitude, we use the scattering matrix \underline{S} that describes a linear relationship between the input and the output voltage waves on a network. We consider the 2×2 \underline{S} matrix, where the two ports of the network system correspond to the transmitter and the receiver. The complicated wave scattering system is modeled by the scattering matrix, and therefore the magnitude of the matrix element $|S_{21}|$ corresponds to the fading amplitude. To apply the random matrix approach, we start with an RMT description of the 2×2 scattering matrix \underline{s}_{rmt} of a wave chaotic system, based on Brouwer and Beenakker's work [21]. This scattering matrix \underline{s}_{rmt}

does not contain any system-specific information and is totally ergodic. The RMT form of the scattering matrix can be written as [21]

$$\underline{\underline{s}}_{rmt} = \underline{\underline{U}}_1 \begin{bmatrix} \sqrt{1-T_1} & 0 \\ 0 & \sqrt{1-T_2} \end{bmatrix} \underline{\underline{U}}_2. \quad (\text{D.1})$$

In this equation $\underline{\underline{U}}_1$ and $\underline{\underline{U}}_2$ are two 2×2 random unitary matrices that can be written in the form [172],

$$\underline{\underline{U}} = e^{i\beta} \begin{bmatrix} \cos \theta e^{i\psi} & \sin \theta e^{i\varphi} \\ -\sin \theta e^{-i\varphi} & \cos \theta e^{-i\psi} \end{bmatrix}, \quad (\text{D.2})$$

where β , ψ , and φ are independent random variables uniformly distributing from 0 to 2π , and $\theta = \arcsin(\sqrt{\xi})$, where ξ is a random variable uniformly distributing from 0 to 1. T_1 and T_2 are the absorption probabilities which govern the strength of the absorption of the system [21]. For $T_1, T_2 \rightarrow 0$, the matrix $\underline{\underline{s}}_{rmt}$ is unitary, and there is no absorption (lossless). Whereas for $T_1, T_2 \rightarrow 1$, the matrix $\underline{\underline{s}}_{rmt}$ vanishes, and the loss parameter is $\alpha \rightarrow \infty$. T_1 and T_2 are random variables, and their joint distributions for the TRI case and the TRIB case will be discussed in the following sections.

D.1 Time-Reversal-Invariant Case

In the TRI case, $\underline{\underline{U}}_2$ is the transpose of $\underline{\underline{U}}_1$ ($\underline{\underline{U}}_2 = \underline{\underline{U}}_1^T$) [21]. Also, the absorption probabilities T_1 and T_2 in Eq. (D.1) are two random variables ($0 \leq T_1 \leq 1$ and $0 \leq T_2 \leq 1$) whose joint distribution function depends on a scalar parameter γ ,

referred to as the “dephasing rate” [21],

$$\begin{aligned}
P(T_1, T_2; \gamma) = & \frac{1}{8} \frac{|T_1 - T_2|}{T_1^4 T_2^4} \exp \left[-\frac{\gamma}{2} \left(\frac{1}{T_1} + \frac{1}{T_2} \right) \right] [\gamma^2 (2 - 2e^\gamma + \gamma + \gamma e^\gamma) \\
& - \gamma (T_1 + T_2) (6 - 6e^\gamma + 4\gamma + 2\gamma e^\gamma + \gamma^2) \\
& + T_1 T_2 (24 - 24e^\gamma + 18\gamma + 6\gamma e^\gamma + 6\gamma^2 + \gamma^3)].
\end{aligned} \tag{D.3}$$

From Eq. (D.1) and (D.2), the fluctuating fading amplitude is

$$|s_{rmt,21}| = \sqrt{\xi(1-\xi) \left[2 - T_1 - T_2 - 2 \cos \phi \sqrt{(1-T_1)(1-T_2)} \right]}, \tag{D.4}$$

where $\phi = 2(\psi - \varphi)$. Hemmady et al. [90] found that the dephasing rate γ in Eq. (D.3) can be related to the loss parameter α of the corresponding closed system as $\gamma = 4\pi\alpha$. For an open fading system, we consider an equivalent closed system in which uniform absorption accounts for wave energy lost from the system, and we assume that we can define an equivalent loss parameter α for the open system.

From Eq. (D.4) we can tune the loss parameter α , which determines the joint distribution function $P(T_1, T_2; \gamma = 4\pi\alpha)$, to generate different probability distribution functions of the fading amplitude [61], as shown in Fig. 5.1(a). In some special cases we are able to derive the analytical form of the distribution of the fading amplitude $P(|s_{rmt,21}|)$. For a lossless system ($\alpha = 0$), the absorption probabilities $T_1 = T_2 = 0$, and thus

$$|s_{rmt,21}| = \sqrt{2\xi(1-\xi)(1-\cos\phi)}. \tag{D.5}$$

By the known distributions of ξ and ϕ , we can compute the n^{th} moment $\langle |s_{rmt,21}|^n \rangle$ and the moment-generating function of $|s_{rmt,21}|$. We find that the moment-generating function [173, 174] of the fading amplitude is identical to the moment-generating

function of the uniform distribution $P(|s_{rmt,21}|) = 1$, for $0 \leq |s_{rmt,21}| \leq 1$. Therefore, we conclude that the distribution of $|s_{rmt,21}|$ is uniform in the zero-loss limit.

For high loss systems ($\gamma \gg 1$), the dominant term in Eq. (D.3) is $\gamma^3 e^\gamma$, so

$$\begin{aligned} P(T_1, T_2; \gamma \gg 1) &\simeq \frac{1}{8} \frac{|T_1 - T_2|}{T_1^4 T_2^4} \exp \left[-\frac{\gamma}{2} \left(\frac{1}{T_1} + \frac{1}{T_2} \right) \right] \gamma^3 e^\gamma \\ &= \frac{\gamma^3}{8} \frac{|T_1 - T_2|}{T_1^4 T_2^4} \exp \left[-\frac{\gamma}{2} \left(\frac{1}{T_1} + \frac{1}{T_2} - 2 \right) \right]. \end{aligned} \quad (\text{D.6})$$

Because of $0 \leq T_1 \leq 1$ and $0 \leq T_2 \leq 1$, the term $(\frac{1}{T_1} + \frac{1}{T_2} - 2) > 0$, and the distribution $P(T_1, T_2; \gamma \gg 1)$ is negligible except when $T_1 \rightarrow 1$ and $T_2 \rightarrow 1$. Therefore, we use the approximation $1/T_1 \simeq 2 - T_1$ and $1/T_2 \simeq 2 - T_2$ in the exponential function in Eq. (D.6), and we keep only the dominant term. The joint distribution function $P(T_1, T_2)$ becomes

$$P(T_1, T_2; \gamma \gg 1) \simeq \frac{\gamma^3}{8} |T_1 - T_2| \exp \left[-\frac{\gamma}{2} (2 - T_1 - T_2) \right]. \quad (\text{D.7})$$

With this joint distribution and the formula of $|s_{rmt,21}|$ [Eq. (D.4)], we derive the n^{th} moment of the high-loss-limit distribution of $|s_{rmt,21}|$,

$$\begin{aligned} \langle |s_{rmt,21}|^n \rangle &= \int_0^1 d\xi \int_0^{2\pi} \frac{d\theta}{2\pi} \int_0^1 dT_1 \int_0^1 dT_2 |s_{rmt,21}|^n P(T_1, T_2; \gamma \gg 1) \\ &= \gamma^{\frac{-n}{2}} \Gamma \left(\frac{n}{2} + 1 \right), \end{aligned} \quad (\text{D.8})$$

where $\Gamma(\cdot)$ is the Γ function. Then we can derive the moment-generating function, and it is identical to the moment-generating function of the Rayleigh distribution [173, 174]. Therefore, the distribution of $|s_{rmt,21}|$ is

$$P(x = |s_{rmt,21}|; \alpha \gg 1) = 8\pi\alpha x \exp(-4\pi\alpha x^2), \quad (\text{D.9})$$

which is a Rayleigh distribution $P(x; \sigma) = (x/\sigma^2) \exp[-x^2/(2\sigma^2)]$ with the relation

$$\alpha = \frac{1}{8\pi\sigma^2}. \quad (\text{D.10})$$

D.2 Time-Reversal-Invariance-Broken Case

For the time-reversal-invariance-broken (TRIB) case [21], we have a different joint distribution function $\tilde{P}(T_1, T_2)$, and U_1 and U_2 in Eq. (D.1) are now independent random unitary matrices with independent random variables $\psi_1, \varphi_1, \beta_1, \psi_2, \varphi_2$, and β_2 , which are all uniformly distributed from 0 to 2π . $\theta_1 = \arcsin(\sqrt{\xi_1})$ and $\theta_2 = \arcsin(\sqrt{\xi_2})$ with independent random variables ξ_1 and ξ_2 uniformly distributing from 0 to 1. The fluctuating fading amplitude for the TRIB case is

$$|\tilde{s}_{rmt,21}|^2 = \xi_1(1 - \xi_2)(1 - T_1) + \xi_2(1 - \xi_1)(1 - T_2) + 2 \cos \tilde{\phi} \sqrt{\xi_1 \xi_2 (1 - \xi_1)(1 - \xi_2)(1 - T_1)(1 - T_2)}, \quad (\text{D.11})$$

where $\tilde{\phi} = \psi_1 + \psi_2 + \varphi_1 - \varphi_2$ has a uniform distribution on $[0, 2\pi)$. We numerically generate $|\tilde{s}_{rmt,21}|$ from Eq. (D.11) and plot the probability distributions $P(|\tilde{s}_{rmt,21}|)$ with varying loss parameters in Fig. 5.1(b). The numerical results show that the distribution $P(|\tilde{s}_{rmt,21}|)$ is a triangular distribution $P(x) = 2x$ for $0 \leq x = |\tilde{s}_{rmt,21}| \leq 1$ in the lossless case, different from the TRI case. However, in the high loss limit the distribution $P(|\tilde{s}_{rmt,21}|)$ goes to a Rayleigh distribution with the relation $\alpha = 1/(8\pi\sigma^2)$, as with the time-reversal-invariant case.

Since the phases of $s_{rmt,21}$ and $\tilde{s}_{rmt,21}$ are uniformly distributed between 0 and 2π [57, 58], a Rayleigh-distributed magnitude means the real part and the imaginary part of $s_{rmt,21}$ and $\tilde{s}_{rmt,21}$ are independent and identically distributed (i.i.d.) Gaussian distributions with zero mean and the variance $\sigma^2 = (8\pi\alpha)^{-1}$. Therefore, in the high loss limit, the loss eliminates the correlations in the random matrix of the TRI case (GOE) [or the TRIB case (GUE)], and the real part and

the imaginary part of the random variable $s_{rmt,21}$ (or $\tilde{s}_{rmt,21}$) become i.i.d. normal distributions, and the variances only depend on the loss parameter α . In practice, note that time-reversal invariance for wave systems can be continuously broken [26, 49, 53, 113], so in the partially broken case the statistical properties would be in between the TRI case and the TRIB case.

D.3 Conclusion

We start from the RMT prediction of the universal scattering matrix and combine it with the random coupling model to derive a statistical model for the fading parameter. In this appendix I show the detailed derivations of the fading amplitudes $|s_{rmt,21}|$ for the time-reversal-invariant case and $|\tilde{s}_{rmt,21}|$ for the time-reversal-invariance-broken case. In Chapter 5 these results are further combined with the system-specific features in the wave scattering system by the extended random coupling model. This is a new application of wave chaos theory in the field of wireless communications, and this RMT fading model is more complete than traditional models.

Bibliography

- [1] M. L. Mehta, *Random Matrices*, Academic Press, Boston, 2 edition, 1991.
- [2] X. Zheng, *Statistics of impedance and scattering matrices in microwave chaotic cavities: the random coupling model*, Ph.D. thesis, University of Maryland, College Park, 2005, <http://hdl.handle.net/1903/2920>.
- [3] S. Hemmady, *A Wave-Chaotic Approach to Predicting and Measuring Electromagnetic Field Quantities in Complicated Enclosures*, Ph.D. thesis, University of Maryland, College Park, 2006, <http://hdl.handle.net/1903/3979>.
- [4] J. Hart, *Scattering from chaotic cavities: Exploring the random coupling model in the time and frequency domains*, Ph.D. thesis, University of Maryland, College Park, 2009, <http://hdl.handle.net/1903/9549>.
- [5] M. C. Gutzwiller, *Chaos in Classical and Quantum Mechanics*, Springer-Verlag, New York, 1990.
- [6] J. J. Leader, *Numerical Analysis and Scientific Computation*, Addison-Wesley, Boston, 2004.
- [7] R. Holland and R. St. John, *Statistical Electromagnetics*, Taylor and Francis, 1999.
- [8] M. Simon and M.-S. Alouini, *Digital Communication over Fading Channels*, Wiley-Interscience, Hoboken, NJ, 2 edition, 2005.
- [9] S. Hemmady, T. M. Antonsen, E. Ott, and S. M. Anlage, “Statistical prediction and measurement of induced voltages on components within complicated enclosures: A wave-chaotic approach,” *IEEE Trans. Electromag. Compat.*, vol. 54, pp. 758, 2012.
- [10] F. Haake, *Quantum Signatures of Chaos*, Springer, Berlin, 2 edition, 2000.
- [11] H. J. Stöckmann, *Quantum Chaos*, Cambridge University Press, Cambridge, England, 1999.
- [12] E. P. Wigner, “On a class of analytic functions from the quantum theory of collisions,” *Ann. Math.*, vol. 53, pp. 36, 1951.
- [13] E. P. Wigner, “Characteristic vectors of bordered matrices with infinite dimensions,” *Ann. Math.*, vol. 62, pp. 548, 1955.
- [14] E. P. Wigner, “Characteristic vectors of bordered matrices with infinite dimensions II,” *Ann. Math.*, vol. 65, pp. 203, 1957.

- [15] E. P. Wigner, “On the distribution of the roots of certain symmetric matrices,” *Ann. Math.*, vol. 67, pp. 325, 1958.
- [16] A. M. Lane and R. G. Thomas, “R-matrix theory of nuclear reactions,” *Rev. Mod. Phys.*, vol. 30, pp. 257, 1958.
- [17] F. J. Dyson, “Statistical theory of the energy levels of complex systems. I,” *J. Math. Phys.*, vol. 3, pp. 140, 1962.
- [18] R. G. Newton, *Scattering theory of waves and particles*, McGraw-Hill, New York, 1966.
- [19] V. Pagneux and A. Maurel, “Irregular scattering of acoustic rays by vortices,” *Phys. Rev. Lett.*, vol. 86, pp. 1199, 2001.
- [20] G. Tanner and N. Søndergaard, “Wave chaos in acoustics and elasticity,” *J. Phys. A: Math. Theor.*, vol. 40, pp. R443, 2007.
- [21] P. W. Brouwer and C. W. J. Beenakker, “Voltage-probe and imaginary-potential models for dephasing in a chaotic quantum dot,” *Phys. Rev. B*, vol. 55, pp. 4695, 1997.
- [22] Y. Alhassid, “The statistical theory of quantum dots,” *Rev. Mod. Phys.*, vol. 75, pp. 895, 2000.
- [23] P. A. Mello and N. Kumar, *Quantum Transport in Mesoscopic Systems*, Oxford University Press, New York, 2004.
- [24] U. Kuhl, M. Martínez-Mares, R. A. Méndez-Sánchez, and H. J. Stöckmann, “Direct processes in chaotic microwave cavities in the presence of absorption,” *Phys. Rev. Lett.*, vol. 94, pp. 144101, 2005.
- [25] O. Bohigas, M. J. Giannoni, and C. Schmidt, “Characterization of chaotic quantum spectra and universality of level fluctuation laws,” *Phys. Rev. Lett.*, vol. 51, pp. 1, 1984.
- [26] P. So, S. M. Anlage, E. Ott, and R. N. Oerter, “Wave chaos experiments with and without time reversal symmetry: GUE and GOE statistics,” *Phys. Rev. Lett.*, vol. 74, pp. 2662, 1995.
- [27] E. Ott, *Chaos in Dynamical Systems*, Cambridge University Press, New York, 2 edition, 2002.
- [28] S. W. McDonald and A. N. Kaufman, “Wave chaos in the stadium: Statistical properties of short-wave solutions of the Helmholtz equation,” *Phys. Rev. Lett.*, vol. 37, pp. 3067, 1988.
- [29] G. D. Birkhoff, “On the periodic motions of dynamical systems,” *Acta Math.*, vol. 50, pp. 359, 1927.

- [30] K. Richter and M. Sieber, “Semiclassical theory of chaotic quantum transport,” *Phys. Rev. Lett.*, vol. 89, pp. 206801, 2002.
- [31] H.-J. Stöckmann and J. Stein, “‘Quantum’ chaos in billiards studied by microwave absorption,” *Phys. Rev. Lett.*, vol. 64, pp. 2215, 1990.
- [32] S. W. McDonald and A. N. Kaufman, “Spectrum and eigenfunctions for a Hamiltonian with stochastic trajectories,” *Phys. Rev. Lett.*, vol. 42, pp. 1189, 1979.
- [33] G. Casati and T. Prosen, “Triangle map: A model of quantum chaos,” *Phys. Rev. Lett.*, vol. 85, pp. 4261, 2000.
- [34] S. Sridar, “Experimental observation of scarred eigenfunctions of chaotic microwave cavities,” *Phys. Rev. Lett.*, vol. 67, pp. 785, 1991.
- [35] E. Doron, U. Smilansky, and A. Frenkel, “Experimental demonstration of chaotic scattering of microwaves,” *Phys. Rev. Lett.*, vol. 65, pp. 3072, 1990.
- [36] S. Hemmady, X. Zheng, E. Ott, T. M. Antonsen, and S. M. Anlage, “Universal impedance fluctuations in wave chaotic systems,” *Phys. Rev. Lett.*, vol. 94, pp. 014102, 2005.
- [37] Y.-H. Kim, U. Kuhl, H.-J. Stöckmann, and J. P. Bird, “Investigating dynamical tunnelling in open quantum dots by means of a soft-walled microwave-cavity analogue,” *J. Phys.: Condens. Matter*, vol. 17, pp. L191, 2005.
- [38] G. Akemann, J. Baik, and P. Di Francesco, Eds., *The Oxford Handbook of Random Matrix Theory*, Oxford, 2011. Oxford University Press.
- [39] J. A. Hart, T. M. Antonsen, and E. Ott, “Effect of short ray trajectories on the scattering statistics of wave chaotic systems,” *Phys. Rev. E*, vol. 80, pp. 041109, 2009.
- [40] J.-H. Yeh, J. A. Hart, E. Bradshaw, T. M. Antonsen, E. Ott, and S. M. Anlage, “Universal and nonuniversal properties of wave-chaotic scattering systems,” *Phys. Rev. E*, vol. 81, pp. 025201(R), 2010.
- [41] J.-H. Yeh, J. A. Hart, E. Bradshaw, T. M. Antonsen, E. Ott, and S. M. Anlage, “Experimental examination of the effect of short ray trajectories in two-port wave-chaotic scattering systems,” *Phys. Rev. E*, vol. 82, pp. 041114, 2010.
- [42] E. B. Bogomolny, “Semiclassical quantization of multidimensional systems,” *Nonlinearity*, vol. 5, pp. 805, 1992.
- [43] T. Kottos and U. Smilansky, “Quantum graphs: a simple model for chaotic scattering,” *J. Phys. A: Math. Gen.*, vol. 36, pp. 3501, 2003.
- [44] T. Kottos and U. Smilansky, “Chaotic scattering on graphs,” *Phys. Rev. Lett.*, vol. 85, pp. 968, 2000.

- [45] S. Gnutzmann and U. Smilansky, “Quantum graphs: Applications to quantum chaos and universal spectral statistics,” *Adv. in Phys.*, vol. 55, pp. 527, 2006.
- [46] A. M. Tulino and S. Verdú, “Random matrix theory and wireless communications,” *Foundations and Trends in Commun. and Inf. Theory*, vol. 1, pp. 1, 2004.
- [47] T. Guhr, A. Müller-Groeling, and H. A. Weidenmüller, “Random-matrix theories in quantum physics: common concepts,” *Phys. Rep.*, vol. 299, pp. 189, 1998.
- [48] A. Pandey and M. L. Mehta, “Gaussian ensembles of random Hermitian matrices intermediate between orthogonal and unitary ones,” *Comm. Math. Phys.*, vol. 87, pp. 449, 1993.
- [49] S.-H. Chung, A. Gokirmak, D.-H. Wu, J. S. A. Bridgewater, E. Ott, T. M. Antonsen, and S. M. Anlage, “Measurement of wave chaotic eigenfunctions in the time-reversal symmetry-breaking crossover regime,” *Phys. Rev. Lett.*, vol. 85, pp. 2482, 2000.
- [50] J. M. Nieminen, “Eigenvalue spacing statistics of a four-matrix model of some four-by-four random matrices,” *J. Phys. A: Math. Theor.*, vol. 42, pp. 035001, 2009.
- [51] H. Schanze, H.-J. Stöckmann, M. Martínez-Mares, and C. H. Lewenkopf, “Universal transport properties of open microwave cavities with and without time-reversal symmetry,” *Phys. Rev. E*, vol. 71, pp. 016223, 2005.
- [52] F. Schäfer, *Time-Reversal Symmetry Breaking in Quantum Billiards*, Ph.D. thesis, der Technischen Universität Darmstadt, Darmstadt, 2009, http://www.ikp.tu-darmstadt.de/media/ikp/achimrichter/quantumchaos/theses/schaefer_diss.pdf.
- [53] B. Dietz, T. Friedrich, H. L. Harney, M. Miski-Oglu, A. Richter, F. Schäfer, J. Verbaarschot, and H. A. Weidenmüller, “Induced violation of time-reversal invariance in the regime of weakly overlapping resonances,” *Phys. Rev. Lett.*, vol. 103, pp. 064101, 2009.
- [54] J. J. M. Verbaarschot, H. A. Weidenmüller, and M. R. Zirnbauer, “Grassmann integration in stochastic quantum physics: The case of compound-nucleus scattering,” *Phys. Rep.*, vol. 129, pp. 367, 1985.
- [55] C. W. J. Beenakker, “Random-matrix theory of quantum transport,” *Rev. Mod. Phys.*, vol. 69, pp. 731, 1997.
- [56] Y. V. Fyodorov, D. V. Savin, and H.-J. Sommers, “Scattering, reflection and impedance of waves in chaotic and disordered systems with absorption,” *J. Phys. A: Math. Gen.*, vol. 38, pp. 10731, 2005.

- [57] X. Zheng, T. M. Antonsen, and E. Ott, “Statistics of impedance and scattering matrices in chaotic microwave cavities: Single channel case,” *Electromagnetics*, vol. 26, pp. 3, 2006.
- [58] X. Zheng, T. M. Antonsen, and E. Ott, “Statistics of impedance and scattering matrices of chaotic microwave cavities with multiple ports,” *Electromagnetics*, vol. 26, pp. 37, 2006.
- [59] X. Zheng, S. Hemmady, T. M. Antonsen, S. M. Anlage, and E. Ott, “Characterization of fluctuations of impedance and scattering matrices in wave chaotic scattering,” *Phys. Rev. E*, vol. 73, pp. 046208, 2006.
- [60] S. Hemmady, X. Zheng, T. M. Antonsen, E. Ott, and S. M. Anlage, “Universal statistics of the scattering coefficient of chaotic microwave cavities,” *Phys. Rev. E*, vol. 71, pp. 056215, 2005.
- [61] J.-H. Yeh, T. M. Antonsen, E. Ott, and S. M. Anlage, “First-principles model of time-dependent variations in transmission through a fluctuating scattering environment,” *Phys. Rev. E*, vol. 85, pp. 015202(R), 2012.
- [62] J.-H. Yeh, T. M. Antonsen, E. Ott, and S. M. Anlage, “Fading statistics in communications - a random matrix approach,” *Acta Physica Polonica A*, vol. 120, pp. A-85, 2012.
- [63] P. A. Mello, P. Peveyra, and T. H. Seligman, “Information theory and statistical nuclear reactions. I. general theory and applications to few-channel problems,” *Ann. of Phys.*, vol. 161, pp. 254, 1985.
- [64] D. M. Pozar, *Microwave Engineering*, Addison-Wesley Longman, Boston, 1990.
- [65] Y. V. Fyodorov and D. V. Savin, “Statistics of impedance, local density of states, and reflection in quantum chaotic systems with absorption,” *JETP Lett.*, vol. 80, pp. 725, 2004.
- [66] D. V. Savin, H.-J. Sommers, and Y. V. Fyodorov, “Universal statistics of the local Green’s function in wave chaotic systems with absorption,” *JETP Lett.*, vol. 82, pp. 544, 2005.
- [67] C. H. Lewenkopf and H. A. Weidemüller, “Stochastic versus semiclassical approach to quantum chaotic scattering,” *Ann. of Phys.*, vol. 212, pp. 53, 1991.
- [68] J. Stein and H.-J. Stöckmann, “Experimental determination of billiard wave functions,” *Phys. Rev. Lett.*, vol. 68, pp. 2867, 1992.
- [69] J. P. Bird, D. M. Olatona, R. Newbury, R. P. Taylor, K. Ishibashi, M. Stopa, Y. Aoyagi, , T. Sugano, and Y. Ochiai, “Lead-induced transition to chaos in ballistic mesoscopic billiards,” *Phys. Rev. B*, vol. 52, pp. R14336, 1995.

- [70] H. Ishio and J. Burgdörfer, “Quantum conductance fluctuations and classical short-path dynamics,” *Phys. Rev. B*, vol. 51, pp. 2013, 1995.
- [71] H. U. Baranger and P. A. Mello, “Short paths and information theory in quantum chaotic scattering: transport through quantum dots,” *Europhys. Lett.*, vol. 33, pp. 465, 1996.
- [72] Y.-H. Kim, M. Barth, U. Kuhl, H.-J. Stöckmann, and J. P. Bird, “Scanning Fourier spectroscopy: A microwave analog study to image transmission paths in quantum dots,” *Phys. Rev. B*, vol. 68, pp. 045315, 2003.
- [73] J. D. Urbina and K. Richter, “Semiclassical construction of random wave functions for confined systems,” *Phys. Rev. E*, vol. 70, pp. 015201(R), 2004.
- [74] R. E. Prange, “Resurgence in quasi-classical scattering,” *J. Phys. A: Math. Gen.*, vol. 38, pp. 10703, 2005.
- [75] E. N. Bulgakov, V. A. Gopar, P. A. Mello, and I. Rotter, “Statistical study of the conductance and shot noise in open quantum-chaotic cavities: Contribution from whispering gallery modes,” *Phys. Rev. B*, vol. 73, pp. 155302, 2006.
- [76] G. L. Stüber, *Principles of Mobile Communications*, Kluwer Academic Publishers, Norwell, MA, 1996.
- [77] G. J. Foschini, “Layered space-time architecture for wireless communication in a fading environment when using multi-element antennas,” *Bell Labs Technical J.*, vol. 1, pp. 41, 1996.
- [78] O. Delangre, P. Doncker, M. Lienard, and P. Degauque, “Coupled reverberation chambers for emulating MIMO channels,” *C. R. Physique*, vol. 11, pp. 30, 2010.
- [79] M. Nakagami, “The m-distribution, a general formula of intensity of rapid fading,” in *Statistical Methods in Radio Wave Propagation*, W. C. Hoffman, Ed., New York, 1960, p. 3, Pergamon Press.
- [80] C. Lemoine, E. Amador, and P. Besnier, “Mode-stirring efficiency of reverberation chambers based on Rician K-factor,” *Electron. Lett.*, vol. 47, pp. 20, 2011.
- [81] A. L. Moustakas, H. U. Baranger, L. Balents, A. M. Sengupta, and S. H. Simon, “Communication through a diffusive medium: Coherence and capacity,” *Science*, vol. 287, pp. 287, 2000.
- [82] S. H. Simon, A. L. Moustakas, M. Stoytchev, and H. Safar, “Communication in a disordered world,” *Physics Today*, vol. 54, pp. 38, 2001.

- [83] A. L. Moustakas and S. H. Simon, “Random matrix theory of multi-antenna communications: the Ricean channel,” *J. Phys. A: Math. Gen.*, vol. 38, pp. 10859, 2005.
- [84] V. I. Morgenshtern and H. Bölcskei, “Crystallization in large wireless networks,” *IEEE Trans. on Information Theory*, vol. 53, pp. 10, 2007.
- [85] V. A. Gopar, M. Martínez-Mares, and R. A. Méndez-Sánchez, “Chaotic scattering with direct processes: a generalization of Poisson’s kernel for non-unitary scattering matrices,” *J. Phys. A: Math. Theor.*, vol. 41, pp. 015103, 2008.
- [86] E. Ott, “Instability condition for confined waves with ergodic ray trajectories,” *Phys. Fluids*, vol. 22, pp. 2246, 1979.
- [87] M. V. Berry, “Semiclassical mechanics of regular and irregular motion,” in *Chaotic Behavior of Deterministic Systems*. 1983, p. 171, North-Holland.
- [88] S. Hemmady, X. Zheng, T. M. Antonsen, E. Ott, and S. M. Anlage, “Universal properties of two-port scattering, impedance, and admittance matrices of wave-chaotic systems,” *Phys. Rev. E*, vol. 74, pp. 036213, 2006.
- [89] S. Hemmady, X. Zheng, T. M. Antonsen, E. Ott, and S. M. Anlage, “Aspects of the scattering and impedance properties of chaotic microwave cavities,” *Acta Physica Polonica A*, vol. 109, pp. 65, 2006.
- [90] S. Hemmady, J. Hart, X. Zheng, T. M. Antonsen, E. Ott, and S. M. Anlage, “Experimental test of universal conductance fluctuations by means of wave-chaotic microwave cavities,” *Phys. Rev. B*, vol. 74, pp. 195326, 2006.
- [91] H. Weyl, “Über die gleichverteilung von zahlen mod. eins.,” *Math. Ann.*, vol. 77, pp. 313, 1916.
- [92] M. Sieber and K. Richter, “Correlations between periodic orbits and their rôle in spectral statistics,” *Phys. Scr.*, vol. 90, pp. 128, 2001.
- [93] D. Wintgen and H. Friedrich, “Correspondence of unstable periodic orbits and quasi-Landau modulations,” *Phys. Rev. A*, vol. 36, pp. 131, 1987.
- [94] R. Schäfer, T. Gorin, T. H. Seligman, and H.-J. Stöckmann, “Fidelity amplitude of the scattering matrix in microwave cavities,” *New J. Phys.*, vol. 7, pp. 152, 2005.
- [95] L. Wirtz, J.-Z. Tang, and J. Burgdörfer, “Geometry-dependent scattering through ballistic microstructures: Semiclassical theory beyond the stationary-phase approximation,” *Phys. Rev. B*, vol. 56, pp. 7589, 1997.
- [96] R. G. Nazmitdinov, K. N. Pichugin, I. Rotter, and P. Šeba, “Conductance of open quantum billiards and classical trajectories,” *Phys. Rev. B*, vol. 66, pp. 085322, 2002.

- [97] C. Stampfer, S. Rotter, and J. Burgdörfer, “Pseudopath semiclassical approximation to transport through open quantum billiards: Dyson equation for diffractive scattering,” *Phys. Rev. E*, vol. 72, pp. 036223, 2005.
- [98] H. Ishio and J. P. Keating, “Semiclassical wavefunctions in chaotic scattering systems,” *J. Phys. A: Math. Gen.*, vol. 37, pp. L217, 2004.
- [99] J. D. Urbina and K. Richter, “Statistical description of eigenfunctions in chaotic and weakly disordered systems beyond universality,” *Phys. Rev. Lett.*, vol. 97, pp. 214101, 2006.
- [100] S. Müller, S. Heusler, P. Braun, and F. Haake, “Semiclassical approach to chaotic quantum transport,” *New J. Phys.*, vol. 9, pp. 12, 2007.
- [101] B. Dietz, A. Heine, A. Richter, O. Bohigas, and P. Leboeuf, “Spectral statistics in an open parametric billiard system,” *Phys. Rev. E*, vol. 73, pp. 035201(R), 2006.
- [102] B. Dietz, T. Friedrich, H. L. Harney, M. Miski-Oglu, A. Richter, F. Schäfer, and H. A. Weidenmüller, “Chaotic scattering in the regime of weakly overlapping resonances,” *Phys. Rev. E*, vol. 78, pp. 055204, 2008.
- [103] A. Gokirmak, D.-H. Wu, J. Bridgewater, and S. M. Anlage, “Scanned perturbation technique for imaging electromagnetic standing wave patterns of microwave cavities,” *Rev. Sci. Instrum.*, vol. 69, pp. 3410, 1998.
- [104] S. Ree and L. E. Reichl, “Classical and quantum chaos in a circular billiard with a straight cut,” *Phys. Rev. E*, vol. 60, pp. 1607, 1999.
- [105] A. Richter, “Wave dynamical chaos: an experimental approach in billiards,” *Phys. Scr.*, vol. T90, pp. 212, 2001.
- [106] G. F. Engen and C. A. Hoer, “Thru-reflect-line: An improved technique for calibrating the dual six-port automatic network analyzer,” *IEEE Trans. Microwave Theory Tech.*, vol. 27, pp. 987, 1979.
- [107] R. B. Marks, “A multiline method of network analyzer calibration,” *IEEE Trans. Microwave Theory Tech.*, vol. 39, pp. 1205, 1991.
- [108] J.-H. Yeh and S. Anlage, “*In situ* broadband cryogenic calibration for two-port superconducting microwave resonators,” *Rev. Sci. Instrum.*, vol. 84, pp. 034706, 2013.
- [109] B. T. Taddese, T. M. Antonsen, E. Ott, and S. M. Anlage, “Iterative time reversal with tunable convergence,” *Electronics Lett.*, vol. 47, pp. 1165, 2011.
- [110] M. Frazier, B. Taddese, T. Antonsen, and S. M. Anlage, “Nonlinear time-reversal in a wave chaotic system,” *Phys. Rev. Lett.*, vol. 110, pp. 063902, 2013.

- [111] P. W. Brouwer, “Generalized circular ensemble of scattering matrices for a chaotic cavity with nonideal leads,” *Phys. Rev. B*, vol. 51, pp. 16878, 1995.
- [112] M. Büttiker, “Time-dependent transport in mesoscopic structures,” *J. Low Temp. Phys.*, vol. 118, pp. 519, 2000.
- [113] U. Stoffregen, J. Stein, H.-J. Stöckmann, M. Kuś, and F. Haake, “Microwave billiards with broken time reversal symmetry,” *Phys. Rev. Lett.*, vol. 74, pp. 2666, 1995.
- [114] G. Gradoni, J.-H. Yeh, T. M. Antonsen, S. M. Anlage, and E. Ott, “Wave chaotic analysis of weakly coupled reverberation chambers,” in *Electromagnetic Compatibility (EMC), 2011 IEEE International Symposium on*, 2011, pp. 202–207.
- [115] C. W. J. Beenakker, “Applications of random matrix theory to condensed matter and optical physics,” in *The Oxford Handbook of Random Matrix Theory*, G. Akemann, J. Baik, and P. Di Francesco, Eds., p. 723. Oxford University Press, Oxford, 2011.
- [116] Y.-H. Kim, M. Barth, H.-J. Stöckmann, and J. P. Bird, “Wave function scarring in open quantum dots: A microwave-billiard analog study,” *Phys. Rev. B*, vol. 65, pp. 165317, 2002.
- [117] H. U. Baranger and P. A. Mello, “Mesoscopic transport through chaotic cavities: A random S-matrix theory approach,” *Phys. Rev. Lett.*, vol. 73, pp. 142, 1994.
- [118] R. A. Jalabert, J.-L. Pichard, and C. W. J. Beenakker, “Universal quantum signatures of chaos in ballistic transport,” *Europhys. Lett.*, vol. 27, pp. 255, 1994.
- [119] D. V. Savin and H.-J. Sommers, “Shot noise in chaotic cavities with an arbitrary number of open channels,” *Phys. Rev. B*, vol. 73, pp. 081307(R), 2006.
- [120] S. F. Godijn, S. Möller, H. Buhmann, L. W. Molenkamp, and S. A. van Langen, “Thermopower of a chaotic quantum dot,” *Phys. Rev. Lett.*, vol. 82, pp. 2927, 1999.
- [121] P. W. Brouwer, K. M. Frahm, and C. W. J. Beenakker, “Quantum mechanical time-delay matrix in chaotic scattering,” *Phys. Rev. Lett.*, vol. 78, pp. 4737, 1997.
- [122] M.-J. Lee, T. M. Antonsen, and E. Ott, “Statistical model of short wavelength transport through cavities with coexisting chaotic and regular ray trajectories,” *Phys. Rev. E*, vol. 87, pp. 062906, 2013.

- [123] P. S. Cannon, K. Groves, D. J. Fraser, W. J. Donnelly, and K. Perrier, “Signal distortion on VHF/UHF transionospheric paths: First results from the wideband ionospheric distortion experiment,” *Radio Sci.*, vol. 41, pp. RS5S40, 2006.
- [124] P. M. Kintner, B. M. Ledvina, and E. R. de Paula, “GPS and ionospheric scintillations,” *J. Geophys. Res. Space Weather*, vol. 5, pp. S09003, 2007.
- [125] E. J. Heller, L. Kaplan, and A. Dahlen, “Refraction of a Gaussian seaway,” *J. Geophys. Res.*, vol. 113, pp. C09023, 2008.
- [126] M. S. Longuet-Higgins, “Statistical properties of an isotropic random surface,” *Phil. Trans. R. Soc. Lond. A*, vol. 250, no. 975, pp. 157, 1957.
- [127] H. Dankert, J. Horstmann, S. Lehner, and W. Rosenthal, “Detection of wave groups in SAR images and radar image sequences,” *IEEE Trans. Geosci. Remote Sens.*, vol. 41, pp. 1437, 2003.
- [128] C. Kharif and E. Pelinovsky, “Physical mechanisms of the rogue wave phenomenon,” *Eur. J. Mech. B*, vol. 22, pp. 603, 2003.
- [129] M. Onorato, A. R. Osborne, M. Serio, and S. Bertone, “Freak waves in random oceanic sea states,” *Phys. Rev. Lett.*, vol. 86, pp. 5831, 2001.
- [130] V. E. Zakharov, “Stability of periodic waves of finite amplitude on the surface of a deep fluid,” *J. Appl. Mech. Tech. Phys.*, vol. 9, pp. 190, 1968.
- [131] K. B. Dysthe, “Note on a modification to the nonlinear Schrödinger equation for application to deep water waves,” *Proc. R. Soc. Lond. A*, vol. 369, pp. 105, 1979.
- [132] K. Trulsen and K. B. Dysthe, “A modified nonlinear Schrödinger equation for broader bandwidth gravity waves on deep water,” *Wave Motion*, vol. 24, pp. 281, 1996.
- [133] D. H. Peregrine, “Interaction of water waves and currents,” *Adv. appl. Mech.*, vol. 16, pp. 9, 1976.
- [134] B. S. White and B. Fornberg, “On the chance of freak waves at sea,” *J. Fluid. Mech.*, vol. 355, pp. 113, 1998.
- [135] D. H. Peregrine, “Water waves, nonlinear Schrödinger equations and their solutions,” *J. Austral. Math. Soc. Ser. B*, vol. 25, pp. 16, 1983.
- [136] F. Baronio, A. Degasperis, M. Conforti, and S. Wabnitz, “Solutions of the vector nonlinear Schrödinger equations: Evidence for deterministic rogue waves,” *Phys. Rev. Lett.*, vol. 109, pp. 044102, 2012.
- [137] M. Onorato, D. Proment, and A. Toffoli, “Triggering rogue waves in opposing currents,” *Phys. Rev. Lett.*, vol. 107, pp. 184502, 2011.

- [138] L. Stenflo and P. K. Shukla, “Nonlinear acoustic gravity waves,” *J. Plasma Phys.*, vol. 75, pp. 841, 2009.
- [139] D. R. Solli, C. Ropers, P. Koonath, and B. Jalali, “Optical rogue waves,” *Nature*, vol. 450, pp. 1054, 2007.
- [140] M. Erkintalo, G. Genty, and J. M. Dudley, “Rogue-wave-like characteristics in femtosecond supercontinuum generation,” *Opt. Lett.*, vol. 34, pp. 2468, 2009.
- [141] B. Kibler, J. Fatome, C. Finot, G. Millot, F. Dias, G. Genty, N. Akhmediev, and J. M. Dudley, “The Peregrine soliton in nonlinear fibre optics,” *Nature Phys.*, vol. 6, pp. 790, 2010.
- [142] W. M. Moslem, P. K. Shukla, and B. Eliasson, “Surface plasma rogue waves,” *Europhys. Lett.*, vol. 96, pp. 25002, 2011.
- [143] Y. V. Bludov, V. V. Konotop, and N. Akhmediev, “Matter rogue waves,” *Phys. Rev. A*, vol. 80, pp. 033610, 2009.
- [144] R. Höhmann, U. Kuhl, H.-J. Stöckmann, L. Kaplan, and E. J. Heller, “Freak waves in the linear regime: A microwave study,” *Phys. Rev. Lett.*, vol. 104, pp. 093901, 2010.
- [145] A. Chabchoub, N. P. Hoffmann, and N. Akhmediev, “Rogue wave observation in a water wave tank,” *Phys. Rev. Lett.*, vol. 106, pp. 204502, 2011.
- [146] F. M. de Aguiar, “Resonant freak microwaves,” *Phys. Lett. A*, vol. 375, pp. 265, 2011.
- [147] M. Bartuccelli, P. Constantin, C. R. Doering, J. D. Gibbon, and M. Gisselält, “On the possibility of soft and hard turbulence in the complex Ginzburg-Landau equation,” *Physica D*, vol. 44, pp. 421, 1990.
- [148] V. Nagy and E. Ott, “Control of rare intense events in spatiotemporally chaotic systems,” *Phys. Rev. E*, vol. 76, pp. 066206, 2007.
- [149] M.-J. Lee, *Statistical modeling of wave chaotic transport and tunneling*, Ph.D. thesis, University of Maryland, College Park, 2013, see <http://drum.lib.umd.edu/>.
- [150] J. A. Hart, “Effects of short orbits on the radiation impedance of chaotic cavities,” unpublished, 2007.
- [151] *TRL Calibration*, see http://na.tm.agilent.com/pna/help/latest/S3_Cals/TRL_Calibration.htm for a discussion of the TRL calibration.
- [152] J. L. Cano and E. Artal, “Cryogenic technology applied to microwave engineering,” *Microwave J.*, vol. 52, pp. 70, 2009.

- [153] J. L. Cano de Diego, *Cryogenic Technology in the Microwave Engineering: Application to MIC and MMIC Very Low Noise Amplifier Design*, Ph.D. thesis, University of Cantabria, 2010, <http://hdl.handle.net/10803/10674>.
- [154] A. Lewandowski and W. Wiatr, “Correction for line length errors and center-conductor-gap variation in the coaxial multilayer through-reflect-line calibration,” in *Microwave Measurement Symposium, 2009 74th ARFTG*, 2009, pp. 1–7.
- [155] J. Laskar, J. J. Bautista, M. Nishimoto, M. Hamai, and R. Lai, “Development of accurate on-wafer, cryogenic characterization techniques,” *IEEE Trans. Microw. Theory Tech.*, vol. 44, pp. 1178, 1996.
- [156] L. Ranzani, L. Spietz, Z. Popovic, and J. Aumentado, “Two-port microwave calibration at millikelvin temperatures,” *Rev. Sci. Instrum.*, vol. 84, pp. 034704, 2013.
- [157] J. C. Booth, J. A. Beall, D. C. DeGroot, D. A. Rudman, R. H. Ono, J. R. Miller, M. L. Chen, S. H. Hong, and Q. Y. Ma, “Microwave characterization of coplanar waveguide transmission lines fabricated by ion implantation patterning of $\text{YBa}_2\text{Cu}_3\text{O}_{7-\delta}$,” *IEEE Trans. Appl. Supercond.*, vol. 7, pp. 2780, 1997.
- [158] K. T. Leong, J. C. Booth, and J. H. Claassen, “Determination of the superconducting penetration depth from coplanar-waveguide measurements,” *J. Supercond. Novel Magn.*, vol. 19, pp. 637, 2006.
- [159] N. D. Orloff, A. Lewandowski, J. Mateu, E. Rocas, J. King, D. Gu, X. Lu, C. Collado, I. Takeuchi, and J. C. Booth, “A compact variable-temperature broadband series-resistor calibration,” *IEEE Trans. Microwave Theory Tech.*, vol. 59, pp. 188, 2011.
- [160] V. Shemelin, M. Liepe, and H. Padamsee, “Characterization of ferrites at low temperature and high frequency,” *Nucl. Instrum. Methods Phys. Res. A*, vol. 557, pp. 268, 2006.
- [161] M. S. Jun, S. W. Hwang, D. Y. Jeong, and D. Ahn, “Microwave design and characterization of a cryogenic dip probe for time-domain measurements of nanodevices,” *Rev. Sci. Instrum.*, vol. 75, pp. 2455, 2004.
- [162] D. L. Birx and D. J. Scalapino, “A cryogenic microwave switch,” *IEEE Trans. Magn.*, vol. 15, pp. 33, 1979.
- [163] L. Spietz, K. Irwin, M. Lee, and J. Aumentado, “Noise performance of lumped element direct current superconducting quantum interference device amplifiers in the 4 – 8 GHz range,” *Appl. Phys. Lett.*, vol. 97, pp. 142502, 2010.

- [164] D. H. Slichter, *Quantum Jumps and Measurement Backaction in a Superconducting Qubit*, Ph.D. thesis, University of California, Berkeley, 2011, http://physics.berkeley.edu/research/siddiqi/docs/Slichter_thesis_lo_res.pdf.
- [165] *Martinis Group*,
see <http://web.physics.ucsb.edu/~martinisgroup/electronics.shtml>
for applications of the cryogenic switches in superconducting quantum computing.
- [166] J. Juroshek, “A study of measurements of connector repeatability using highly reflecting loads,” *IEEE Trans. Microwave Theory Tech.*, vol. 35, pp. 457, 1987.
- [167] T. E. MacKenzie and A. E. Sanderson, “Some fundamental design principles for the development of precision coaxial standards and components,” *IEEE Trans. Microwave Theory Tech.*, vol. 14, pp. 29, 1966.
- [168] J. P. Hoffmann, P. Leuchtman, and R. Vahldieck, “Pin gap investigations for the 1.85mm coaxial connector,” *Proc. Eur. Microwave Conf.*, p. 388, 2007.
- [169] G. Vandersteen, Y. Rolain, J. Schoukens, and A. Verschuere, “An improved sliding-load calibration procedure using a semiparametric circle-fitting procedure,” *IEEE Trans. Microwave Theory Tech.*, vol. 45, pp. 1027, 1997.
- [170] *Radiall coaxial subminiature latching switches R591722605*,
the photograph is from the data sheet of the cryogenic switch
https://radiall-files.s3.amazonaws.com/tds/ramses/R591_GENERIC%20TDS.pdf.
- [171] D. Rytting, “Network analyzer error models and calibration methods,” in *Proc. ARFTG/NIST Short Course RF Measurements Wireless World*, 2001.
- [172] K. Życzkowski and M. Kuś, “Random unitary matrices,” *J. Phys. A: Math. Gen.*, vol. 27, pp. 4235, 1994.
- [173] M. G. Bulmer, *Principles of Statistics*, Courier Dover Publications, Mineola, New York, 1979.
- [174] A. Papoulis and S. Pillai, *Probability, Random Variables and Stochastic Processes*, McGraw-Hill Europe, Berkshire, 4 edition, 2002.